

# **Effects of Laser Welding on Formability Aspects of Advanced High Strength Steel**

by

Narasimhan Sreenivasan

A thesis  
presented to the University of Waterloo  
in fulfillment of the  
thesis requirement for the degree of  
Master of Applied Science  
in  
Mechanical Engineering

Waterloo, Ontario, Canada, 2007

© Narasimhan Sreenivasan 2007

I hereby declare that I am the sole author of this thesis. This is a true copy of the thesis, including any required final revisions, as accepted by my examiners.

I understand that my thesis may be made electronically available to the public.

## **Abstract**

Limiting dome height (LDH) tests were used to evaluate the formability of both base metal and laser butt welded blanks of AHSS (including High strength low alloy (HSLA), Dual phase (DP) steels of different grades). Mechanical properties of the base metal and welded blanks were assessed by uniaxial tensile and biaxial LDH tests, and related to measured microhardness distributions across the welds. The formability ratio of laser welded dual phase sheet steels generally decreases with increased base metal strength. A significant decrease of LDH was observed in the higher strength DP steel welded specimens due to the formation of a softened zone in the Heat Affected Zone (HAZ). Softened zone characteristics were correlated to the LDH. Larger softened zones led to a larger reduction in the LDH. HAZ softening has been shown to be a function of the base metal martensite content and the weld heat input. Formability also decreased with increased weld heat input. Both in experiment and numerical simulations strain is localized in the softened HAZ in the uniaxial tensile testing, indicating that strain localization decreases tensile strength and elongation of laser welds in DP980.

## **Acknowledgements**

I would like to thank my supervisors Dr. M. Kuntz and Dr. Y. Zhou for their guidance and great wisdom which have made this work possible. The interest and ideas of my friends and fellow researchers at the University of Waterloo have also been of great value. I would especially like to thank my wife and my parent for their unconditional support, encouragement, patience and understanding throughout the completion of this degree.

This work was funded by Auto21, one of the Networks of Centres of Excellence supported by the Canadian Government and International lead zinc research organization (ILZRO)

## Table of Contents

<b>1 Introduction.....</b>	<b>1</b>
1.1 Advanced high strength steel .....	1
1.2 Laser Welding.....	2
1.2.1 Definition of Laser .....	2
1.2.2 Laser Welding Applications .....	3
1.3 Tailor Welded Blanks .....	3
1.4 Problem and Justification.....	5
1.5 Objective .....	5
1.6 Criteria and Constraints .....	6
<b>2 Literature Review .....</b>	<b>7</b>
2.1 Formability of Sheet Metals.....	7
2.2 Advanced High Strength Steel.....	9
2.2.1 Metallurgy of AHSS .....	9
2.2.2 Dual Phase (DP) Steel.....	9
2.2.3 High Strength Low Alloy.....	11
2.3 Formability of AHSS .....	12
2.4 Progress in Tailor Welded Blank Applications .....	13
2.5 Laser Welding Technology.....	16
2.5.1 Laser Principle .....	16
2.5.2 Conduction Mode Welding.....	17
2.5.3 Keyhole Mode Welding.....	18
2.6 Advantages of Laser Welding.....	19
2.7 Limitations of Laser Welding Technology.....	20
2.8 Laser Welding of Advanced High Strength Steel.....	20
2.9 Factors Influencing Formability of Tailor Welded Blanks.....	21
2.9.1 Methods.....	22
2.9.2 Process .....	25
2.9.3 Machine.....	28
2.9.4 Material .....	28
2.10 Application of Numerical Methods for TWBs .....	29
2.11 Summary .....	30
<b>3 Equipment, Materials and Procedures .....</b>	<b>33</b>
3.1 Laser Equipment .....	33
3.1.1 The Diode Laser.....	33
3.1.2 Fixtures and Shielding Gas for Diode Laser.....	35
3.1.3 The Nd:YAG Laser.....	36
3.2 Selection of Materials .....	36
3.3 Metallurgical Examination.....	38
3.3.1 Sample Preparation .....	38
3.3.2 Optical Microscopy and SEM Analysis.....	38
3.4 Hardness Examination .....	39
3.5 Tensile Testing.....	39
3.6 Formability testing .....	42
3.6.1 Specimen Preparation and Grid Strain Analysis System.....	42

3.6.2 Gridding .....	43
3.6.3 Limiting Dome Height Test Equipment .....	44
3.6.4 Data Acquisition and Strain Measurement .....	46
<b>4 Experiment Result .....</b>	<b>49</b>
4.1 Material Characterization.....	49
4.1.1 Metallurgical Aanalysis .....	49
4.1.2 Fusion Zone Microstructure of Different Steels .....	51
4.1.3 Microhardness Analysis.....	54
4.2 Uniaxial Tensile Testing .....	58
4.3 Formability Test.....	65
4.3.1 Effect of Softening on the Formability Properties of Welded AHSS .....	72
4.3.2 Effect of Heat Input on the Formability Properties of Welded AHSS .....	74
4.3.3 Effect of Base Metal Elongation on the Formability Properties of Welded AHSS .....	76
4.3.4 Relationship between Heat Input, Minimum Hardness and the Fracture Location .....	78
4.3.5 Relationship between Uniaxial Strain and Biaxial Strain.....	79
4.4 Summary of the Experimental Results .....	80
<b>5 Numerical Modelling .....</b>	<b>81</b>
5.1 Introduction.....	81
5.2 Theoretical Back ground.....	81
5.3 Experimental Tensile Testing .....	83
5.4 FE Modeling .....	83
5.5 Comparing the Numerical Simulation Results with the Experimental Results .....	86
5.6 Effect of Softened HAZ Material Properties on the Overall Strength and Elongation .....	91
5.7 Effect of Softened HAZ Width on the Overall Strength and Elongation .....	94
5.8 Summary of the Numerical Results .....	98
<b>6 Conclusion .....</b>	<b>99</b>
6.1 Microstructure.....	99
6.2 Tensile Testing.....	99
6.3 Numerical Simulation of Tensile Test .....	100
6.4 Formability Properties .....	100
<b>References.....</b>	<b>102</b>

## List of Figures

Figure 1-1 Strength-Elongation relationships for low strength, conventional HSS, and Advanced HSS steels [1].	2
Figure 1-2 Various tailor welded blank components used in an automotive structure [1].	4
Figure 2-1 Microstructure of Dual Phase steel [10].	10
Figure 2-2 Microstructure of HSLA steel [10].	12
Figure 2-3 Use of tailor welded blank for production of outer door panel of a car body [22].	14
Figure 2-4 Conduction-mode and keyhole-mode laser welding, from [3].	18
Figure 2-5 Influencing factors of welded joints on formability.	21
Figure 2-6 Elongation of different steels for different welding process [33].	24
Figure 2-7 Formability of different welding process [33].	24
Figure 2-8 Formability Vs Different Laser welding parameters [4].	26
Figure 2-9 Steel TWB LDH test result [49].	27
Figure 3-1 Block diagram for the various experimental analyses conducted in this chapter.	33
Figure 3-2 Nuvonyx ISL-4000L diode laser system and Panasonic VR-16 welding robot	34
Figure 3-3 Diode laser welding fixture and shielding gas setup.	35
Figure 3-4 Microstructure of the base metal (a) DP steel (b) HSLA steel	37
Figure 3-5 Cross weld Vicker microhardness measurement for DP980 steel.	39
Figure 3-6 Standard tensile test sample	40
Figure 3-7 Orientation of the tensile test specimens - rolling directions.	40
Figure 3-8 Sub size specimens used in uniaxial tensile tests of TWBs (a) longitudinally welded specimen and (b) transverse specimen (weld line perpendicular to the direction of application of load).	42
Figure 3-9 Micro tensile sample of the fusion zone	42
Figure 3-10 Dimensions of welded blank specimens for biaxial stretching	43
Figure 3-11 Grid etching system.	44
Figure 3-12 MTS 866.02 formability press.	45
Figure 3-13 Die Geometry	46
Figure 3-14 Strain measuring system	47
Figure 4-1 Optical photo - Cross section of a Nd:YAG weld at 6 m/min	49
Figure 4-2 Optical photo - Cross section of a diode weld at 0.7m/min	49
Figure 4-3 (a) SEM photos of base metal and (b) tempered zone in Nd:YAG laser weld	51
Figure 4-4 The fusion zone microstructure of DP450 diode weld for 0.8m/min	52
Figure 4-5 The fusion zone microstructure of DP600 diode weld for 1.2m/min	52
Figure 4-6 The fusion zone microstructure of DP800 diode weld for 0.8m/min	53
Figure 4-7 The fusion zone microstructure of DP980 weld [10].	53
Figure 4-8 The fusion zone microstructure of HSLA weld [10]	54
Figure 4-9 Hardness profiles of DP980 and HSLA steel for diode laser at welding speed of 1.0 m/min [10].	55
Figure 4-10 Hardness profiles of DP980 and HSLA steels for diode laser at different welding speed [10].	55
Figure 4-11 Hardness profiles of DP980 Nd:YAG welds 3 m/min [64].	57

Figure 4-12 Hardness profiles across welds: Diode laser welding with speed of 1.3 m/min. BM is Base metal; HAZ is Heat affected zone; and FZ is Fusion zone. [65] .....	57
Figure 4-13 Relationship between soft zone width, degree of softening to various diode laser welding speed [64] .....	58
Figure 4-14 Typical tested tensile coupons for weld specimens .....	59
Figure 4-15 Typical stress strain curves for DP980 and HSLA transverse and longitudinal tests with the welding speed of 1.3 m/min of diode laser. [10] .....	59
Figure 4-16 Gridded subsize tensile specimen of welded DP980 steel .....	61
Figure 4-17 True stress- true strain curve obtained from the experiment for base metal (DP980) and weld. ....	63
Figure 4-18 log true stress- log true .....	64
Figure 4-19 Representative results of engineering stress versus engineering strain of the uniaxial tensile tests .....	65
Figure 4-20 Typical tested transverse welded tensile coupon indicating fracture at the HAZ during experiment. ....	65
Figure 4-21 The shape of specimens after Dome Height Testing [10] .....	67
Figure 4-22 Side views of the LDH test specimens of (a) DP980 and (b) HSLA steel; weld speed 1.6 m/min [10].....	68
Figure 4-23 Typical limiting dome height results of the base metal and diode welded specimens at 1.6 m/min welding speed [64].....	69
Figure 4-24 Limiting dome height of base metal and diode laser welded samples of different strength AHSS at welding speed: 1.0 m/min [65].....	70
Figure 4-25 Formability ratio of different AHSS (welding speed: 1.0 m/min) [65] .....	71
Figure 4-26 Relationship between reduction in hardness vs. limiting dome height [64] .	73
Figure 4-27 Relationship of formability ratio on the hardness ratio of different AHSS, welding speed 1.0 m/min[65] .....	73
Figure 4-28 Relation between formability ratio and welding speed for welds with both lasers [64].....	75
Figure 4-29 Relationship between formability ratio and the heat input of the welding process for DP980 steel [65].....	75
Figure 4-30 Relationship between formability ratio vs. base metal elongation of same grade of steel with laser weld with same welding parameters (3 kW, 4 m/min) [64] .....	77
Figure 4-31 Relationship between formability ratio vs. base metal elongation of same grade of steel (DP600) with diode laser weld with same welding parameters (4kW, 1 m/min).....	77
Figure 4-32 Softened zone and fracture distance from weld centre for welds with both lasers [64].....	79
Figure 4-33 Relationship between biaxial and uniaxial strain versus weld speed [64] ....	80
Figure 5-1 Schematic view of half the tensile sample. ....	82
Figure 5-2 Mesh for the quarter model of tensile specimen with constraints in the X, Y plane.....	84
Figure 5-3 Comparison of load-elongation curve obtained from experiment and numerical simulation for DP980 steel.....	87
Figure 5-4 Comparison of experimental and numerical result of load vs. displacement in the DP980 steel for diode laser and Nd:YAG laser weld. ....	89

Figure 5-5 Comparison of experimental and numerical plastic strain in the transverse welded tensile specimen of DP980 steel (diode laser welding).....	90
Figure 5-6 Strain localisation is high in softened HAZ in DP980 steel welded sample in experiment and FEM simulation.....	90
Figure 5-7 Variation of maximum load and displacement with respect to decrease in HAZ strength for welded sample with 0.5 mm HAZ width in the simulation.....	92
Figure 5-8 Plastic strain contours in different zones of weldments for HAZ strength of (a) 1300 MPa (b) 1450 MPa during time=0.1996 sec of deformation. ....	93
Figure 5-9 Plastic strain contours in different zones of weldments for HAZ strength of (a) 1300 MPa (b) 1450 MPa during time=3.1996 sec of deformation. ....	94
Figure 5-10 Variation of maximum load and displacement with respect to HAZ width (HAZ strength of 1300 MPa) in the simulation. ....	95
Figure 5-11 Contours of Y-stress during deformation of welded specimen with 4mm HAZ width due to development of constraint force. ....	96
Figure 5-12 Comparison of Y-stress developed in the welded specimen for HAZ width of 0.5 mm and 4mm. ....	97

### List of Tables

Table 2-1 Material properties used by author [33] .....	22
Table 2-2 Welding parameter [33].....	22
Table 2-3 Material properties [4].....	25
Table 2-4 Welding process [4].....	25
Table 3-1 Chemical composition of the different steels .....	38
Table 4-1 Tensile test results of HSLA and DP980 steel of diode laser [65].....	60
Table 4-2 Mechanical properties of DP980 and its weld.....	62
Table 4-3 Diode laser weld orientation on the punch of the formability equipment at 2m/min [64] .....	70
Table 5-1 Fusion zone and the soft zone width obtained during laser welding experiments. ....	88
Table 5-2 Mechanical properties for the HAZ compared to base metal in the welded samples.....	88

# 1 Introduction

## 1.1 Advanced high strength steel

There is a heavy motivation in automotive industries to reduce the weight of the vehicles due to stringent environment policies and to cut down fuel consumption. In this effort, steel manufacturers have come out with various new types of advanced high strength steels (AHSS), which include: dual phase (DP), transformation induced plasticity (TRIP), twinning induced plasticity (TWIP), ferritic-bainite (FB) and martensitic (MART) steels. All of these advanced steels have high strength and fair ductility required for various automobile structures. Hence thinner sheets can be employed for body in white (BIW) structures to make the auto body lighter this is called “down gauging”. Additionally, these steels are Zn-coated or treated so as to prevent corrosion and add environmental protection. Hence, AHSS have been successfully used in automotive manufacturing industries to reduce weight and to improve crashworthiness [1].

Figure 1.1 compares the total elongations and tensile strengths of the different types of AHSS. Tensile strengths of AHSS overlap both the high strength steels (HSS) and ultra high strength steels (UHSS) range of strengths. In general, the AHSS family has greater total elongations than conventional HSS of similar tensile strengths. However there is a reduction in elongation with increasing strength, which can reduce impact performance of these steels. The energy absorbed during an impact test is related to true stress and true strain of that steel. Steel with high strength and high ductility have higher toughness (impact performance).

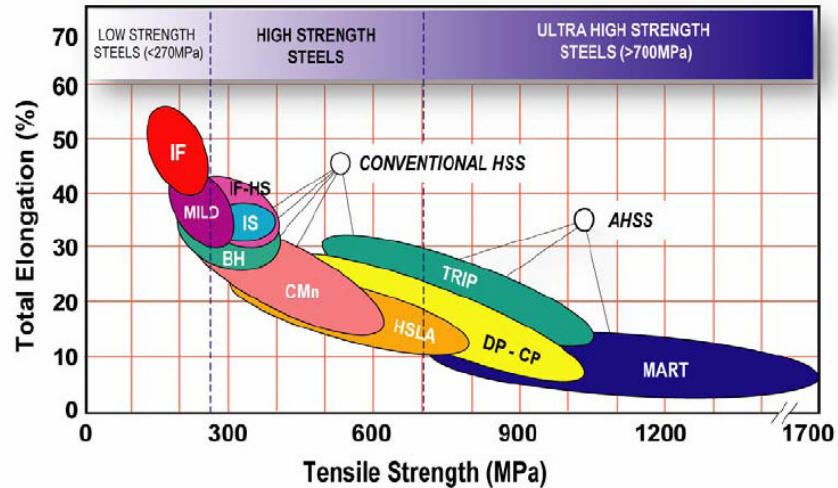


Figure 1-1 Strength-Elongation relationships for low strength, conventional HSS, and Advanced HSS steels [1].

## 1.2 Laser Welding

### 1.2.1 Definition of Laser

The word 'LASER' is an acronym for light amplification by stimulated emission of radiation. A typical laser emits light in a narrow, low-divergence beam and with a well-defined wavelength (i.e., monochromatic, corresponding to a particular colour if the laser is operating in the visible spectrum). This is in contrast to a light source such as the incandescent light bulb, which emits into a large solid angle and over a wide spectrum of wavelength. Since the first laser was developed in 1960, lasers have been deployed in number of applications such as materials processing, lithography, communications, medicines, biology and physics. Various material processing applications use the laser, since the laser beam intensity, average power and flexibility of beam delivery at different locations.

Industrial lasers make use of the laser beam intensity, average power and flexibility of beam delivery for various materials processing techniques. Laser welding process comes under the laser materials processing, which is just one application of high-power lasers [2, 3].

### **1.2.2 Laser Welding Applications**

Metallurgical applications of laser including welding process were initially studied in the year 1962 [3]. Till 1967, various research groups studied the fundamental aspects of laser welding [3].

Laser welding has gained considerable acceptance in the automotive industry because it provides several advantages over other joining processes. Benefits include high productivity, good flexibility, and low maintenance and energy costs along with the ability to produce strong welds.

The majority of high power laser welding installations in the automotive industry consist of CO<sub>2</sub> and Nd:YAG lasers in the power range of 3 kW to 6 kW. The laser focal spot is targeted on the workpiece surface which will be welded. At the surface the large concentration of light energy is converted into thermal energy. The surface of the workpiece starts melting and progresses through it by surface conductance. For welding, the beam energy is maintained below the vaporization temperature of the workpiece material.

Weld depth and width depend on the process parameters, which are: laser power, speed, focuses spot size and position shield gas flow and direction. The laser weld is a non-contact process, an easily controlled tool, and well suited to automation or CNC systems. The possibility of switching the beam from one laser source to several workstations allows optimum use of the laser for a combination of assembly and welding functions. Inherent laser weld process flexibility helps satisfy automotive production requirements without extensive set up for different part geometries. Laser welds show fairly narrow cross sections and therefore require parts to be precisely manufactured and positioned. Low heat input and thermal distortion reduce secondary machining requirements. The process is also capable of welding a variety of joint configurations and material combinations.

### **1.3 Tailor Welded Blanks**

Automotive structural assemblies often comprise individually formed stampings that are then spot welded together into a larger structural part. Alternatively, the use of tailor welded blanks (TWBs) can eliminate many sub-assemblies with one stamped component

that has targeted strength in only the areas where it is required. This eliminates the added cost of stamping and assembling multiple parts, which increases structural integrity. Tailor welded blanks involve the butt / lap welding of two (or more) different sheet thickness or alloys to form a multi-gauge and/or multi-alloy blank. This can also reduce the weight of automotive panels. In this way, the blanks can be tailored for a particular application, not only as to shape and thickness, but also by the use of different quality sheets (with and without coating). The use of TWBs at a mass production level was started in Europe (Germany) in the early 1980s, and thereafter the practical use expanded rapidly all over the world [4]. TWBs are currently used for the body side frames, door inner panels, motor compartment rails, center pillar inner panels and wheelhouse/ shock tower panels as seen in Figure 1.2.

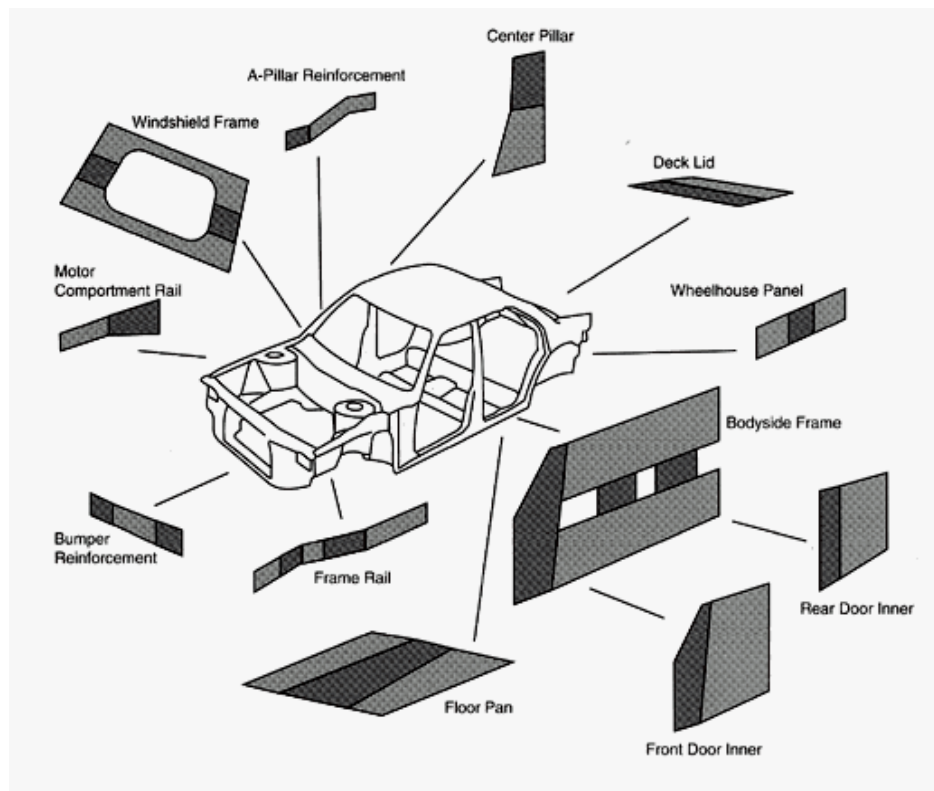


Figure 1-2 Various tailor welded blank components used in an automotive structure [1]. The different types of welds are identified for TWB applications and those include:

- a. Laser Beam
- b. Resistance Mash Seam
- c. High Frequency Induction

#### d. Electron Beam

By far, laser tailor welded blanks have found the widest applications in the automotive industry [1].

### **1.4 Problem and Justification**

From the previous section, it is understood that both advanced high strength steels and tailor welded blanks have potential to reduce weight of vehicles. Hence there is a high level of interest in using advanced high strength steels in TWBs for further mass reduction and structural performance improvement. It is recognized that during laser welding in steels, heterogeneous material structures are developed across the weld region, which will influence the performance of the welded steel. The surrounding HAZ contain regions that may be harder or softer [5].

Because of the growing importance of TWBs and the associated forming problems, formability of TWBs is an extremely important area of research. The present study deals with forming behaviour of TWBs with respect to the material properties. Further predictive numerical model results that would evaluate the problem of the tensile properties aspects of these welded steels are studied.

### **1.5 Objective**

The objective of this research work is to investigate and develop a better understanding of the effect of laser welding on the formability aspects of the AHSS. To facilitate this, clear objectives are formulated to study the effect of welding parameters on the formability properties.

- |           |   |
|-----------|---|
| Stage I   | Optimise laser welding parameters and investigate material and mechanical properties. |
| Stage II  | Evaluate the formability of laser welded AHSS for tailor welded blank applications.   |
| Stage III | Develop a numerical simulation for uniaxial tensile test of laser welded AHSS.        |

The experiments were designed to develop in depth understanding of the effect of process variables, microstructure, and property relationships so as to develop a fundamental understanding of the effect of laser welding on the formability of the AHSS.

## **1.6 Criteria and Constraints**

Laser welding is a welding process which is widely used in the TWB applications for the automobile production. Numerous standards exist, which details procedures for mechanical testing of the welded AHSS. In this study, standards governed by the American Society for Testing and Materials (ASTM) were used as criteria for testing laser welded AHSS. The scope of the research project is limited to five materials, which includes one HSLA as benchmark and four DP steels. Material thickness is restricted to 1 to 1.2 mm and only two type of lasers of (diode 4KW and Nd: YAG 3KW) were selected for the welding process. The systems selected for the experimentation have simple bead on plate (butt joint with full penetration welding) in order to avoid the geometrical defects during the laser welding process.

## **2 Literature Review**

Formability is the ability of sheet metal to be formed into a desired shape without failure. When a sheet metal fails by localised necking and fracture during manufacturing, a common practice is either to redesign the part or to change the processing method so that the state of strain in critical region will not exceed the limit of deformation (the forming limit). Therefore evaluation of formability of sheet metals prior to actual manufacturing is very useful for correcting failures. Sheet metals are a critical material for vehicle design, and have good weldability and formability. Low carbon and ultra low carbon steel sheets have long been the work-horse materials in automotive and consumer industries because they can be stamped into inexpensive, complex components at high production rates. In recent years, the development of AHSS steels has made curiosity for automotive industries to apply these steels to auto body components. Hence a brief review of formability and weldability of advanced high strength steels in the context of tailor welded blank application is presented below.

### **2.1 Formability of Sheet Metals**

Flow localization is an unstable flow where the deformation is confined to one zone of the sheet metal. This is also referred to as onset of necking, which leads to fracture on further deformation [41]. When a stamping tears during forming, the tear is a visible indication that metal has been worked beyond its prevailing forming limit. Whether or not a particular sheet of metal can be formed without failure depends on many factors such as material properties, surface conditions, blank size and shape, lubrication, press speed, blank holder pressure, punch and die design. Because of this, source of flow localization problem is difficult to pin point and quantify. Hence formability is an attribute that has no precise, universal meaning. Because of multitude of materials, stamping designs and press conditions, there are no standard valid rules for improving the formability of a stamping through changes in tool design or process parameters [42].

To evaluate formability, some laboratory scale simulative tests have been developed [42]. The simulative tests subject sheet metals to the deformation that occurs in a particular forming operation. Examples of these tests include Erichsen test, Olsen test, Fukui

conical cup test and Swift flat bottom test [42]. Swift flat-bottom cup test and Sach's wedge draw test are used to simulate deep drawing. Combined stretching and drawing are simulated in the Fukui conical cup test and some times the round-bottom cup test is also used. The Erichsen and Olsen tests were the first tests developed to estimate sheet metal formability under pure stretching conditions. In Erichsen cup test, flat polished die plates with 27 mm circular opening are used to clamp a sheet specimen, which is then penetrated by a 20 mm steel ball. The height of the cup at fracture is the Erichsen cup height. The Olsen test is done with a 7/8 inch ball and a 1 inch die opening.

Each simulative test evaluates only one of the many possible forming conditions. So, these tests can not produce complete information about forming behavior of a sheet under all possible combination of deformation modes. Therefore, none of the simulative tests give a reliable overall formability index for a stamping operation. The other problems associated with these tests are: insufficient size of penetrator, inability to prevent complete drawing-in of the flange and their inability to correlate with press performance. It is extremely difficult to achieve excellent reproducibility of results from these tests even with the same experimental set up [77, 78].

Hecker [77] developed a modified hemispherical cup test by scaling up the penetrator size to 101.6 mm, adding a draw-bead in the die plates near the die opening, and running the tests dry (without lubrication) thereby eliminating problems with the Erichsen and Olsen cup tests. This modified test is known as the limiting dome height (LDH) test. The reproducibility of the results is higher in LDH test and correlation between cup height and n-value for low carbon steels is good. Ghosh [79] modified the Hecker test to simulate plane-strain condition, as more than 80% of the stamping failures occur close to plane-strain condition.

A new test called OSU formability test was developed by Miles et al.[80] in which an elliptical punch was used to evaluate several coated and uncoated sheet materials. The results showed that the reproducibility was better compared to LDH test. Good correlation was found between the OSU and LDH tests. The OSU test was found to be suitable for only materials with low r-values as there was excessive lateral strain for materials with high r-values (>1.5). Also, the elliptical geometry of the punch is difficult to fabricate compared to a hemispherical punch.

## **2.2 Advanced High Strength Steel**

Advanced High-Strength Steel (AHSS) is designed and manufactured for automotive application with focus on press-forming and fabrication processes for under body, structural, and body panels. When selecting conventional high-strength steels to replace mild steel or other traditional grades, reduced formability is often one of the undesired consequences. To overcome this, and to further achieve lower mass automotive structures, recent steel developments have targeted improvements in formability. The AHSS family of multi-phase microstructures typifies the steel industry's response to the demand for improved materials that utilize proven production methods. These engineered materials address the automotive industry's need for steels with both higher strength and enhanced formability [1].

### **2.2.1 Metallurgy of AHSS**

The fundamental mechanical properties like hardness, yield strength, ultimate tensile strength and total elongation were initially used as a rough indication of formability of sheet metal. The metallurgy and processing of AHSS grades should be understood clearly as they provide a baseline understanding of these mechanical and material properties.

### **2.2.2 Dual Phase (DP) Steel**

Dual phase steels are essentially low-carbon steels that contain a large amount of manganese (1-2 wt.%) and silicon (0.05-0.2 wt. %) as well as small amounts of microalloying elements, such as vanadium, titanium, molybdenum, and nickel [1]. A dual phase steel is created by heating a low-carbon micro-alloyed steel into the intercritical region of the Fe-C phase diagram between the  $A_1$  and  $A_3$  temperatures, soaking it so that austenite forms, slowly cooling it to the quench temperature, and then rapidly cooling it to transform the austenite into martensite [1,6]. Upon quenching, the austenite is converted mostly to martensite, but will also partially be converted into ferrite if the cooling rate is not sufficiently high [7, 9]. Also, depending on the cooling rate, the austenite may be converted at least partially into bainite [8].

The ferrite that forms from austenite is referred to as epitaxial ferrite. The microstructure of dual phase steel, consisting of ferrite and martensite, is as shown in Figure 2-1 [9, 13].

Epitaxial ferrite grains, shown in Figure 2-1, are distinguishable from proeutectoid ferrite through use of an alkaline chromate etch [12]. All three constituents have a large effect on the mechanical properties of the steel. Epitaxial ferrite has a negative effect on the mechanical properties. It dramatically lowers the tensile strength and slightly increases the ductility of the steel [11].

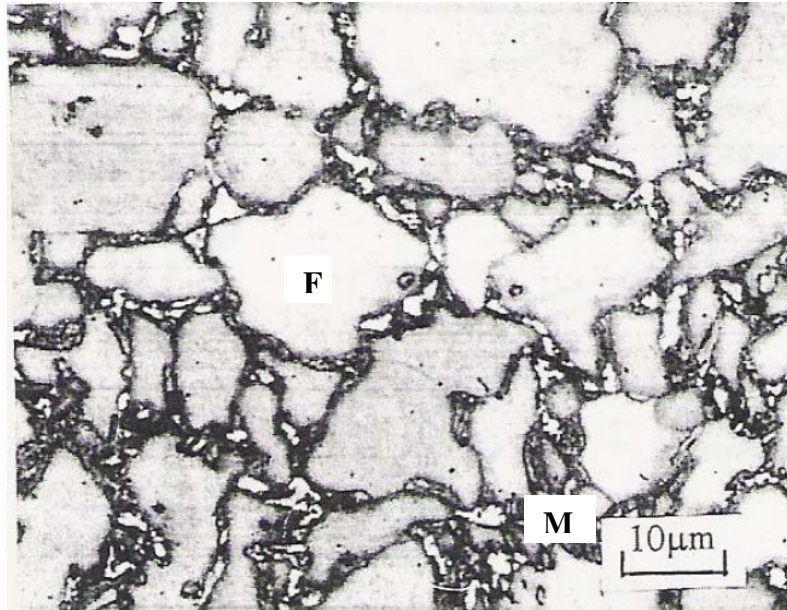


Figure 2-1 Microstructure of Dual Phase steel [10]

The reason for this is that the epitaxial ferrite forms stress concentrations in the martensite grains, which compromises its strength [11]. Thus, epitaxial ferrite is undesirable and effort is made to ensure that it does not form. Upon quenching a dual phase steel, residual stresses are created at the martensite-ferrite interfaces due to the volumetric expansion of the martensite [6, 13]. This creates an increased number of dislocations at these interfaces. Because the vast majority of the alloying elements are found within the martensite, the density of mobile dislocations within the ferrite matrix is quite high [6].

One important characteristic of dual phase steels is that the 0.2% offset yield strength increases as the martensite content increases, but is not affected by the carbon content [15]. Leidl et al. [13] showed that the increase in yield strength is due to the residual stresses which are created in the ferrite due to the volumetric expansion of the martensite.

As the amount of martensite increases, so does the residual stress in the ferrite matrix, which causes the yield stress to rise. As would be expected, the strength of dual phase steels increase as the amount of martensite increases, and also when the martensite is more finely dispersed [6, 14, 16].

Another characteristic of dual phase steels is that they exhibit continuous yielding [6, 11, 13]. This is unusual for low-carbon steels; most show an elongated yield point followed by strain hardening. The reason for this is that there is a higher dislocation density in dual phase steels than in other low carbon steels. This higher mobile dislocation density in dual phase steels allows for the continuous yielding [6, 17, 18].

Dual phase steels have been developed only recently but, due to their promising mechanical properties, have been studied in great detail. Unlike most low-carbon steels, they do not exhibit discontinuous yielding unless they are annealed. They exhibit high tensile strength and moderate ductility, which is not significantly affected at elevated strain rates. This illustrates the promise for dual phase steel; it can be used to reduce vehicle mass, while providing good energy absorption at high impact velocities.

### **2.2.3 High Strength Low Alloy**

High Strength Low Alloy Steels (HSLA) is another type of steel which already in widespread use for reducing the weight of automobiles. Not only do they show good strength, formability and weldability, but their cost is lower than equivalent heat-treated alloys because they achieve their desired characteristics directly from hot rolling [19]. They have been used for automotive applications as well as warships, off-road trucks, offshore platforms, and equipment for oil-wells [19].

HSLA steels typically have a ferrite-pearlite microstructure as shown in Figure 2-2. They were developed in the 1960s by adding niobium, vanadium, and titanium to form precipitates in low carbon high manganese steels [20, 21]. These elements, when added to the steel, create Ti-N, Nb-N, and Nb-C precipitates [22], which increase the strength of the steel, but affect its ductility and weldability, as the toughness increases [23]. They also increase the strength of the steel by retarding the growth of the ferrite grains during cooling [21].

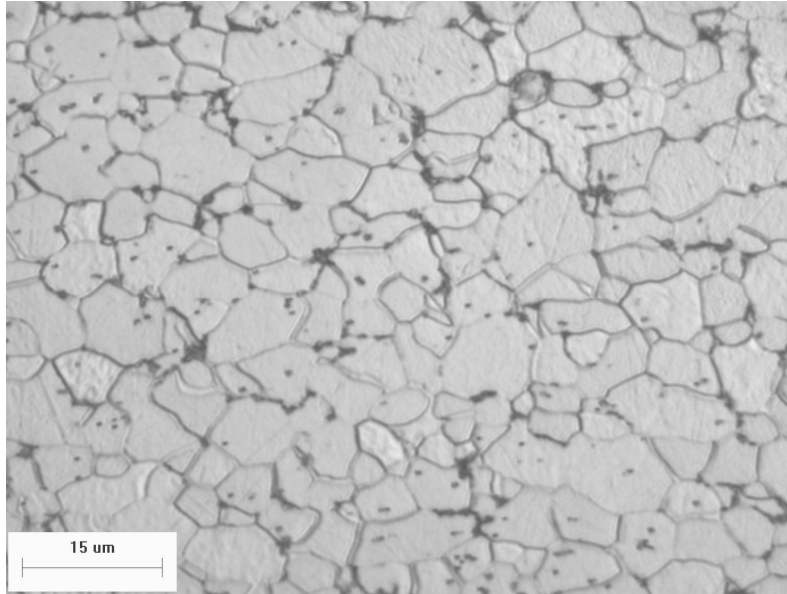


Figure 2-2 Microstructure of HSLA steel [10]

Using the DP980 grades in appropriate applications offers opportunities for reduced product weight, enhanced crash performance, manufacturing process consolidation, and cost reduction. However, because these grades have different microstructures, chemistries, and properties, forming die processing must be optimized to take advantage of the differences.

### 2.3 Formability of AHSS

The authors Shi et al [44] discuss five different materials that were included in their comparative study of formability of one HSLA and four DP steels. DP steels have greater ratio of tensile strength over yield strength than HSLA steel. Higher tensile strength of DP steel correlates to better crash performance of automotive components. Additionally a 10% potential weight reduction is available through down gauging by replacing the conventional HSLA with similar yield strength dual phase steel while maintaining equivalent crash performance. The DP steel had enhanced the material's resistance to bucking and wrinkle during axial feeding in tubular hydroforming processes when compared to the HSLA steel [45].

AHSS have inherent high strength, attractive crash energy management properties and good formability which significantly contribute to light weight vehicle and fuel economy [46]. Sriram et al [46] work dealt with data on relevant intrinsic mechanical behaviour,

splitting limits, and springback behaviour for several samples of mild, conventional HSS, AHSS, and UHSS. In general it was concluded that formability as determined by the different tests decreased with increasing the tensile strength.

Kamura et al [47] compared the formability aspects of eleven different grades of galvanealed steels and concluded that formability of TRIP steel is equivalent to DP steels on most forming modes. Formability of the TRIP steel was superior to DP steel for the lower punch shoulder radii, however DP980 steel showed a similar formability of TRIP steel in the higher punch shoulder radii.

## **2.4 Progress in Tailor Welded Blank Applications**

Automakers are constantly searching for innovative means of reducing vehicle weight and manufacturing costs in order to meet fuel economy standards while remaining economically competitive. Tailor welded blanks (TWB) is one of the solutions to meet these conflicting requirements. Tailor welded blanks are blanks where multiple sheets of material are welded together prior to the forming process.

Currently tailor welded blanks are used for manufacturing auto body parts such as front door inner, rear door inner, floor pan, A-pillar, centre pillar (B-pillar), body side frames etc. One typical example is the production of an automobile outer side panel as shown in Figure 2-3. Five different pieces are first blanked: four of them are 1 mm thick, one is 0.8 mm thick. These pieces are laser butt welded and then stamped into the final shape. In this way, the blanks can be tailored for a particular application, not only as to shape and thickness, but also by the use of different quality sheets (with and without coating) [22]. In another example, the required strength and stiffness for supporting a shock absorber is achieved by welding a round piece on the surface of the large sheet. The sheet thickness in these components varies, depending on its location and contribution to characteristics such as stiffness and strength, while allowing significant weight and cost savings.

European, Japanese and North American car makers, including Volvo, Mercedes-Benz, BMW, Nissan, Toyota, GM and Ford are using tailor welded blanks in the design and manufacture of their automobiles. Globally, the market for tailored blanks has grown from about 120 million parts in 2001 to nearly 250 million parts in 2005 [23].

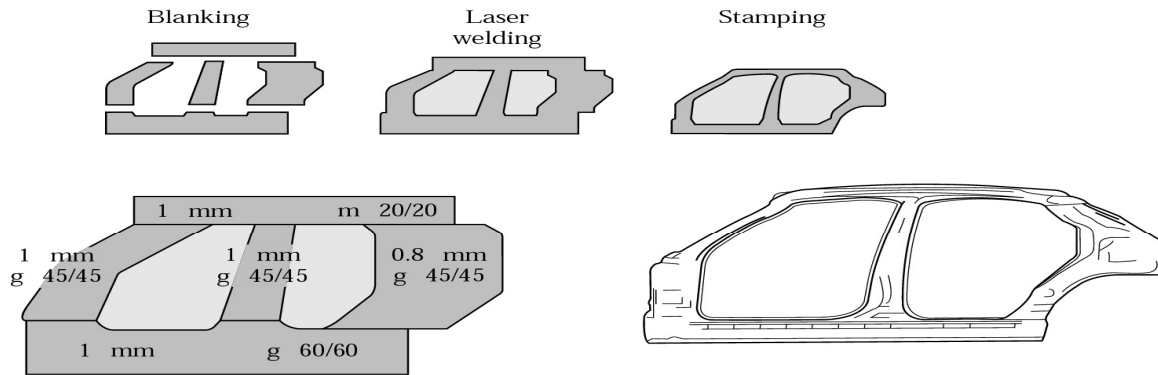


Figure 2-3 Use of tailor welded blank for production of outer door panel of a car body [22]

While the use of TWBs in auto body manufacturing is increasing, the potential application of TWBs in consumer products, packing and construction industries are yet to be explored [24]. The Tailored Steel Product Alliance (TSPA) [25] is an organization that assists automakers in their application of tailored products by optimizing the performance of the products and thereby expanding applications and the markets for the products. The member companies of TSPA are involved in promoting application of TWBs globally. For automotive applications involving laser welding of thinner sections (in this study), no weld consumable or filler wire is used. The laser weld produces a butt-joint with a narrower heat-affected zone (HAZ), as compared to other processes. In the resistance mash seam welding process, the HAZ is about twice the width of the laser weld. The other identified advantage of laser welding is better appearance. A laser beam can be used to weld a maximum weld length of about 3800 mm and the use of a multi-axes robotic system with dual laser beam makes it possible to weld a curvilinear weld. All these factors and especially the narrower HAZ have made laser welding popular for manufacturing TWB [1].

However, this technology presents several challenges to the design and manufacturing engineers due to several additional manufacturing issues that arise due to stamping of a

'pre-welded blank' and these issues can be segregated into three different categories [Auto/Steel partnership, 1995].

(a) Pre-forming issues:

1. Welding technique and weldability of the materials of different grades, thickness and coatings.
2. Optimization of the weld parameters for getting sound weld by proper inspections and testing technique.
3. Weld length, orientation and shape (linear or non-linear) and automation of the welding process to get the desired weld geometry.
4. Material optimization by part integration considering the weight reduction of the part.
5. Handling and shipping of the welded blanks.

(b) Forming issues:

1. Design of tools for incorporating thickness differences.
2. Formability changes due to difference in thickness, strength and tool-blank interface friction.
3. Effect of properties of weld and heat affected zones on formability.
4. Effect of weld orientation on strain distribution.
5. Weld line movement during forming.
6. Spring back.

(c) Post-forming issues

1. Performance issues like crashworthiness, fatigue strength, structural integrity and extent of weight reduction.
2. Overall cost analysis taking into account of all tangible and intangible benefits.
3. After sales service.

Progresses made against these issues are discussed in brief. The quality of the weld in a TWB is critical for a successful forming operation and it depends on the welding technique, composition of parent metals and the weld structure. Eisenmenger et al. (1995) used design of experiments to study the effect of laser welding parameters on formability of welded blanks for two different material combinations of cold rolled steel. Dome tests, hole expansion tests, transverse and longitudinal tension tests were used to evaluate the

formability of the welded blanks. It was found that misalignment and gap are two critical weld parameters that influence quality of welded blanks and hence formability. Higher shield gas flow rate and welding speed enhance formability of the welded blanks and minimize the premature failure in the weld. Weld with larger concavity had high premature failure rates. Waddell et al. (1998) studied the influence of laser weld zone on formability of TWBs in steels with yield strength in the range of 150 MPa to 585 MPa. It was found that average failure height in Erichsen cup test of laser weld blank was influenced by a combination of weld hardness and the weld width with the role of weld hardness being more predominant. The main factor that controls the hardness of the weld is the composition (carbon equivalent) of the base metal. Steels with same yield strength can result in welds with significant differences in formability depending on their composition.

Formability and weld zone analysis of tailor welded blanks of cold rolled steel sheets with various thickness ratios were studied by Chan et al. (2005). Nd:YAG laser butt welding was used. The transverse tensile tests showed that there was no significant difference between the tensile strength of TWBs and the base metals. Metallographic and microhardness studies were done to see the morphology and hardness of parent metal, HAZ and weld zone respectively and increase in hardness of the fusion zone by 60% was observed.

## **2.5 Laser Welding Technology**

### **2.5.1 Laser Principle**

The operation of lasers is dependent upon stimulated emission. When atoms or molecules in certain materials become excited by an energy source, they can emit photons at specific wavelengths as they return to the unexcited state. Photons emitted then travel inside of a laser cavity, where they are reflected to travel back and forth along the length of the cavity by reflective surfaces. In the travel path, these photons may strike other excited particles and stimulate them to emit photons as well. After stimulated emission, there are then two photons of equal energy travelling in the same direction. In order for a material to be an efficient lasing medium, population inversion must be possible; this

requires the material in its excited state to have a longer lifetime than its lower energy/ground state. This condition permits the material to release its energy when stimulated, rather than releasing the energy spontaneously on its own or self excitement. The lasing medium is continuously pumped to produce excited particles to sustain the system. Some of the laser light is allowed to leave through an opening or through partial transmission of one of the reflective surfaces to form a laser beam. The laser beam is then focussed by optics and delivered to the application [2, 3].

Weld penetration, depth and shape of the weld cross section is determined by many factors including the joint geometry, thermal characteristics of the metals, and the laser parameters. For this discussion the focus is on the basic laser beam interaction as a vital point to the different laser welding modes of penetration. Two distinct modes of laser welding apply depending on the power density [25]. These are conduction mode, and keyhole mode welding.

### **2.5.2 Conduction Mode Welding**

In conduction-mode welding, the laser energy is absorbed at the surface of the workpiece and the weld pool is developed as heat is conducted through the material. Figure 2-4 illustrates weld pool cross-sections in conduction and keyhole-mode welding.

At low power density, the melt puddle depression does not occur and the laser energy input creates a smooth shallow liquid pool. This pool will grow in size until the laser energy delivered into the puddle equals the energy lost to conduction into the rest of the solid metal. Upon solidification of the puddle, a cross section of the parts will show a weld that generally has a penetration no greater than half the width of the weld. The surface of the weld is very smooth and cosmetic because the melt puddle will not shrink back during solidification.

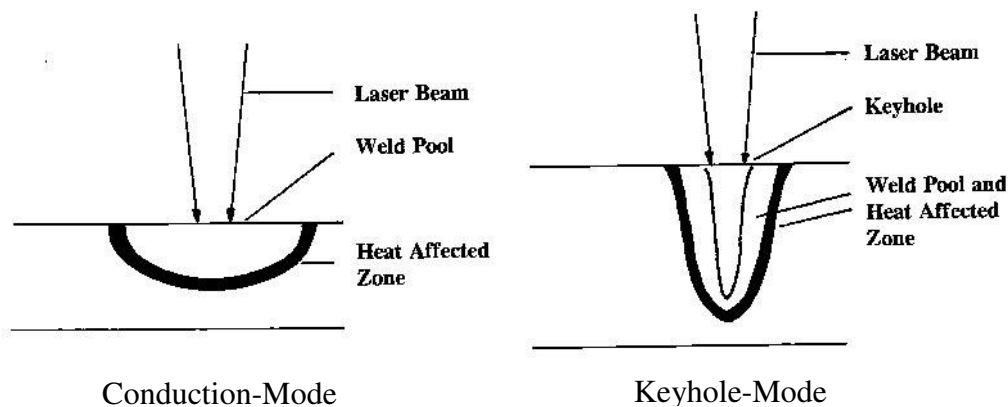


Figure 2-4 Conduction-mode and keyhole-mode laser welding, from [3]

### 2.5.3 Keyhole Mode Welding

In keyhole-mode welding the laser beam penetrates the surface of the weld pool by vaporizing some material. Narrow, deep penetration welds are possible with keyhole-mode welding. In this mode, intermittent closure of the keyhole can cause gas entrapment and porosity in the weld. Conduction-mode welding does not suffer from this problem because there is less perturbation to the system [3]. The nature of the physics of the keyhole leads to this instability. The existence of a keyhole relies on a balance between vapour pressure and surface tension inside of the keyhole column. The vapour pressure is highest at the bottom of the keyhole, while surface tension is usually highest at the top of the keyhole. At the top, the keyhole is unstable because the surface tension tending to collapse it exceeds the vapour pressure tending to expand it. This imbalance leads to intermittent collapsing of the keyhole from the top down, which can lead to occluded vapour pores at the root of the weld and inconsistent penetration [27].

Keyhole-mode welding is also associated with very high fluid velocities in the molten metal of the weld pool. A thin layer of molten material is present surrounding the keyhole opening, which is forced to flow from the front of the weld pool toward the back of the weld pool by surface tension differences caused by temperature gradients in the weld pool. The fluid velocity in a keyhole weld has been calculated to be as high as 3000 mm/s [28].

The depth of the keyhole is determined by the continuous wave (CW) power or peak power of the laser for pulsed units. The lower the average power, the shallower the

keyhole before conduction losses equal laser power and the keyhole depth limit is reached. When one moves the keyhole across the workpiece during a seam weld, the fusion front penetration is determined by the keyhole depth. As the processing speed is increased, the keyhole depth will decrease but the weld cross section will retain a keyhole or “nailhead” geometry. At slower speeds, the weld penetration will increase to a virtual maximum determined by the keyhole depth of near zero travel speed.

## **2.6 Advantages of Laser Welding**

There are number of methods for joining metals: Arc welding, Friction stir welding (SFW), Resistance spot welding (RSW), Electron beam welding (EBW) and Laser beam welding (LBW). Generally arc welding cannot be used without adding filler metal, whereas laser welding is used without filler metal.

The disadvantages of mash welding were the number of moving parts that required maintenance, welding of coated materials, possible corrosion due to coating removal during weld, wider HAZ, and increased weld bead thickness due to the overlapped edge. As in laser welding the width of weld zone is very narrow, hence the corrosion resistance of the weld zone is enhanced. In the keyhole mode welding, lasers have higher energy density that produce narrow, deep penetration welds at speeds much higher than those of arc welding processes. Since the energy density is high, a greater fraction of the energy absorbed by the workpiece is utilized in generating the weld pool and as a result, HAZ are narrow [29]. An important issue remains relative to formability differences, which suggests that the harder but narrower HAZ from laser welds in many applications is advantageous over the mash weld [1].

An advantage that is more particular to the automotive industry is the one-sided nature of laser welding. Many automotive sheet metal components are joined by resistance spot welding, which requires access to the joint from both sides of the lap interface. Because of the limited joint design flexibility inherent with resistance spot welding, it has become standard in the automotive industry to design components either with flanges or with accessible overlapping areas [30]. Laser welding allows joining of sheets where access to only one side is possible, allowing greater joint design flexibility. Laser welding presents opportunities to the automotive industry for new design concepts which may allow even

greater efficiency in material usage, resulting in greater weight reduction and cost savings.

In addition, laser welding is a non-contact process, whereas resistance spot welding requires contact with the sheet surfaces which leads to electrode wear. Increased costs and decreased production are associated with dressing and replacing worn electrode tips for RSW [31].

## **2.7 Limitations of Laser Welding Technology**

Most industrial processes employing laser welding utilize keyhole-mode welding since it gives deep penetration and fast welding speeds. The rapid fluid motion that is associated with keyhole-mode laser welding and instability of the keyhole often lead to rough andropy bead surfaces [25]. This can be a disadvantage in applications when the weld surface appearance is important, for example, in automotive applications where the weld will be visible. However the conduction mode laser welding does not have this issue, but only slower welding speeds are possible as they have lower power density.

## **2.8 Laser Welding of Advanced High Strength Steel**

Incorporating AHSS in tailored blanks using laser welding, automakers can improve designs of automotive parts by combination of strength, formability, and crash energy. However, before analysis of forming characteristics of TWBs, various weldability issues must be understood in order to design and produce high-quality parts with reasonable production and tooling costs. So most of the initial works were on the process development and optimization of the laser weld process [32, 33, 34]. Different types of lasers available for welding commonly used are the CO<sub>2</sub>, Nd: YAG [35, 36, 37]. High power diode laser (HPDL) is particularly well suited for welding of butt and lap-fillet joint geometries in aluminium sheet for automotive applications [38, 39, 40]. Herfurth and Ehlers [40] have shown the applicability of using an HPDL for welding butt joints and tailor-welded blanks in aluminum sheet. It was found that the conduction-mode welding of the diode laser was advantageous in joining sheet metal parts due to a larger melt pool and therefore good gap-bridging ability. Diode laser welding allowed for a smooth transition between parts and excellent weld appearance.

## 2.9 Factors Influencing Formability of Tailor Welded Blanks

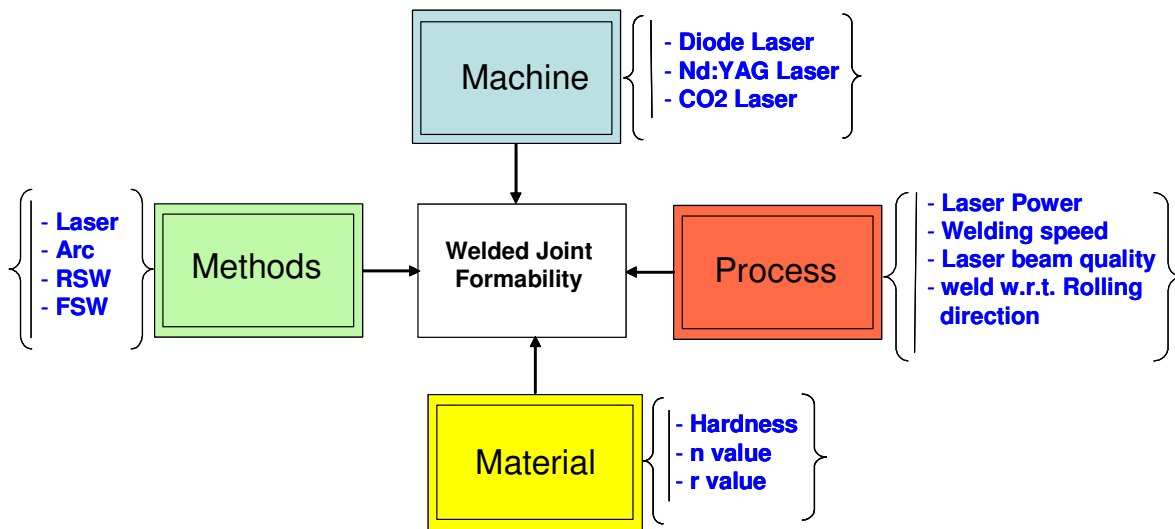


Figure 2-5 Influencing factors of welded joints on formability

Figure 2-5 represents the different factors influencing the formability of a welded joint. Despite their numerous benefits, forming TWBs is challenging due to a significant reduction of formability associated with a welded blank. To predict the forming behaviour of a tailor welded blank, it is essential to have a clear understanding of the important changes that occur during forming of a tailor welded blank. Some of them are

- material property changes in the heat-affected zone (HAZ) of the weld,
- non-uniform deformation because of the differences in thickness, properties and/or surface characteristics,
- effect of welded zone on the strain distribution, failure site and crack propagation
- weld line movement during deformation.

Among these complexities in formability of the TWBs welding process gives certain major roles. The sources of factors from welding process that influence formability can be classified into four major areas namely methods of welding, types of welding machine, process parameters used during welding and material properties (base materials and changes in material properties in the weld and HAZ). This section is going to discuss briefly about these factors on the formability of welded sheets.

## 2.9.1 Methods

Different methods of welding are available. Uchihara et al [33], compares 3 types of welding methods, viz. Plasma arc weld, Mash seam weld and Laser weld for AHSS. Different materials and welding parameters used in their work is given as below in the Table 2.1 & 2.2. They conducted two types of test:

1. To determine an upper steel strength limit that can be welded and the best welding method for the higher strength steel grades (780 MPa and above).
2. To find the best welding process that has higher formability of the AHSS (590 MPa).

Table 2-1 Material properties used by author [33]

	Mark	Thickness(mm)	Yield Strength(MPa)	Tensile strength(MPa)	EI (%)	
<b>Test 1</b>	270 E	1	163	306	49.3	
	270 C	1	215	339	42.6	
	440	1	308	447	34.8	
	590	1	415	630	27.2	
	780	1	432	826	21	
	980	1	677	1048	15.8	
<b>Test2</b>	590	A	1.4	463	605	27.1
	590	B	1.4	508	597	26.3
	590	C	1.4	408	636	27.2
	590	D	1.4		617	33.3
	590	E	1.4	400	607	35.7

Table 2-2 Welding parameter [33]

	(a) Laser Welding		(b) Mash seam welding		(c) Plasma arc welding	
<b>Test 1</b>	Laser	YAG Laser	Current	18kA/270-780steel	Current	80A
	Power	3kW		16kA/980steel	Speed	1m/min
	Speed	6.5m/min	Force	10kN/270steel	Chip hole dia.	2.8mm
	Focus	Surface		12kN/440,590steel	Plasma gas	Ar+10%H2
	Shielding gas	Ar (20L/min)		14kN/780,980steel		(0.5L/min)
			Lap	2.5mm	Shielding gas	Ar+10%H2
		Speed	4m/min		(10L/min)	
<b>Test 2</b>	Power	3kW	-		Current	120A
	Speed	4.5 m/min			Speed	1m/min

The welding parameters for the different welding process are tabulated as test1 in table 2.2. Figure 2-6 shows tensile test results of the perpendicular to the weld line. The base metal elongation was within the range 41 % -18.2% for different tensile strength steel 270- 980 MPa respectively. The mash seam welded and the arc welded DP 780 MPa fractured in the HAZ, whereas the fracture of the laser welded DP780 is not in the HAZ.

The arc and mash seam welding has a larger heat input into the material, generating a wider fusion zone, deep and wider HAZ. However, laser welding has a narrower fusion zone, shallow and narrower HAZ. The hardness traverse showed a softening in the HAZ of the arc and mash seam weld of the DP780. Hence, the elongation of arc and mash seam welded steels reduced drastically. However, Uchihara et al [33] did not explain the reason for the softening in the HAZ.

The laser welded DP980 MPa steel is fractured in the HAZ; however the drop in elongation is small due to smaller softening dimension in the HAZ. The elongation of the laser welded specimens for different strength steels considered in their work is closer to the base metal elongation compared to the other two processes (Arc and Mash seam weld). These results suggest that a weld with a shallow and narrow softening zone in the HAZ could be used in the industries.

Uchihara et al [33] concluded that laser welding is the best welding process because of the narrow weld and small heat input. Laser welding is the most suited weld process for higher strength steels.

Another part of their work was on the formability of the same grade (590 MPa) steel welded with different methods. Figure 2-7 represents the result of limiting dome height tests in which major strain was applied in welding direction. The dome heights of the laser welded steels were almost the same as that of the base metals. The dome heights of the plasma arc welded steels are smaller than that of the laser welded, especially in the materials A & B (similar ultimate tensile strength but different chemical composition). Their work concludes that laser welding is the best welding process for the AHSS steel.

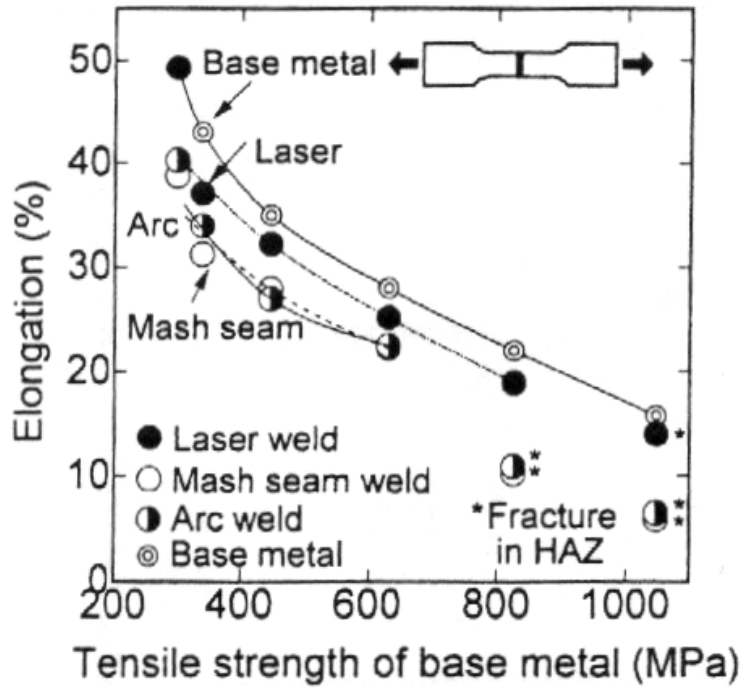


Figure 2-6 Elongation of different steels for different welding process [33]

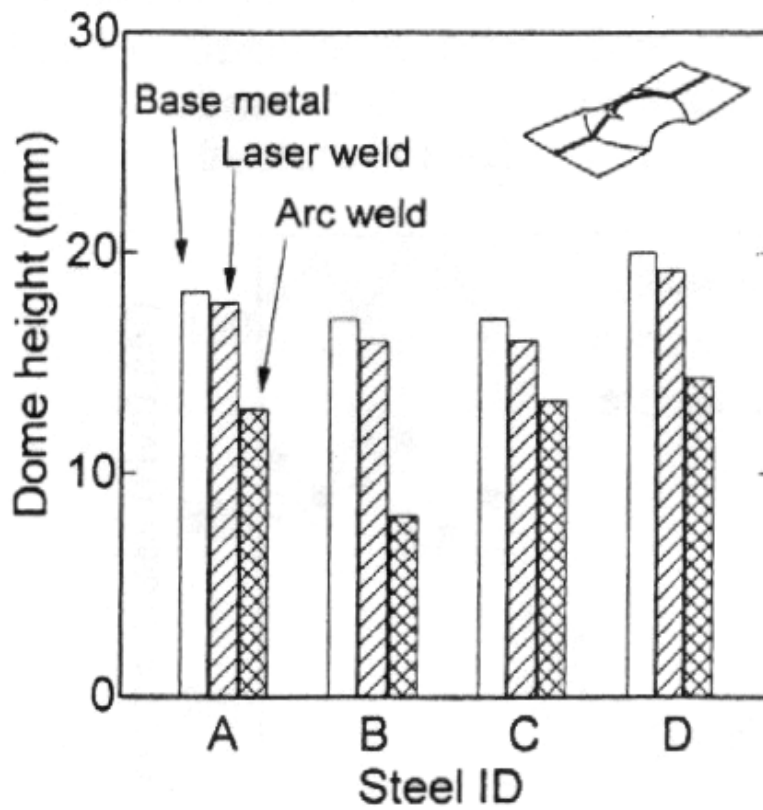


Figure 2-7 Formability of different welding process [33]

### 2.9.2 Process

Bruce et al [4] compares the laser weldability of higher strength AHSS. Table 2.3 and Table 2.4; show the material properties and welding parameters considered in their work. The two different welding parameters produced two weld seams that approximately measures 1 mm and 2 mm weld width. The narrow weld width was created with 6kW of CO<sub>2</sub> laser power at 7m/min. In contrast, the wider weld width was produced with 3kW of CO<sub>2</sub> laser power at 4m/min. Figure 2.8, measured the biaxial stretch formability of a laser weld in an Erichsen test and related to the weld hardness and weld width. It is evident from the test, for higher welding speed and power; formability is higher as net heat input is lower leading to smaller softened HAZ, whereas a higher heat input of 3kW laser exhibits a significantly larger softened HAZ.

Table 2-3 Material properties [4]

Material	Thickness (mm)	Yield Strength (MPa)	Tensile Strength (MPa)	Elongation (%)	n value
GA 980 (DP)	1.20	550	971	19.2	0.110
CR 980 (DP)	0.99	848	1037	15.5	0.102

Table 2-4 Welding process [4]

Laser machine	Laser type	Power (W)	Welding speed (m/min)
ProCoil	CO <sub>2</sub>	6000	7
NKK	CO <sub>2</sub>	3000	4

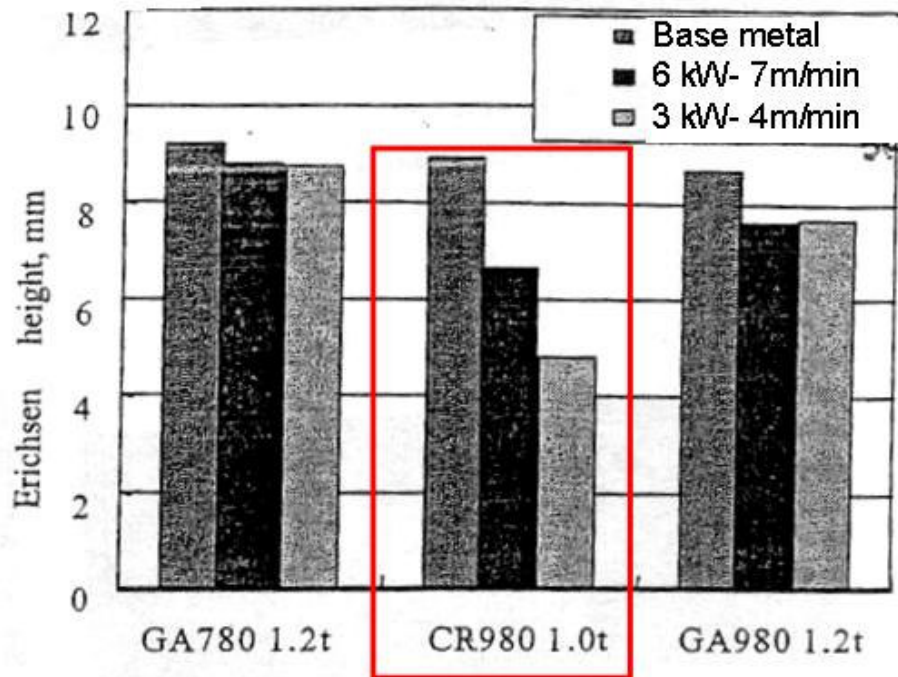


Figure 2-8 Formability Vs Different Laser welding parameters [4]

Azuma et al. [49] used a 50mm diameter dome punch for their experiments, considering two different weld orientations. The first orientation placed the weld line perpendicular to the major strain direction (also called the transverse direction), and the second placed the weld line parallel to the major strain direction (longitudinal). The results for the transverse and longitudinal loading directions are shown in Figure 2-9. The loss of maximum height of a welded specimen loaded in the transverse direction with a thickness ratio of 1.0 was approximately 8%, as compared to an unwelded base material. In the longitudinal direction the loss of height was much greater, at approximately 30%. For low gauge ratios the major strain direction is very critical for determining dome height, with the transverse direction performing excellently. As the thickness ratio increases this advantage is lost. The maximum height appears to decay exponentially for the transverse specimens, before reaching a steady trough after a ratio of 1.5. For the longitudinal specimen, the maximum height drops a relatively small amount for ratios from 1.0 to 1.8, indicating that loading in the longitudinal direction is not as sensitive to thickness ratio as the transverse direction. Interestingly, after a ratio of approximately 1.5, the difference between the two loading directions is relatively small at approximately 10%.

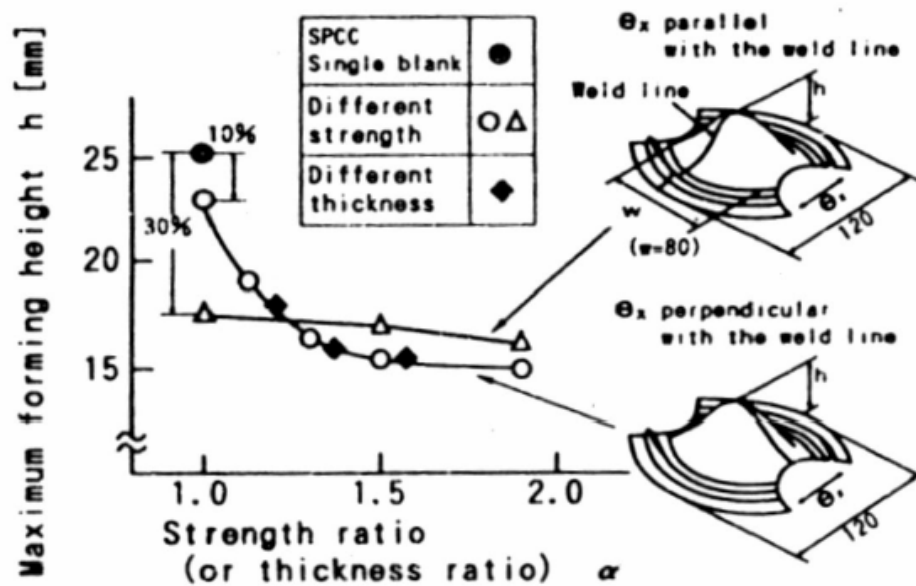


Figure 2-9 Steel TWB LDH test result [49]

Radlmayr et al.[50], having also investigated welding processes, fatigue strength, corrosion, and characterizing many different aspects of steel TWBs, performed a limited set of Nakazima tests. Nakazima (Dome) out-of-plane test uses a hemispherical punch similar to LDH. Since for this test deformations are not frictionless, lubricants are used. The necessary strain paths are obtained by using different lubricants, creating different friction conditions, and also with different sample widths. Results of the dome height tests are only presented in the longitudinal orientation. Because of clamping considerations, three different strengths of unspecified steel materials that composed the TWBs were all of the same thickness at 0.9mm. These three materials were welded in six configurations. The first three TWB configurations were blanks welded from two sheets of like materials and were compared to results from a base material blank. In each case, the loss of dome height was relatively small. The maximum loss was smaller than 20%, the other two cases showed approximately a 10% loss, without a clear trend based on strength. This result is better than the loss in dome height in Azuma's work. For each TWB combination of differing strength materials, the dome height at failure lay between the two like-material TWB test results.

### **2.9.3 Machine**

Saunders et al. [51] investigated the formability differences between CO<sub>2</sub> and Nd:YAG laser welding, and mash seam welding. Formability was evaluated using a scaled down automotive part, as well as tensile, LDH, and OSU formability tests. A new test called OSU formability test was developed in which an elliptical punch was used to evaluate several coated and uncoated sheet materials. The results showed that the reproducibility was better compared to LDH test. Good correlation was found between the OSU and LDH tests. The OSU test was found to be suitable for only materials with low r-values as there was excessive lateral strain for materials with high r-values (>1.5). Also, the elliptical geometry of the punch is difficult to fabricate compared to a hemispherical punch.

The laser welded TWBs in their investigation had narrower welds than the mash seam welds, although there was undercut present in the specimens. The mash seam welds were as wide as the overlap used in the process. They abandoned LDH testing after having difficulties with material draw-in. Based on their metallography and tensile test results they have concluded that the performance of CO<sub>2</sub> and Nd:YAG laser welds can be made virtually indistinguishable.

### **2.9.4 Material**

Waddell et al. [52] concluded that the fracture height of an Erichsen cup test was inversely proportional to the hardness of the weld material or the carbon equivalent. The carbon equivalent is a measure of the hardenability of a steel material. Higher carbon content equates to a higher potential hardness, due to increased iron carbide (Fe<sub>3</sub>C) [52] second phase in the iron matrix, as well as increasing the window of cooling time required to produce a martensitic micro structure as the molten weld HAZ material solidifies and cools.

Numerous studies have confirmed that in formability experiments of TWB, strain is concentrated and fracture occurs in the thinner/weaker side of the blank this is called limiting strength ratio (LSR) [51,52,53,54]. LSR is given as given below:

$$\text{LSR} = \frac{\text{Yield strength (} \sigma_s \text{) of higher strength material}}{\text{Ultimate tensile strength (} \sigma_{ts} \text{) of lower strength material}}$$

In order to have a better uniform stretching of the TWB the LSR should be less than unity. On the other hand, it is known that laser welds in AHSS are harder/stronger than the base metal [55], and the surrounding HAZ contain regions that may be harder or softer [56]. Therefore, some significant effects of welding on formability would be expected.

Previously, research was conducted on the relative influence of the sheet rolling direction, welding route with respect to rolling direction and weld orientation on formability punch of laser welded steel sheet [37]. The conclusion were that for similar thickness laser welded samples, the measured strain values were relatively insensitive to the position of the weld with respect to the crown of the punch, while dissimilar laser samples showed some variation.

Welding orientation relative to the rolling direction (parallel, perpendicular and diagonal) did not influence the formability. However, the formability was influenced for different thickness blank [37, 57]. Dome height tests have also been used by a number of other steel TWB researchers including Shi et al. [58], Radlmayr et al.[50], Saunders et al.[51], Baysore et al.[59], Waddell et al.[52 ] , Aristotle et al.[56], and Chan et al. [60] but with comparatively few TWB configurations.

An introductory study on the influence of welding phenomena on the formability of HSLA and DP980 steels has been done [10]. This study was on the effect of the diode laser weld on two different materials and also the influence of soft zone in the outer of HAZ of the welds of DP980 steel on the formability.

## **2.10 Application of Numerical Methods for TWBs**

Computer based mathematical modeling of forming processes is now capable of giving outstanding improvements in economy of manufacture and product quality if it can be applied using sufficiently accurate representation of material behavior and of boundary conditions in the process. Finite element analysis has been carried out to investigate the significance of the softened zone in the weldment and its effect on the global deformation behaviour [70].

Experimental and numerical simulation for aluminium alloy (AA 6082) weldments in the transverse tensile testing were conducted to look into the influencing factors on the tensile behaviour using Abaqus code [70]. The result concluded specimen geometry (plate width, thickness) and width of the soft zone generated in the HAZ are the influencing factors on the tensile behaviour.

Rodrigues et al [71] investigated the influence of mismatch between different material mechanical properties within the weldment. Constraint on the plastic deformation behaviour of the HAZ in welds on high strength steels using numerical methods. Uniaxial tensile test of welded samples with different hypothetical HAZ widths were simulated for various material mismatch levels (low to high). Their conclusions are that the overall strength of the joint is related to the tensile strength of the soft zone and the mechanical behaviour of the overall joint depends on the plastic strain distribution inside of the HAZ. The butt joint tensile performance of arc welded AHSS was simulated using finite element analysis (FEA) and design of experiment (DOE) was done to find out the most influential parameters. Two different failure modes were observed: of failure due to localized stress concentration; and failure due to excessive elongation of the welded AHSS steels [72]. It was concluded that the influencing factors in the tensile performance are HAZ strength and weld metal strength; increasing these two parameters decreases tensile strength and displacement at peak load relative to the base metal strength. However, these literatures only had the numerical simulation studies, without comparison with the experimental results and evaluated the weldments with addition of the filler material during the welding process. An autogenous laser welding process was not used for numerical simulation. In view of the above shortcoming, this work is intended to present a numerical simulation of the tensile test of the autogenous laser welded steels.

## **2.11 Summary**

The use of tailored blanks has increased steadily over the last 20 years, and is expected to continue to rise above current levels [87,88]. TWBs offer several notable benefits like reduced manufacturing costs, minimized waste part, and improved dimensional control, as well as performance improvements and decreased part weight [48]. To further improve crash worthiness and weight reduction goals, automotive manufacturers are evaluating

the use of advanced high strength steels (AHSS) in TWB applications. One type, dual phase (DP) steels are processed by intercritical annealing and rapid cooling to produce a continuous ductile ferrite matrix with islands of hard martensite [26]. This microstructure produces a high work hardening rate, resulting in higher ultimate tensile strength compared to conventional HSLA steels with similar yield strength. Thus, DP steels are suitable for forming operations, and can be considered for TWB applications.

The predominate joining processes for TWB fabrication are laser beam welding and mash seam resistance welding, with laser welding more common in North America [68]. Several power supplies have been used for laser blank welding, including CO<sub>2</sub> [68], Nd:YAG [33, 60], and high power diode laser (HPDL) [38,40].

Formability is one of the most important mechanical characteristics in materials for auto parts. Although a formability comparison has been made between HSLA and DP steels [44], little research has been conducted on the effects of welding on formability of DP steels [38, 57]. Inhomogeneity of microstructures and properties across a weld brought about by the welding process may greatly change the deformation response of a weld and thus the overall welded specimen properties. Numerous studies have so far been reported of the formability of tailor welded blanks [51, 53, 60]. However, the focus of attention has almost invariably been the effects on forming of dissimilar material properties or thickness across the weldment, which has served to obscure the role of welding itself upon the deformation characteristics.

Through the use of finite element method (FEM) stamping simulation, it has been shown that the formability of laser welded blanks can be predicted without the production of test dies [82]. Numerical simulation is an effective tool for clarification and confirmation of experimental observations. Saunders et al [51] used the FEM to show that the formability of TWBs is related to the material thickness and strength ratios, as well as weld ductility. The accuracy of the simulation; however, depends on the availability of accurate material mechanical properties in both the base metal, and the weld region. Methods for evaluating weld metal properties by comparing experimental tensile tests with simulation results have been proposed [36, 57]; however, these methods are only able to predict hardened fusion zone and HAZ properties and do not provide a solution where HAZ softening is observed. Rodrigues et al. [71] used finite element simulations to evaluate

the effects of a soft zone on the strength and ductility of welds in high strength steels in tensile testing. Their work focused on thick sections in three-dimensional stress states, and the results may not be applicable to thin sheets which can be assumed to be two-dimensional. Furthermore, they assumed mechanical properties for the hardened and softened zones which are difficult to determine in practice. Tomokiyo et al. [86] used FEM to clarify the effect of a softened HAZ on the formability of laser welded DP980 blanks. The material properties of the softened region were evaluated by mechanical testing of thermally simulated coupons. Their results showed that strain localization occurred in the softened-HAZ, but they could not compare the analysis with experimental results, and they did not consider the effects of varying soft zone width or strength.

Among the material properties strain hardening coefficient ( $n$ ) affects formability in stretch forming. It is a measure of the ability of the metal to resist localized strains and thus postpone the onset of necking/non-uniform deformation. A sheet with high strain hardening exponent has better ability to uniformly distribute plastic strain (higher % elongation) in uniaxial tensile test. It was also observed that  $n$ -value and % elongation from the tensile test reflects the overall stretchability of the material in sheet forming. So tensile test simulative test is the easiest and quickest way to analyze sheet formability.

This study is on the influence of the laser welding on the formability aspects of the AHSS and to develop a numerical simulation approach for modeling the uniaxial tensile test of laser welded DP980 blanks which show significant softening in the HAZ.

### 3 Equipment, Materials and Procedures

The various experimental techniques and methods used to characterize the properties of base materials and the welded blanks to study formability of the five types of steels for tailor welded blanks are discussed in this chapter as shown in Figure 3-1. The design and process details of specimen preparation, laser welding and experimentation are explained. The different steps followed in the design and fabrication of experimental set up are also discussed in detail.

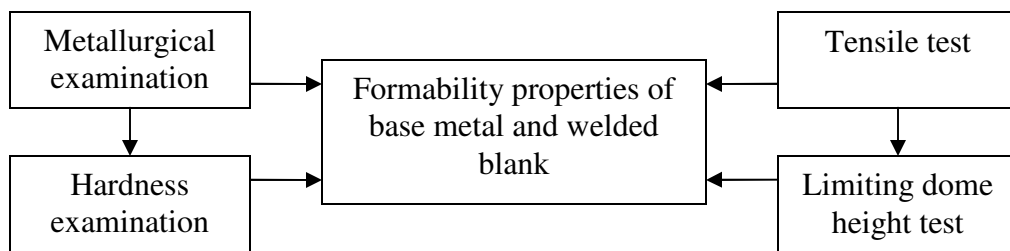


Figure 3-1 Block diagram for the various experimental analyses conducted in this chapter.

#### 3.1 Laser Equipment

A study of the weldability of steels was carried out primarily on butt welds on small flat coupons. Generally, coupon size was 100×25 mm, yielding welded specimens of 100×50mm, though this was increased when necessary to obtain adequate specimen size for mechanical testing. Two different laser systems were used in the course of the work; the system characteristics of each are summarized in Table 2.6.

##### 3.1.1 The Diode Laser

The Nuvonyx ISL-4000L is a 4kW AlGaAs diode laser with a wavelength of  $805 \pm 5$  nm [81]. The diode laser had the laser head mounted and deployed on the arm of a Panasonic VR-016 welding robot. The system as used for laser welding is shown in Figure 3.2. The coupon holding fixture, also visible in the figure, used high strength steel clamping bars tensioned by arrays of cap screws. The diode laser comprises four water cooled heat sinks each containing 20 individual laser diodes, with condensing optics to

deliver a combined rectangular beam of 12 x 0.9 mm. In all cases welding was carried out with the welding direction parallel to the beam long axis, and with the plane of best focus coincident with the coupon top surface.

The laser system consisted of a system control unit, a laser head and a chiller. The system control unit contained current power supplies as well as system control PLC modules and a touch-screen control interface. The laser head contained the laser diode arrays, a focussing lens and output window. The laser diode arrays were cooled by water flowing through channels in heat sinks to which the diode bars were mounted.



Figure 3-2 Nuvonyx ISL-4000L diode laser system and Panasonic VR-16 welding robot. The chilled water was supplied to the laser head by an external chiller unit. Water flow from the chiller was measured and controlled by the system control unit. In addition, dry compressed air was used as a purge gas which flowed through the laser head cavity at all times when the chiller was in operation, in order to control the humidity in the laser cavity and prevent condensation which may damage components. An air knife was fitted to direct a jet of air in front of the output window of the laser head to protect the output window from spatter or fumes. Welds were conducted in the bead on plate mode i.e. a butt weld with full penetration on the blanks of uniform thickness and material. Welding

was conducted on the blanks within the speed range of 0.7 – 1.9 m/min. Welding speed less than 0.7 m/min led to excess weld size and sag; speed above 1.9 m/min resulted in partial penetration.

### 3.1.2 Fixtures and Shielding Gas for Diode Laser

Tight, uniform clamping was achieved by a fixture as illustrated in the system schematic, Figure 3.3. Clamping bars machined from high strength steel allowed the transfer of strong clamping forces through a thin, streamlined geometry. The design of the fixture and the clamping bars allowed for full access of the laser to the weld joint without interfering with the shielding gas flow or air knife. All of the fixtures had an open cavity beneath the weld line, designed to absorb any transmitted laser energy and to facilitate exclusion of air from the underside welding environment by Zn vapour generated during the process.

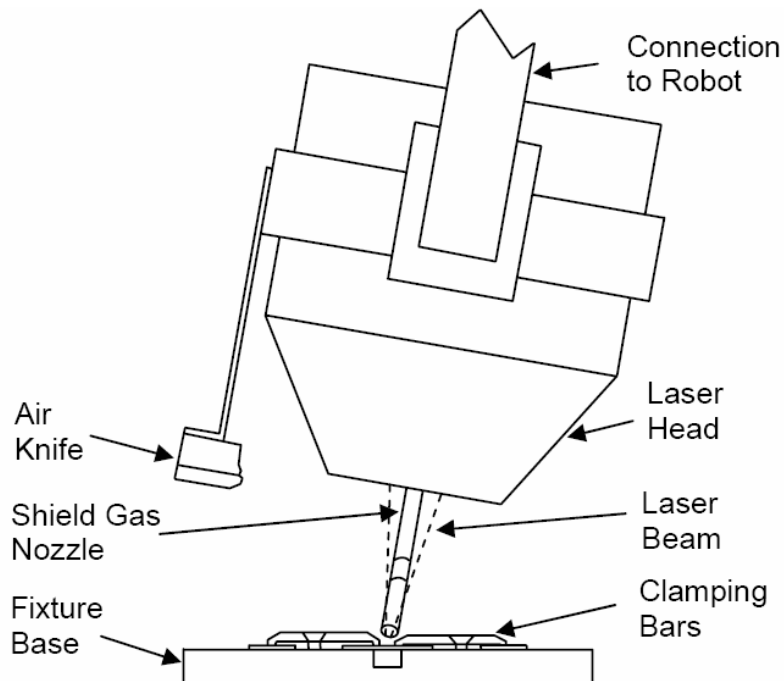


Figure 3-3 Diode laser welding fixture and shielding gas setup.

Shielding was provided by feeding ultra-high purity argon through a specially designed nozzle. The shield gas nozzle was attached to the bracket surrounding the laser head and

angled to provide a laminar flow of gas from the front of the weld pool. The inside diameter of the shield gas nozzle was 19 mm (3/4"), and gas flow rate of 14 l/min (35 cfh) was used to achieve good shielding of the weld pool with laminar flow. The shield gas nozzle was mounted to the laser head bracket to direct shield gas from the front of the weld pool toward the rear of the weld pool. None of the weld tests employed inert gas shielding on the underside of the joint assembly.

### 3.1.3 The Nd:YAG Laser

The Haas HL3006D Nd:YAG laser employed fiber optic beam delivery from a remote laser system to the final delivery optics. The full power of 3 kW was used for the welding process. Operating speeds were used within the range of 1 – 6 m/min to obtain full penetration. Welding speed less than 1m/min led to cutting of the material; speed above 6 m/min led to incomplete penetration.

## 3.2 Selection of Materials

The microstructures of DP and HSLA sheet materials used in this work are shown in Figure 3.4. The DP steel has a ferrite matrix with a significant volume fraction of fine martensite grains. The HSLA steel also has a fined-grained ferrite matrix with very small dispersed colonies of alloy carbides. A summary of Chemical composition of the different steels is provided in Table 3.1. Steels thickness with a coating, described as galvanized coating (GA) was used for this study. The volume fractions of martensite ( $f_M$ ) were determined using quantitative metallography and  $H_{BM}$  is the Vickers hardness of base metal. Since the full chemical composition of the steel was considered proprietary, a summary of the alloying is provided including carbon equivalent using the well known Yurioka formula [16].

$$CE = C + f(C)[Si/24 + Mn/6 + Cu/15 + (Cr + Mo + Nb + V)/5], \quad (1)$$

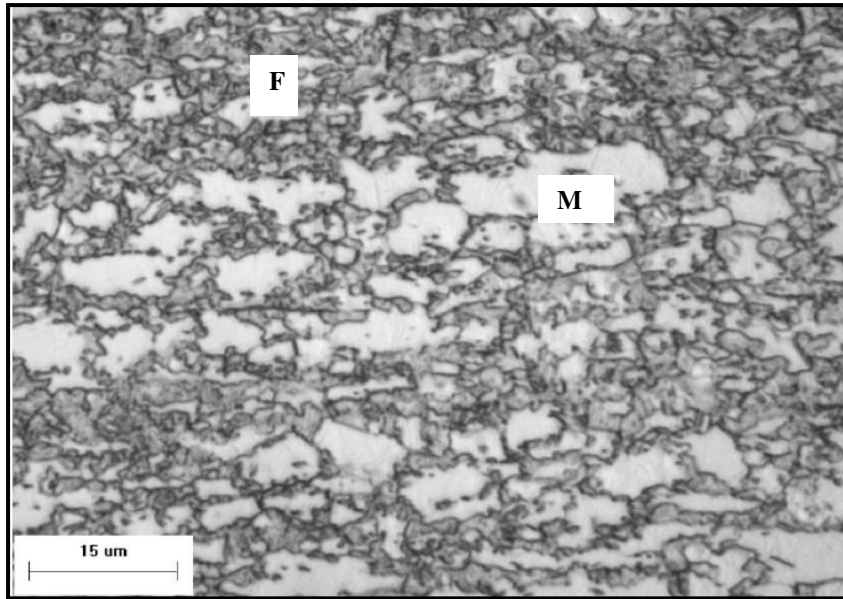
where,  $f(C)=0.75+0.25\tanh[20(C-0.12)]$ .

The melting temperature (in K) of the steels was calculated with the following equation[16]:

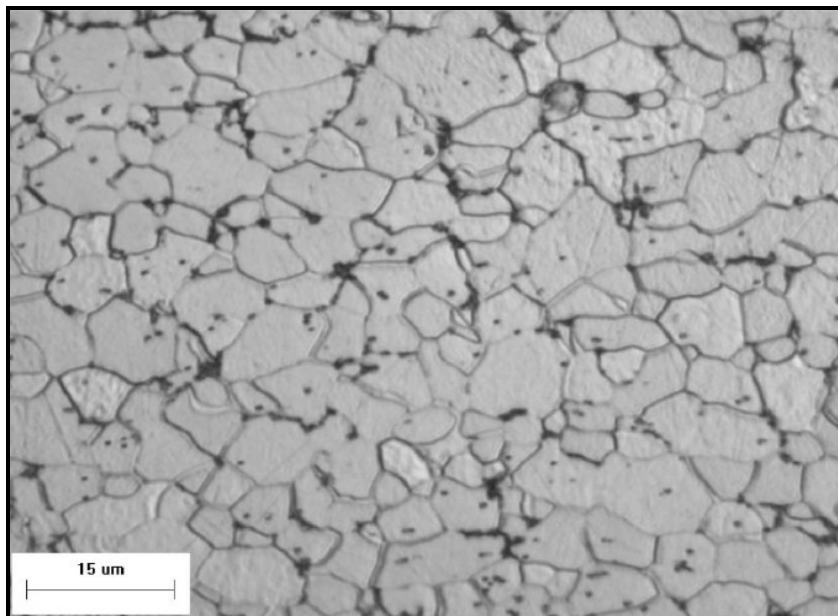
$$T_m = 1810 - 90C \quad . \quad (2)$$

The critical temperature (in K) for austenite transformation on heating was estimated for the steels using the equation proposed by Yurioka [16].

$$T_{Ac1} = 1024 - 26.6C + 17.6Si - 11.6Mn - 22.9Cu - 23Ni + 24Cr + 22.5Mo - 39.7V - 5.7Ti + 232.4Nb - 169.4Al - 894.7B \quad (3)$$



(a) DP Steel



(b) HSLA

Figure 3-4 Microstructure of the base metal (a) DP steel (b) HSLA steel

Table 3-1 Chemical composition of the different steels

Steel	Thickness (mm)	Coating (g/m <sup>2</sup> )	f <sub>M</sub> (%)	C (wt%)	CE (wt%)	HBM (Hv)
HSLA	1.14	N/A	-	0.056	0.170	163
DP450	1.2	77	7	0.071	0.265	162
DP600	1.0	77	16	0.099	0.341	199
DP800	1.25	77	54	0.147	0.524	262
DP980	1.17	48-55	49.4	0.132	0.474	283

### 3.3 Metallurgical Examination

#### 3.3.1 Sample Preparation

Weld characteristics were evaluated using metallographic examination and microhardness measurements. Thin sections were cut from the laser welded specimens, mounted and polished as per standard metallographic procedures to observe the microstructure of the weld fusion zone, HAZ and parent sheet. The polished specimens were etched with 2% nital solution and observed under an optical microscope.

#### 3.3.2 Optical Microscopy and SEM Analysis

Stereo-microscope images and optical micrographs were acquired and analyzed using image-analysis software. Scans of entire weld cross-sectional areas with the optical microscope were made using an automatic stage, and images were assembled by the image analysis software. The weld profile was observed at 50X magnification to check the penetration and grain size and structure were observed at a higher magnification. SEM was performed on a Jeol JSM 6460 with an attached Oxford Instruments INCA-350 for energy dispersive spectroscopy (EDS) analysis.

### 3.4 Hardness Examination

Cross-weld Vickers microhardness tests was conducted on the etched specimens at a load of 500g, with loading time of 15s. Traverses normally used a step distance between indentations of 0.3 mm for diode and 0.15 mm for Nd:YAG laser welds as shown in Figure 3.5.

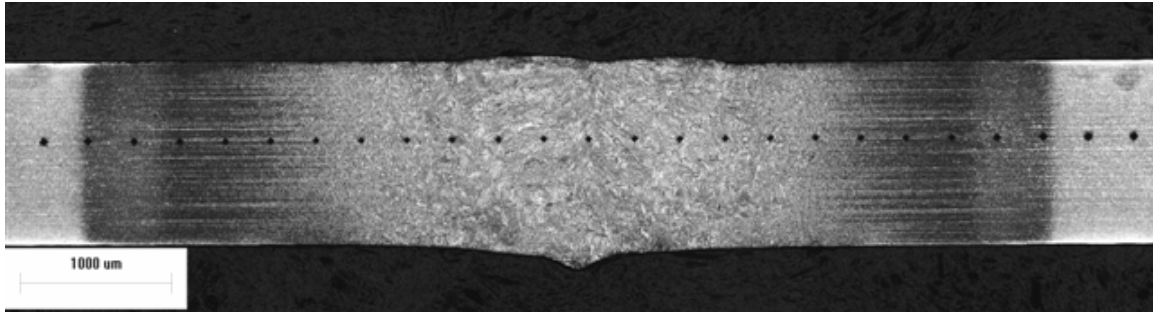


Figure 3-5 Cross weld Vicker microhardness measurement for DP980 steel.

### 3.5 Tensile Testing

Uniaxial tensile tests were carried out on specimens of base metal sheets machined as per ASTM standard E8M specification as shown in Figure 3.6 [62]. The specimens were tested along two directions, with tensile axis being parallel ( $0^{\circ}$ ), 45 degree and perpendicular ( $90^{\circ}$ ) to the rolling direction of the sheet as shown in Figure 3.7.

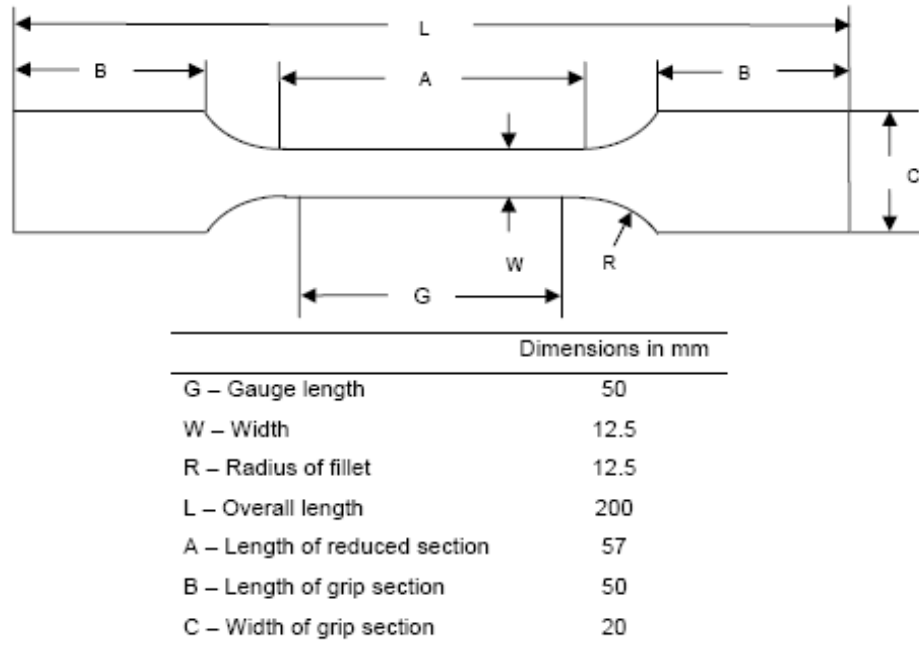


Figure 3-6 Standard tensile test sample

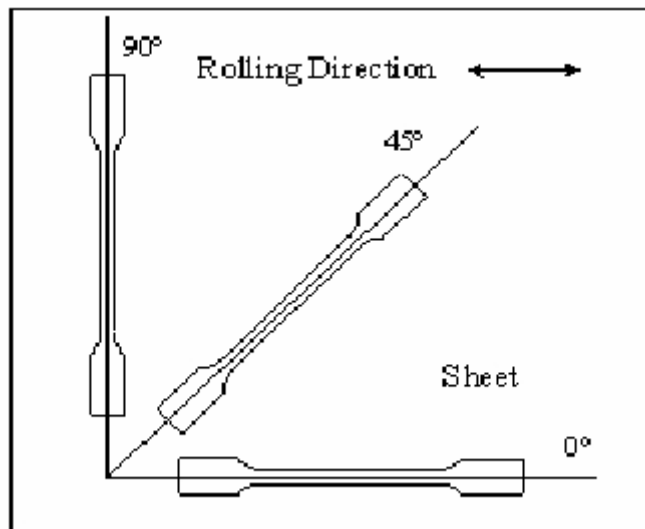


Figure 3-7 Orientation of the tensile test specimens - rolling directions

A constant cross head speed of 2 mm/min was employed in all the cases. The standard tensile properties of 0.2% offset yield strength (*YS*), ultimate tensile strength (*UTS*), % elongation, strain hardening coefficient (*n*) and strength coefficient (*K*) were determined. The strain-hardening behaviour of the sheets can be described by using the Hollomon equation [75]:

$$\sigma = K \epsilon^n \quad (3.1)$$

where  $\sigma$  = true stress,  $\epsilon$  = true strain,  $n$  = strain hardening coefficient,  $K$  = strength coefficient.

For determining the  $n$  value of these sheets, load-elongation data obtained from the above tensile tests were used to plot engineering stress-strains curves. These engineering stress-strain curves were converted into true stress-true strain curves using the following equations:

$$\sigma = s (1 + e) \quad (3.2)$$

$$\epsilon = \ln (1 + e) \quad (3.3)$$

where  $s$  = engineering stress,  $e$  = engineering strain.

The  $\log \sigma$ -  $\log \epsilon$  data were calculated for the uniform plastic deformation range (between YS and UTS) and using linear regression (least square method) a best-fit line was plotted. The slope of this line gives  $n$  value and the y-intercept gives  $\log K$ .

Sub size tensile specimens were cut from the laser welded samples as shown in Figure 3.8 for conducting the tensile tests in transverse and longitudinal directions on the TWBs as per ASTM E8M standard [62]. The tensile tests were done at a constant cross head speed of 2 mm/min until fracture. Since in the longitudinal sub size specimens, the width in the gauge portion is 6 mm out of which nearly 50% is in the weld and the HAZ regions, these tests were done to get an indication about mechanical properties of the weld. Transverse tests were used to ensure that the weld does not crack before the failure occurs in the weaker material due to deformation.

Smaller micro-tensile specimen, as shown in Figure 3.9, was used to obtain the mechanical properties of fusion zone experimentally. The geometry was derived as per the tensile split Hopkinson bar (TSHB) test [61].

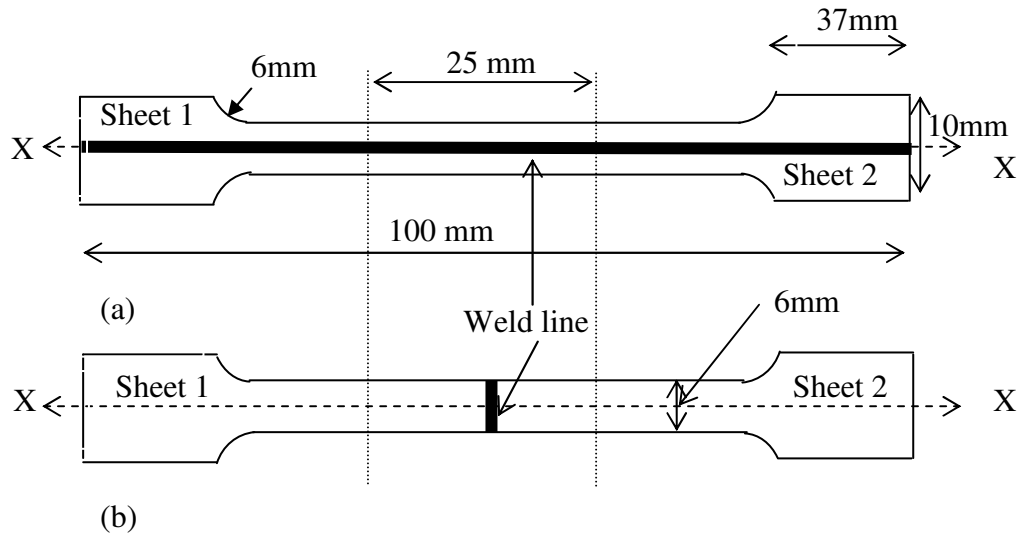


Figure 3-8 Sub size specimens used in uniaxial tensile tests of TWBs (a) longitudinally welded specimen and (b) transverse specimen (weld line perpendicular to the direction of application of load).

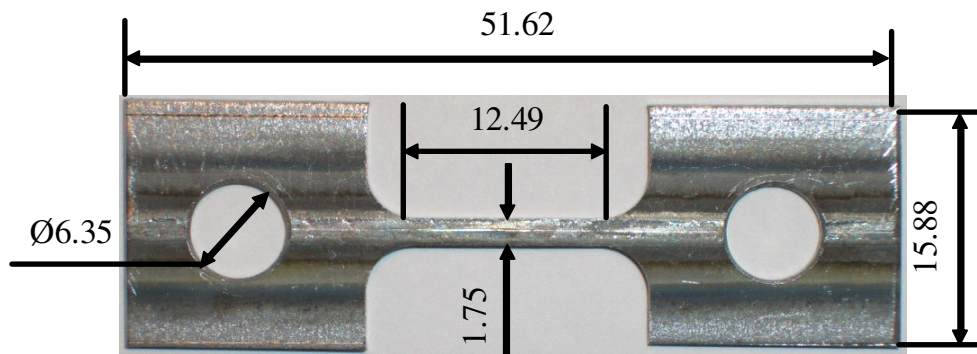


Figure 3-9 Micro tensile sample of the fusion zone

### 3.6 Formability testing

#### 3.6.1 Specimen Preparation and Grid Strain Analysis System

To encourage essentially biaxial, pure stretching deformation, all formability test coupons were square specimens of size 180mm X 180mm (as shown in Figure 3.10), were cut from the laser welded specimens, without cutouts.

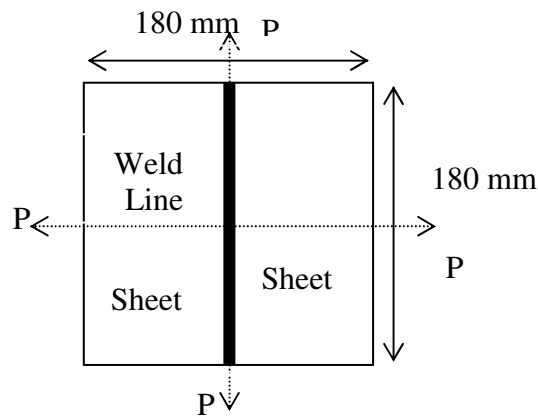


Figure 3-10 Dimensions of welded blank specimens for biaxial stretching

Due to the heterogeneous nature of the mechanical properties across a weldment, variations in strain were expected along weld sample. Local strain in the welded sample after deformation was measured using the circular grid method. Therefore, transverse tensile and formability tests were evaluated using strain measurements to obtain local strains. The strain measurement system consists of two parts: (i) the application of uniform grids on specimens prior to deformation; and (ii) the visual detection system to measure grid sizes at the completion of testing.

### 3.6.2 Gridding

Uniform circular grids were etched onto the tensile and formability specimen. This involves passing an alternating current through an etching electrolytic solution onto the AHSS sheet. This procedure produces a dark etched region on the surface of the sheet. Figure 3.11 shows the etching equipment. By placing an insulating stencil, (E) on the specimen surface (C), a pattern can be produced. The stencil has porous regions where the current can pass through to the surface.

The sheet is cleaned prior to gridding to ensure good electrical conduction with a cleaning solution. The sheet surface is wet with the electrolytic solution and the stencil is applied directly to the sheet surface. An absorbent pad (D) which has been soaked in etching solution is placed on top of the stencil. The electrical circuit consists of a power supply (A) and its two electrodes. The ground electrode (F) is attached to the edge of the TWB specimen. The circuit is completed by a conductive roller (B), which is rolled over

the absorbent pad until a satisfactory pattern of grids is produced. During etching an AC potential of 15V was applied, which does a much better job of penetrating the surface than DC current.

The steel grids exhibit higher contrast and uniformity and are much easier to produce consistently. A more consistent grid size and shape definition facilitates strain measurement especially after a grid has been scored or rubbed by the tooling surface during the deformation process. A circular grid size of 2.5 mm diameter was used for each test.

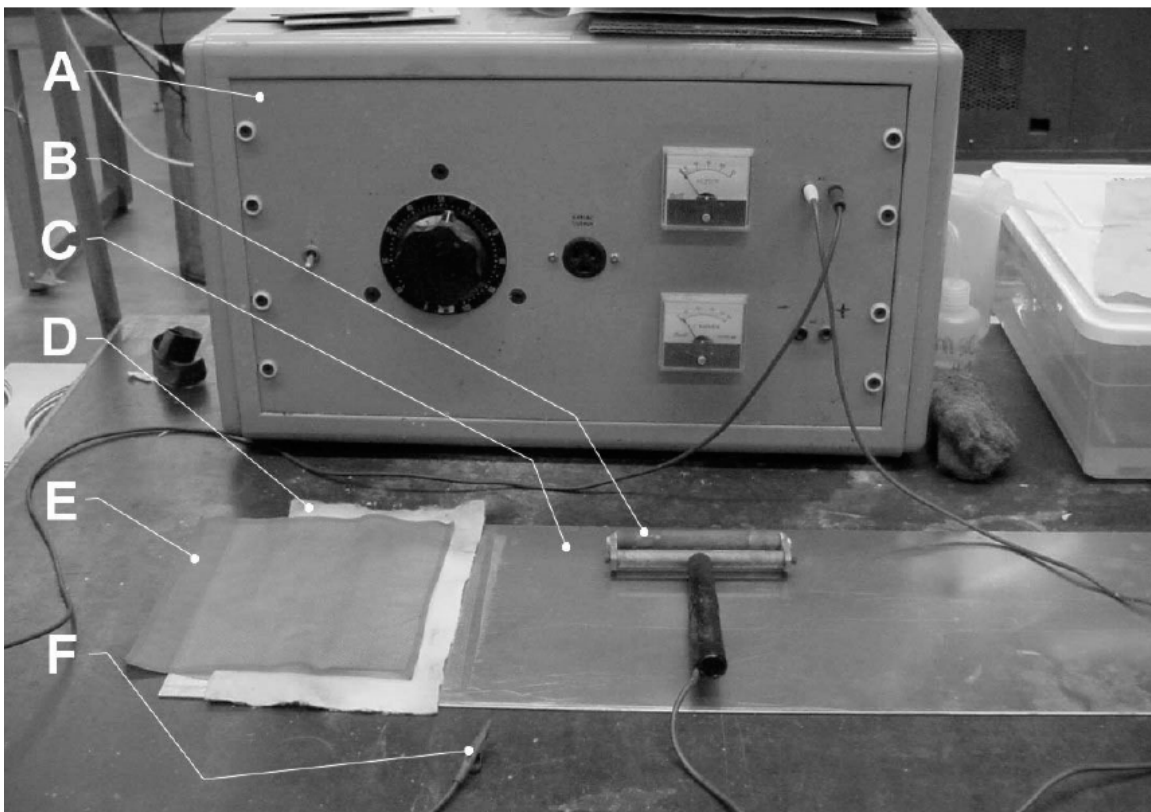


Figure 3-11 Grid etching system

(A) Power supply (B) Conductive roller (C) Specimen (D) Absorbent pad (E) Insulating stencil (F) Ground electrode

### 3.6.3 Limiting Dome Height Test Equipment

The limiting dome height tests were carried out on an MTS 866.02 double action hydraulic press (Fig 3.12). The assembly of punch, lower die and upper die in the experimental set up is shown in Fig3.13. The blank was placed at the center of the lower

die so that weld bead was at the centre of a 101.6 mm (4.0 in) hemispherical punch (Figure 3.13), in a direction perpendicular to the rolling directions. The upper and lower dies had a circular draw bead at a distance of 132 mm (5 in) from the die center. A clamping force of 135 kN was used to secure the blank so that there will be no draw-in in the flange region. The lubrication between the punch face and the TWB surface was provided by a light coating of mill oil (Quaker Lerrocote 61 MAL-HCL-1G), followed by a 0.05 mm plastic sheet. The tests were performed according to ASTM E643-84 standards [62]. While performing the experiment, a practical difficulty of controlling and stopping the test at the point of necking was encountered. Thus both necking and fracture were accepted as the criterion for failure for all the stretch dome tests, which has also been reported by Chan et al. [60].



Figure 3-12 MTS 866.02 formability press.

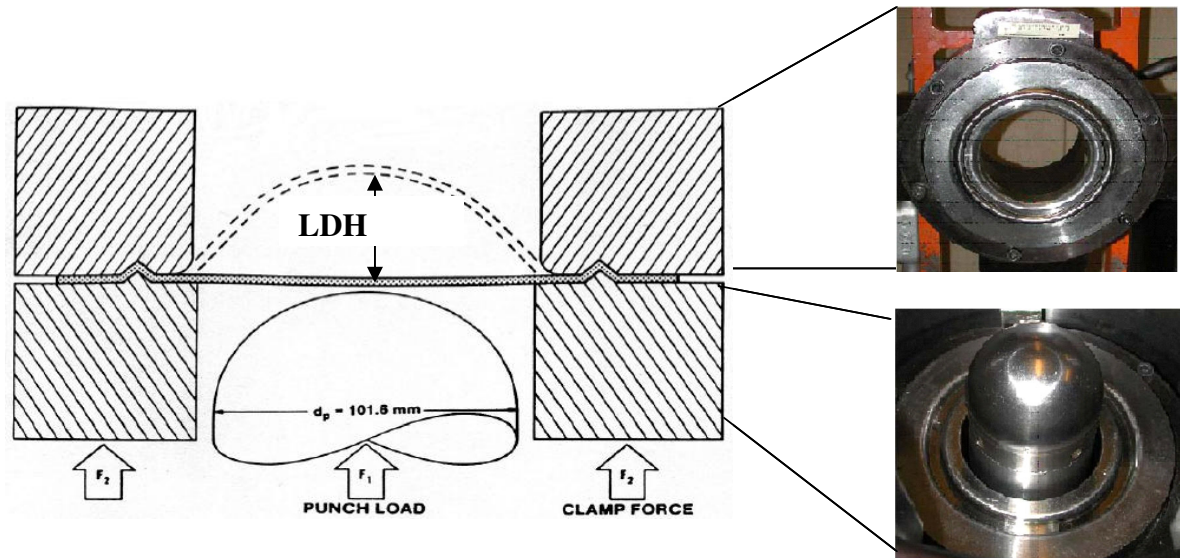


Figure 3-13 Die Geometry

### 3.6.4 Data Acquisition and Strain Measurement

In all the forming experiments, a data acquisition system consisting of a load cell and a rotary encoder was used to record the load-displacement data during the experiments. A 30 ton load cell with a resolution of 10 kg was attached to the punch to measure load and a rotary encoder with a resolution of 0.1mm was attached to the ram to get punch displacement. Amplifier was used to amplify the signals from the load cell and the rotary encoder. These amplified signals are converted to digital signals by analog to digital converter card and are fed to the motherboard. Suitable software was used to collect all the digital data and plot the data in the form of load vs displacement curve.

The grid pattern was applied along the length of the weld, on the welded blanks. Ideally the grid pattern would be etched directly on the weld line itself. However, the irregular weld surface and the variable weld width make it impossible to do so and, as well, the accurate measurement of strain requires a consistent surface to measure from. The transverse mode of failure is usually a HAZ or base material failure, therefore this strain measurement location permits the failure strain to be directly measured. Weld failure in the longitudinal direction is most closely measured directly adjacent to the weld line. The measurable strain gradient is inversely proportional to the grid size and spacing, since

each grid only measures the average strain over the area it occupies. Smaller grid sizes are able to capture a higher gradient of strain in the material since a higher density of grids can be applied. There is a practical limit to the smallest grid size however. As the grids get smaller, their shape and size become more inconsistent. This is especially true on aluminum surfaces, where etching can be problematic. Also the smaller grid sizes would result in more strain measurements for a given area. Strain measurement is a laborious and time consuming procedure, making unnecessary measurement a poor use of resources.

All strain measurements were taken with a digital image analysis strain measurement system, shown in Figure 3.14. Its components include a digital camera (C) with which grid images are acquired, and a computer (A) including a software program (B) which performs the measurements of each grid on a specimen (D). The undeformed grid size must be calibrated before any experiments are performed by taking the average size of many undeformed grids. After calibrating, the error or deviation can be checked. A tolerance of up to approximately 3% strain is expected. After calibration, strain measurement can then be performed. By defining five points on the outer edge of the grid, the elliptical dimensions are computed by the software.

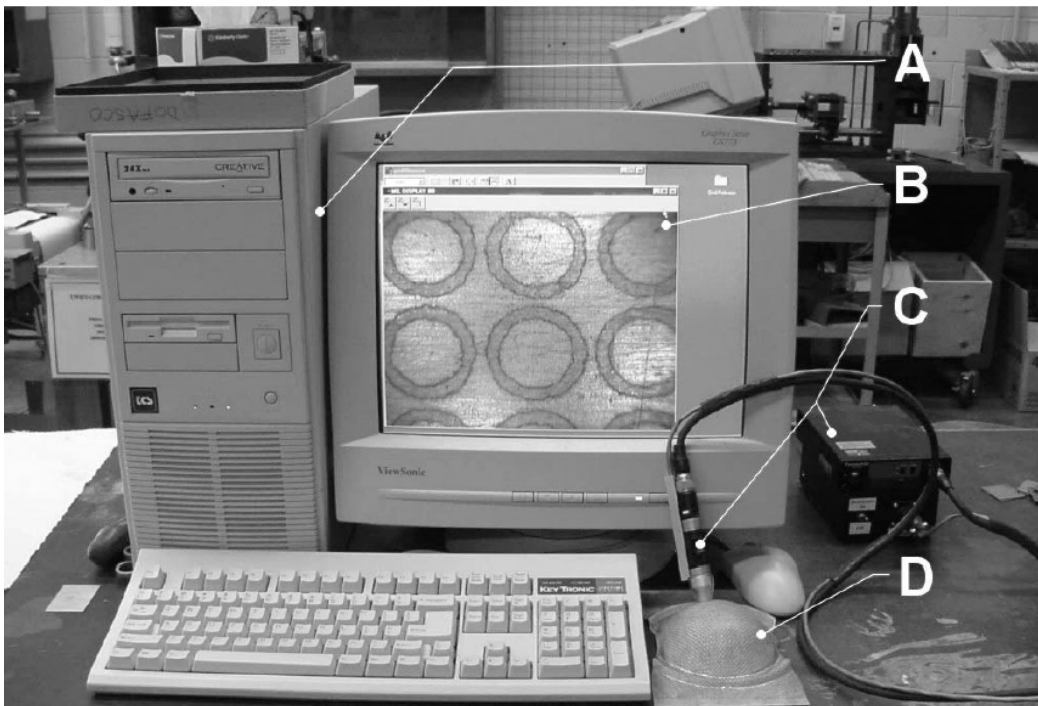


Figure 3-14 Strain measuring system

The major and minor axis of this ellipse is then used to calculate the principal strains. All predicted and measured strain values are calculated as engineering strain. The following equation is used to calculate the principal engineering strains:

$$E_1 = \frac{\text{Ellipse major axis length} - \text{Calibration diameter}}{\text{Calibration diameter}}$$

$$E_2 = \frac{\text{Ellipse minor axis length} - \text{Calibration diameter}}{\text{Calibration diameter}}$$

## 4 Experiment Result

### 4.1 Material Characterization

Material characteristics were evaluated using both metallographic and micro-hardness measurements for both the base metal and the welded blanks.

#### 4.1.1 Metallurgical Analysis

Metallography was performed using optical microscopy and scanning electron microscopy (SEM). The microstructure of three zones (base metal, heat affected zone and fusion zone) are discussed. The cross sectional view of the weldments of both diode and Nd:YAG are shown in Figure 4.1 and 4.2. The base metal microstructure of the DP980 steel is shown in Figure 4-3 a. Microstructural examination shows the tempering of martensite in Figure 4-3 b and 4-3 c for Nd:YAG and diode, respectively. The volume of tempered martensite was less in the Nd:YAG weld due to the keyhole welding mode rather than the conduction mode of the diode laser.

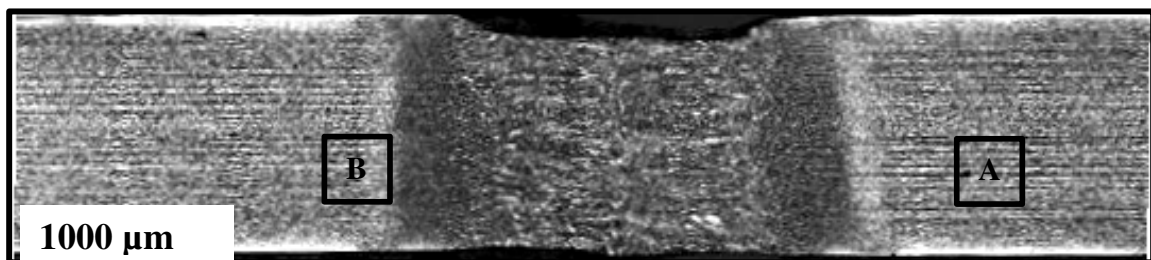


Figure 4-1 Optical photo - Cross section of a Nd:YAG weld at 6 m/min

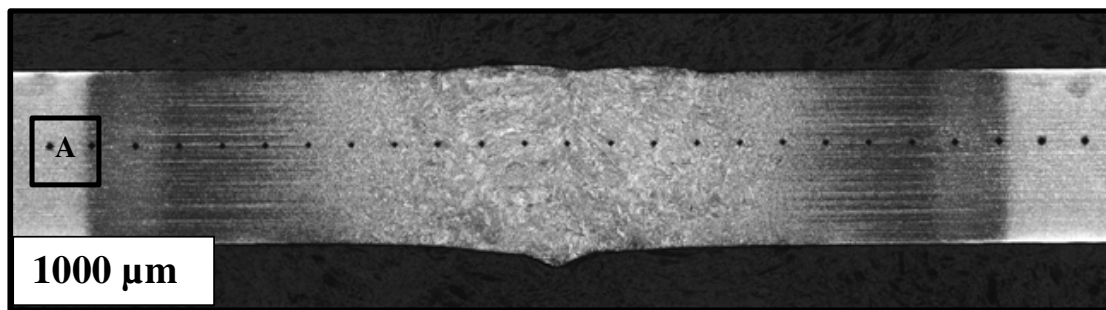
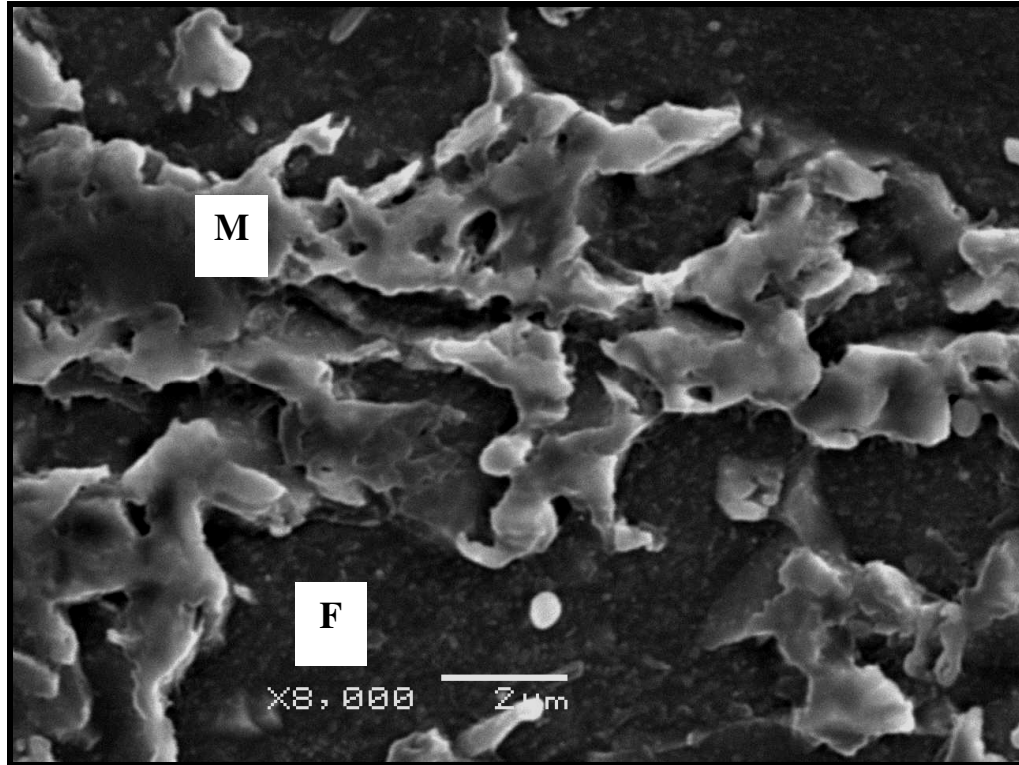
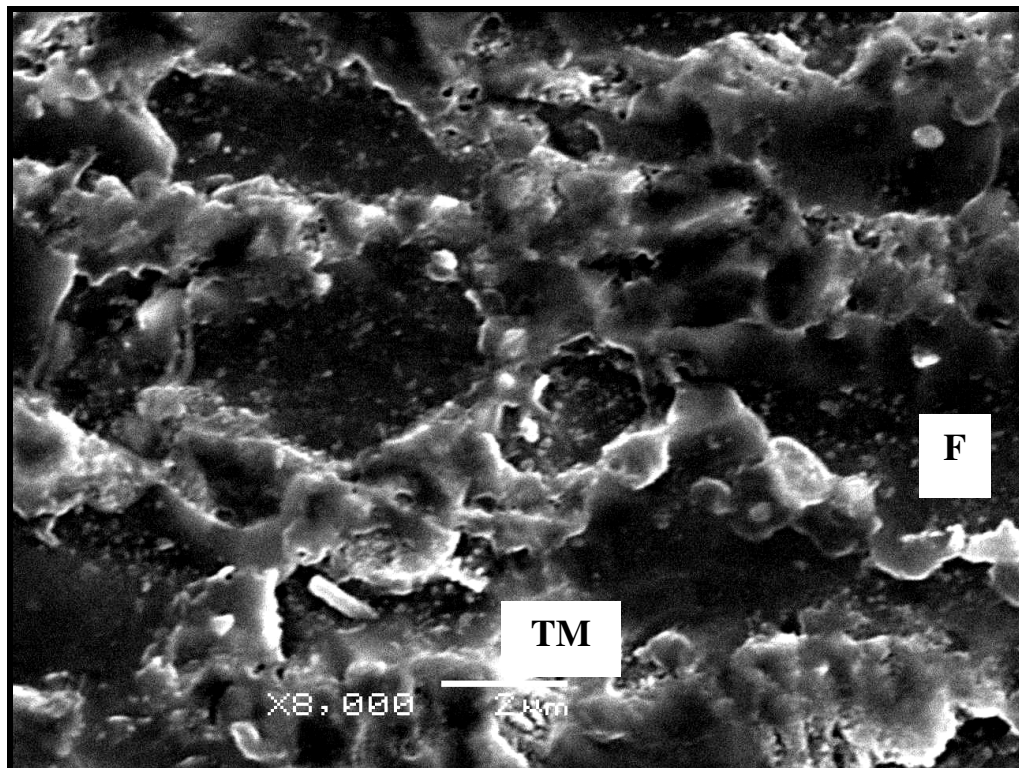


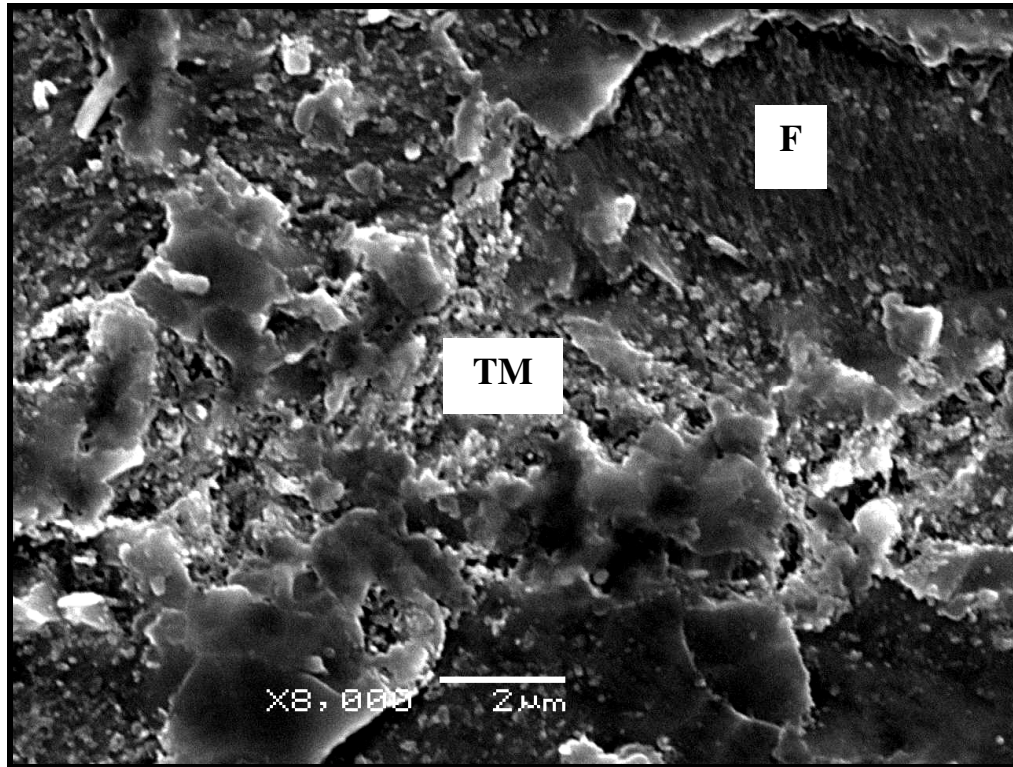
Figure 4-2 Optical photo - Cross section of a diode weld at 0.7m/min



(a) Details of area A in Figure 4.1



(b) Details of area B in Figure 4.1



(c) Details of area A in Figure 4.2

Figure 4-3 (a) SEM photos of base metal and (b) tempered zone in Nd:YAG laser weld  
(c) SEM photo of tempered zone in diode laser weld [M- martensite; F- ferrite; TM-  
tempered martensite] [64]

#### 4.1.2 Fusion Zone Microstructure of Different Steels

Fusion zone microstructure of DP450 under diode laser welding is ferritic and bainitic due to its lean chemistry as shown in Figure 4-4. However, DP600 and DP800 is martensitic in the fusion zone as shown in Figure 4-5 and 4-6. Under the diode laser welding window for these two steels, the fusion zone cooling rate lies within the same range. The individual chemistry represented by carbon equivalent makes a big difference in fusion zone microstructure.

The microstructure of the DP980 steel fusion zone was thought to be mainly comprised of martensite as shown in Figure.4.7, and moreover the hardness was close to levels generally associated with a fully martensite product [63]. The HSLA steel weld metal mostly consisted of ferrite side plate and bainite structures, as shown in Figure.4.8

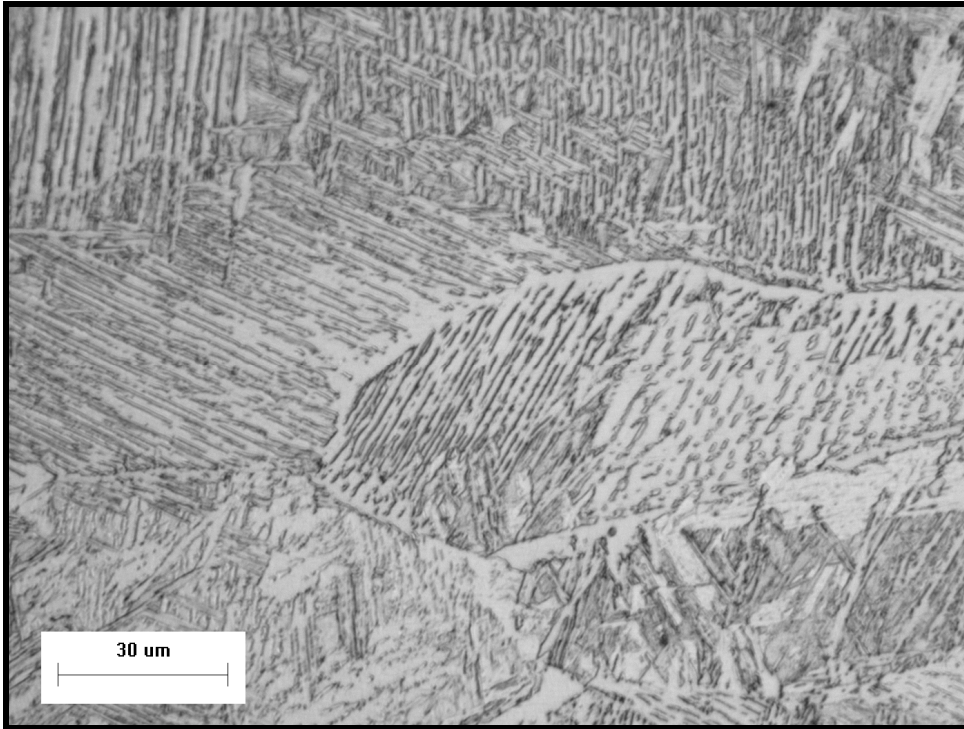


Figure 4-4 The fusion zone microstructure of DP450 diode weld for 0.8m/min

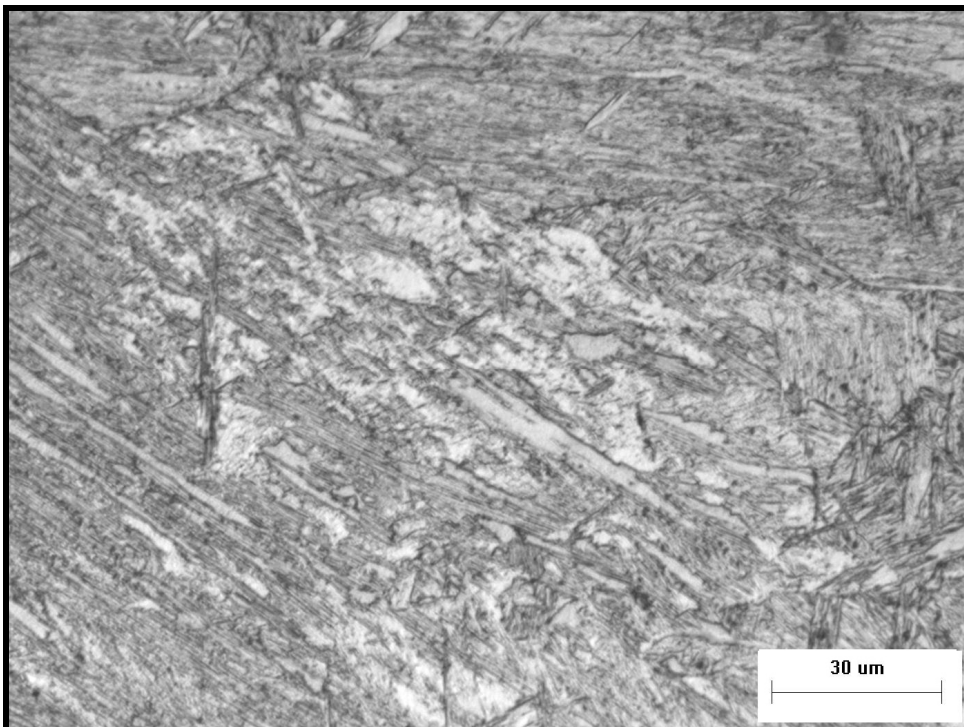


Figure 4-5 The fusion zone microstructure of DP600 diode weld for 1.2m/min

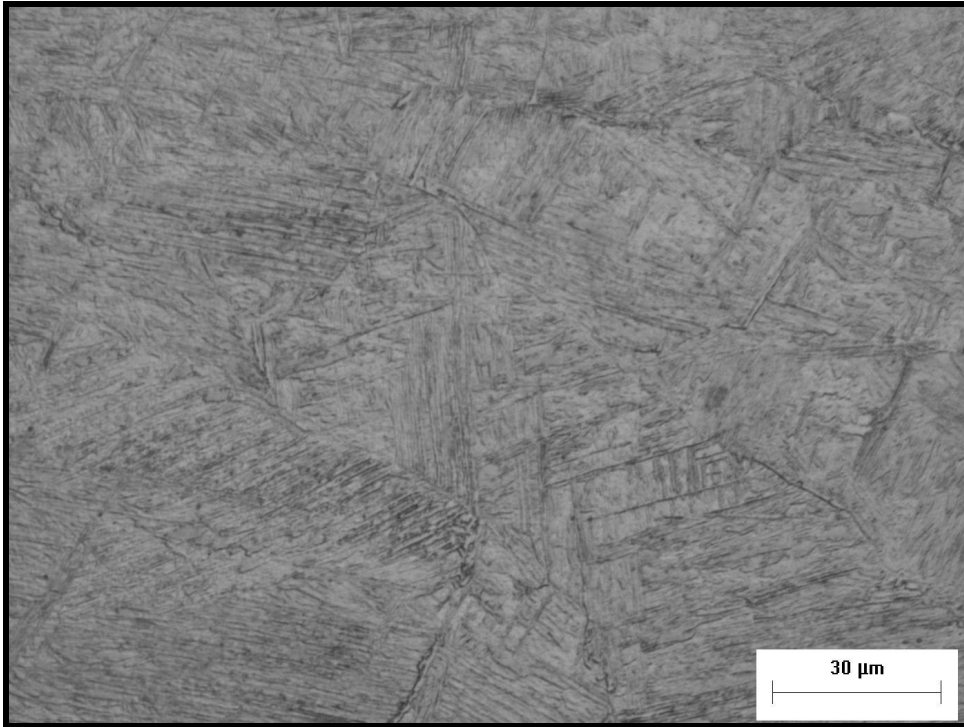


Figure 4-6 The fusion zone microstructure of DP800 diode weld for 0.8m/min

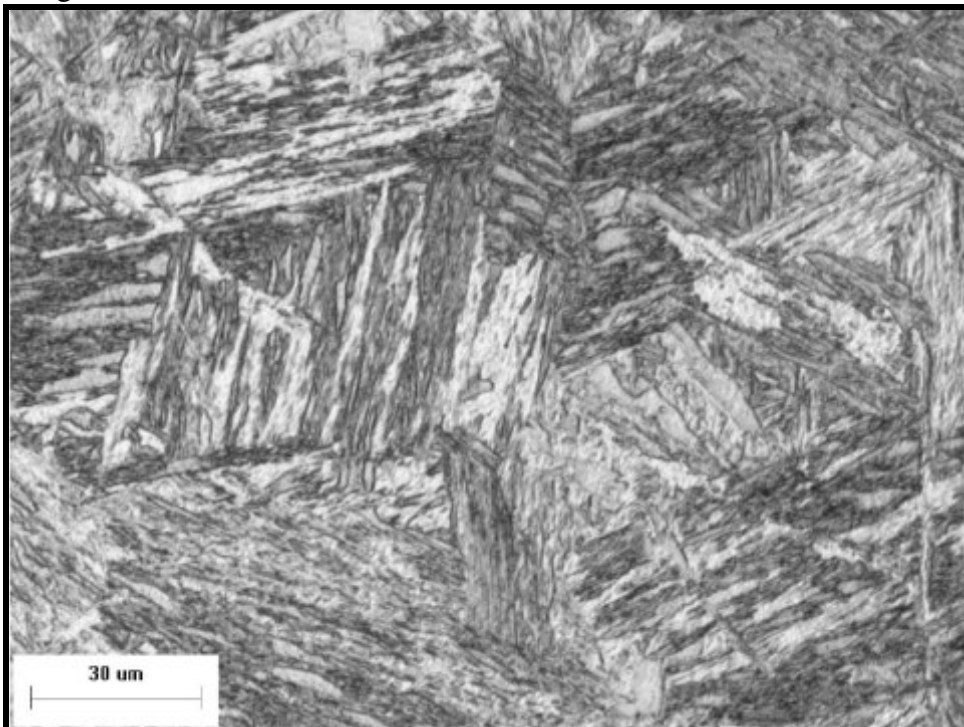


Figure 4-7 The fusion zone microstructure of DP980 weld [10]

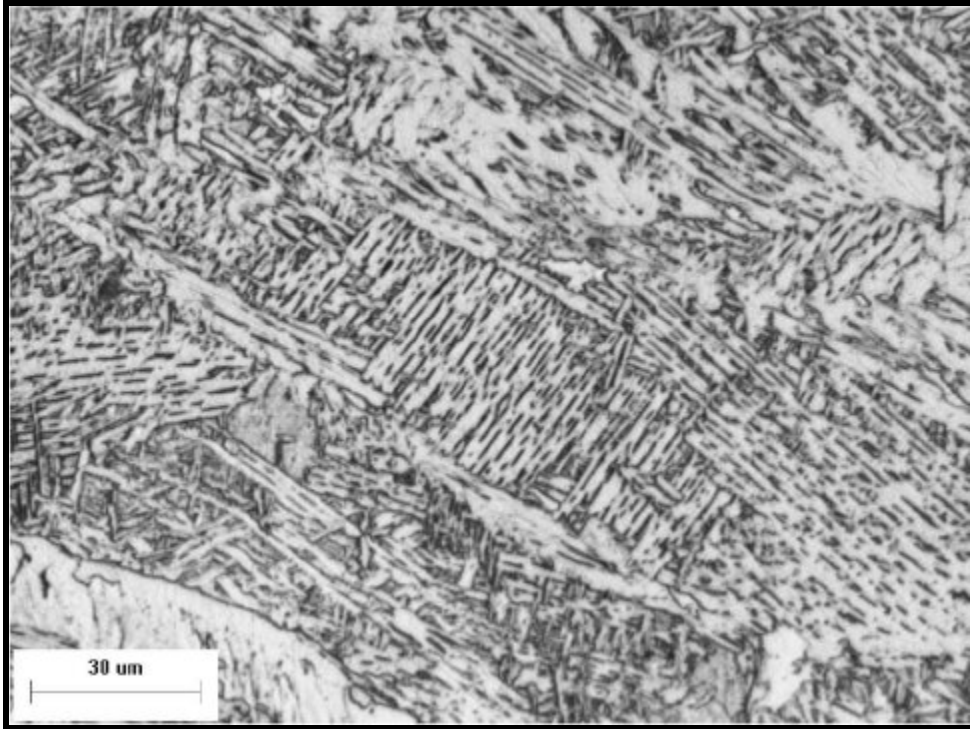


Figure 4-8 The fusion zone microstructure of HSLA weld [10]

#### 4.1.3 Microhardness Analysis

Microhardness profiles across the weld are shown in Figures 4.9 to 4.11. Representative cross-weld hardness profiles across the welds in DP980 and HSLA steels are shown in Figure 4.9. In both steels, the hardness profile was relatively flat across the fusion zone, showing a very high hardness in the weld metal and high-temperature (inner) HAZ, as could be expected from the chemistry. This region was fully austenized during the laser welding process. The high cooling rate generated in the laser welding process, in combination with high carbon equivalent for DP980 steel evaluated with Yurioka formula resulted in the fully martensitic microstructure in the inner heat affected and fusion zone[63].

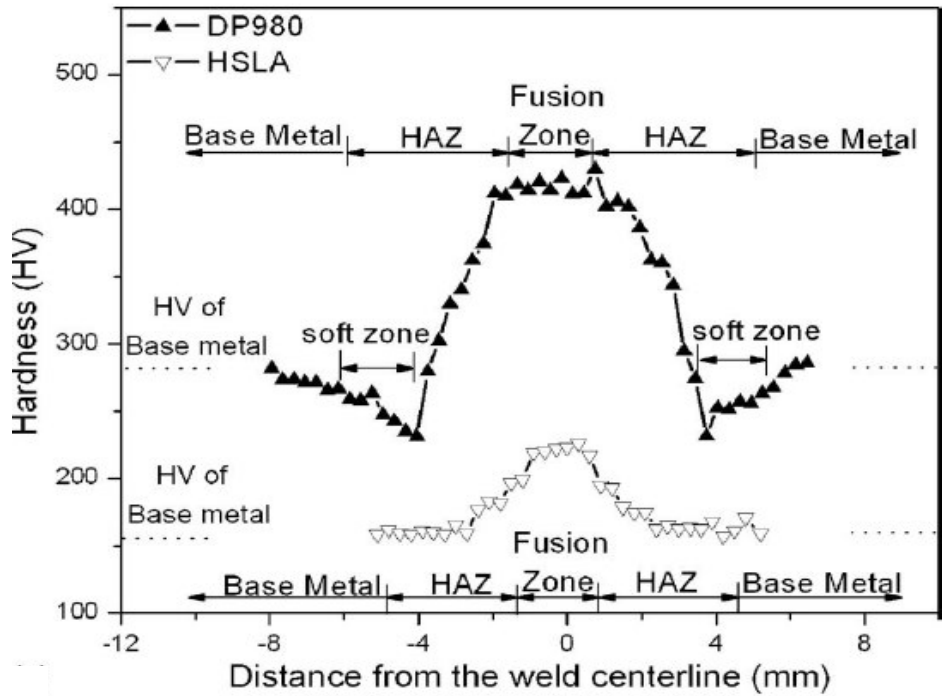


Figure 4-9 Hardness profiles of DP980 and HSLA steel for diode laser at welding speed of 1.0 m/min [10]

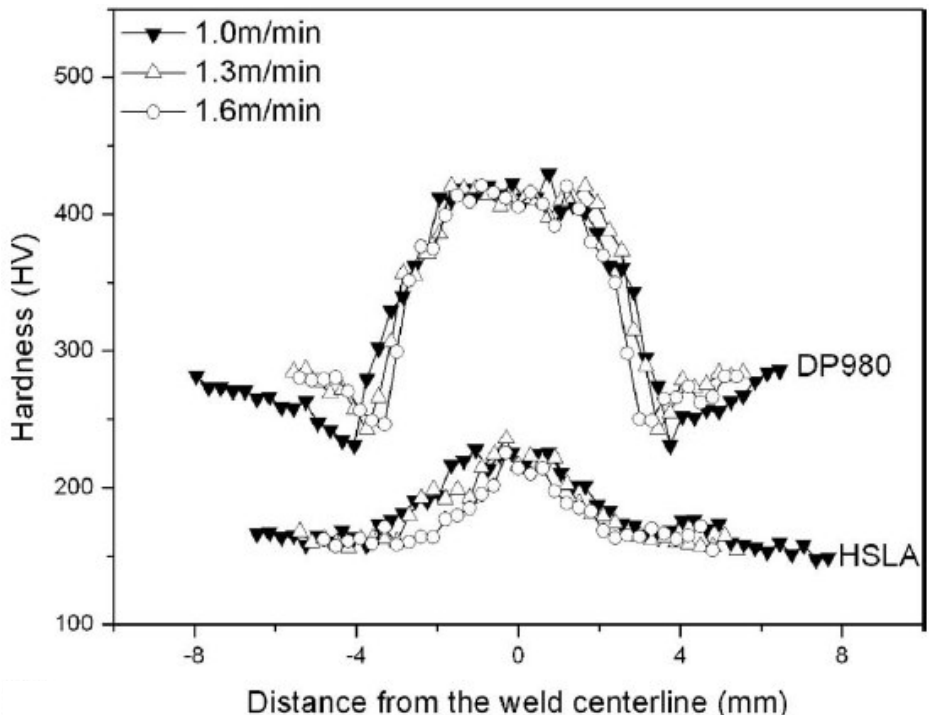


Figure 4-10 Hardness profiles of DP980 and HSLA steels for diode laser at different welding speed [10]

In both steels, the local hardness progressively decreased moving outwards through the HAZ; i.e., with lower peak temperature experienced in the weld thermal cycle. With

HSLA steel, the HAZ hardness pattern merged smoothly into the unaffected base metal. For DP980 steel, however, hardness “valleys” were invariably seen in the outer part of the HAZ (outer HAZ) for all welds, where hardness locally dropped significantly below the base metal hardness. For the Nd-YAG weld there is a "smaller" drop in hardness as shown in Figure 4.11. Such valleys have previously been seen in HAZs of other DP steels [66,67,63] and were attributed to local tempering of the martensite phase of the as-manufactured steel. Microstructural examination also confirmed that the hardness valleys were directly related to tempering or local decomposition of martensite could be observed, as depicted in Figure 4.1 and 4.2

Figure 4.11, depicts typical hardness profiles of DP980 steel welded with Nd:YAG laser. The high welding speed achievable with the Nd:YAG laser led to significantly smaller weld and HAZ width, compared to the diode laser (Figure 4.2) . This observation was primarily due to the high power density and also smaller spot size of the Nd:YAG laser, which resulted in a lower heat input keyhole mode weld and generated a shorter thermal cycle which led to a shallower, narrower softened zone in the outer HAZ.

Xia et al. [83] observed softening in a wide range of dual phase steel designs. The degree of softening in the HAZ was found to be a function of the weld heat input, as well as the steel design. Increasing heat input resulted in an increase in the exposure time of the softened region to temperatures where martensite tempering occurs. At low heat inputs, the minimum hardness in the HAZ tended to approach the base metal hardness. With increasing heat input, the local heating and cooling rates in the HAZ are lower, resulting in a longer exposure to high temperatures and a greater softening effect. The base metal microstructure, specifically the volume fraction of martensite was also found to affect the softening response. The higher strength steels with increased martensite levels were more affected by softening.

Figure 4.12 shows cross-weld hardness profile for DP450, DP600, and DP980 steels welded at a constant weld speed of 1.3m/min. Since the heat input is similar, the softening response of these materials is a function of the martensite content, with the volume fraction of martensite increasing with base metal strength. The highest strength DP980 showed the greatest softening, followed by the DP600, and finally, the lowest strength DP450 showed the lowest softening [65].

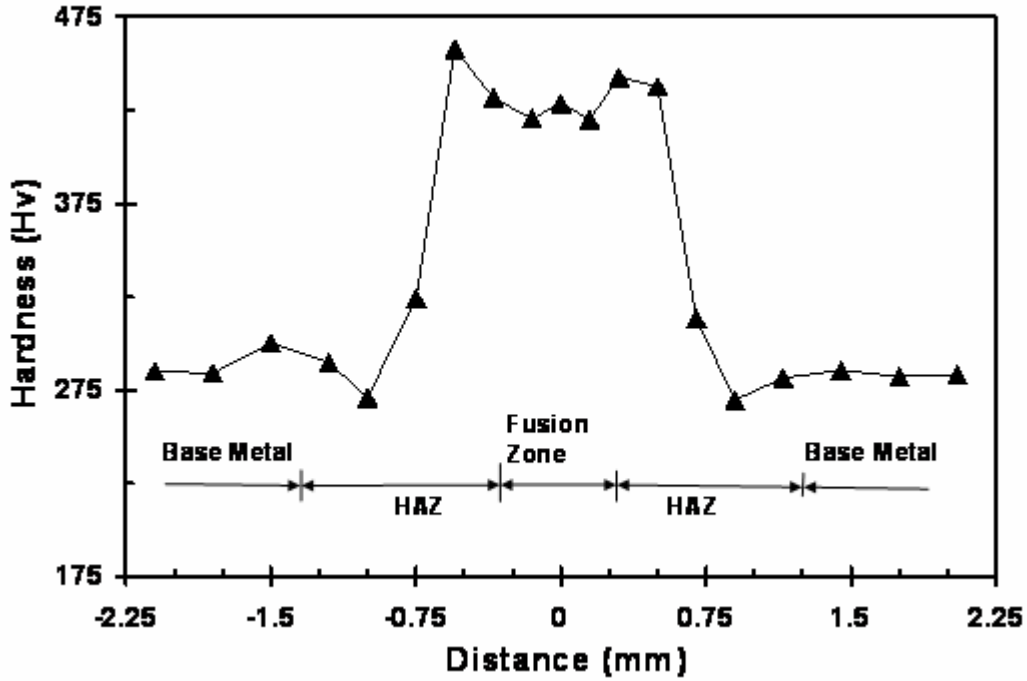


Figure 4-11 Hardness profiles of DP980 Nd:YAG welds 3 m/min [64]

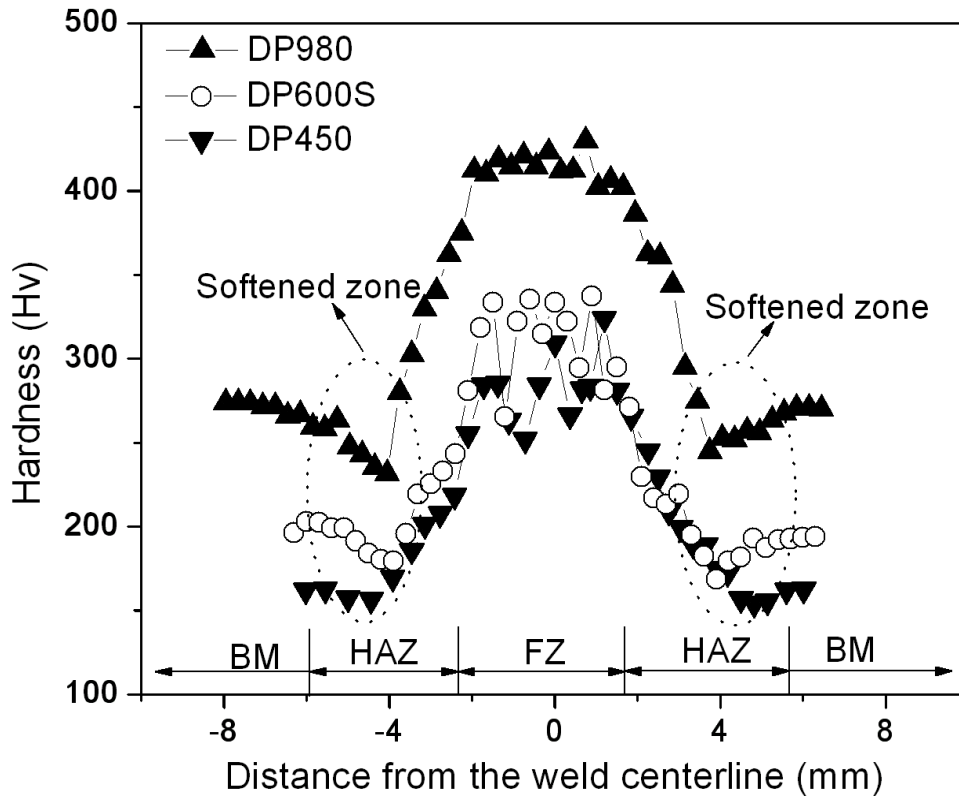


Figure 4-12 Hardness profiles across welds: Diode laser welding with speed of 1.3 m/min. BM is Base metal; HAZ is Heat affected zone; and FZ is Fusion zone. [65]

The welding speed and the mode of laser welding (conduction and keyhole) had a significant effect on the softened HAZ of the DP980 steel, affecting its location, width and the minimum hardness. Consistently, with the increase of the welding speed, the width and degree of softening were both reduced as seen in Figure 4.13. The degree of softening is represented by the hardness difference between the base metal and the minimum hardness in the softened zone.

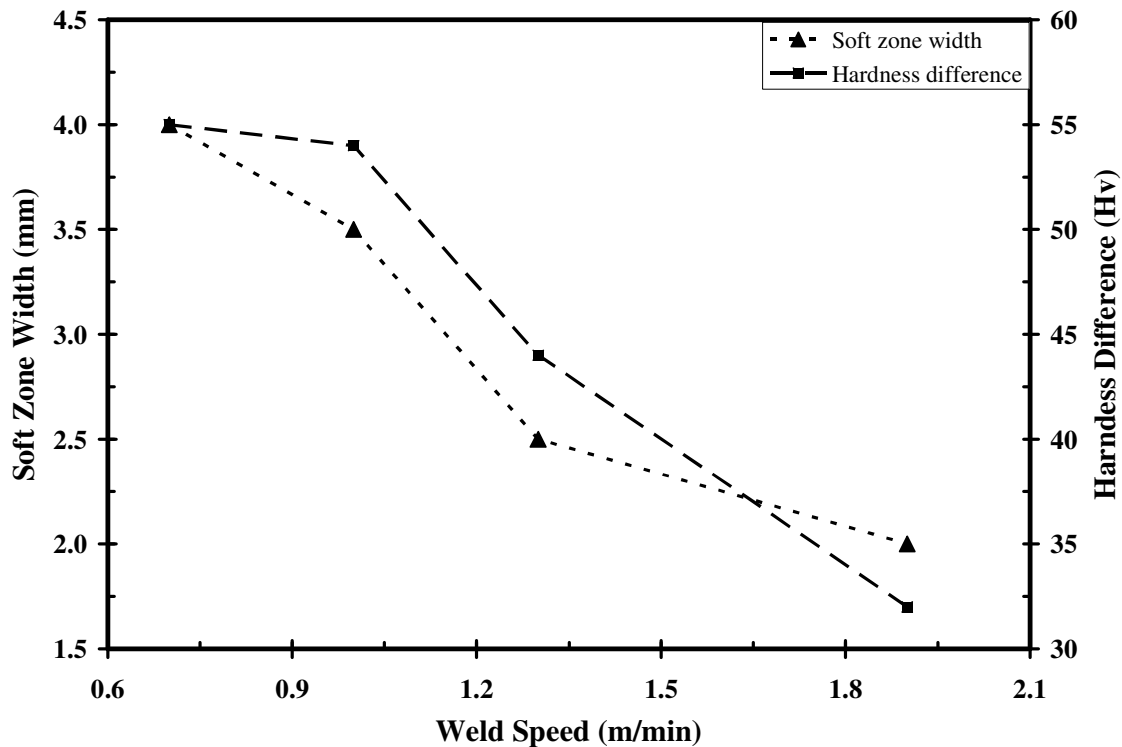


Figure 4-13 Relationship between soft zone width, degree of softening to various diode laser welding speed [64]

## 4.2 Uniaxial Tensile Testing

Uniaxial tensile testing, longitudinally (i.e. weld parallel to loading direction) and transversely (i.e. weld perpendicular to loading direction), as shown in Figure 4.14, was used to characterize weld deformation and failure modes and to evaluate the strength of welds for two different steels, HSLA and DP980. The testing results are shown in Figure 4.15 for 1.3 m/min welding speed and other welding speed results of diode laser weld are summarized in Table 4.1.

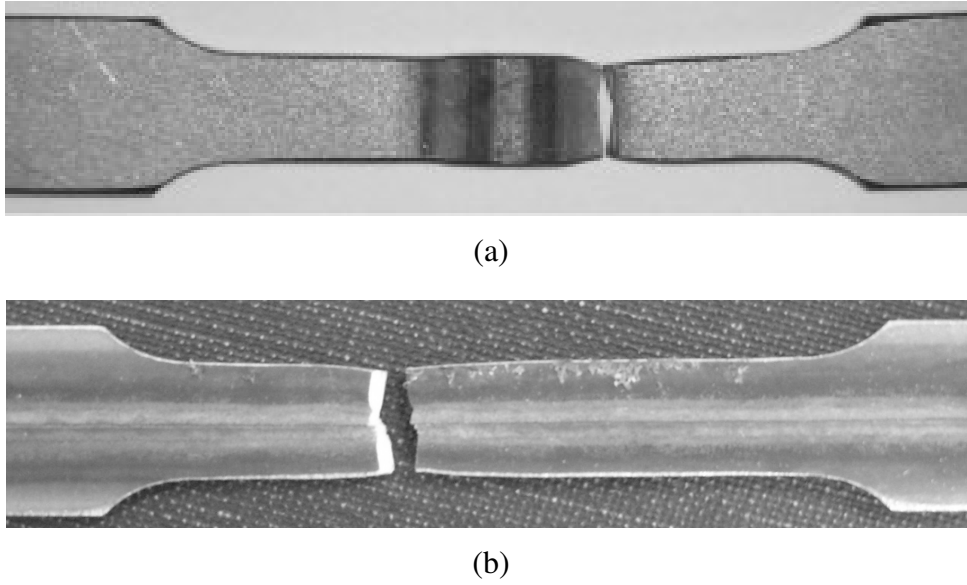


Figure 4-14 Typical tested tensile coupons for weld specimens  
(a) Transverse; (b) Longitudinal. [10]

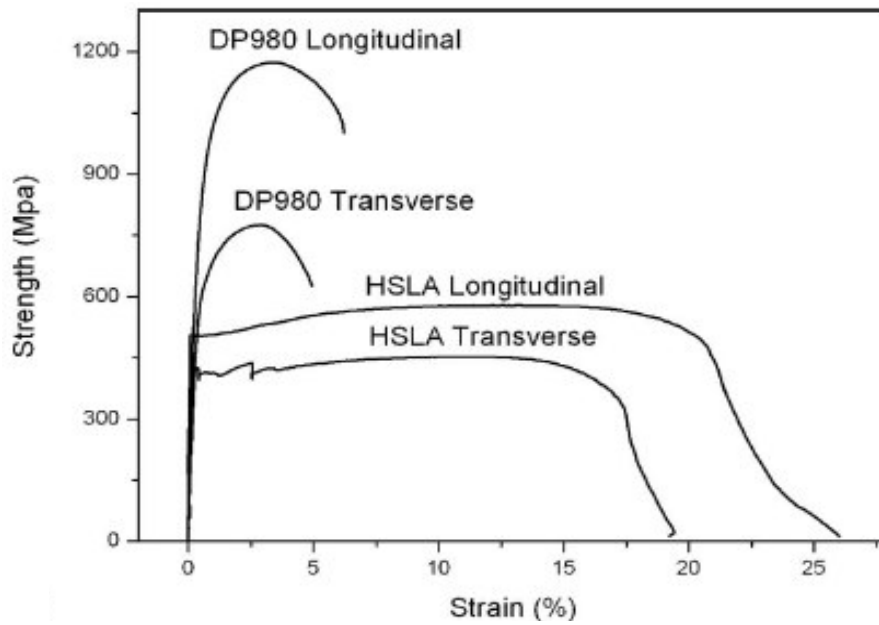


Figure 4-15 Typical stress strain curves for DP980 and HSLA transverse and longitudinal tests with the welding speed of 1.3 m/min of diode laser. [10]

Table 4-1 Tensile test results of HSLA and DP980 steel of diode laser [65]

Steel	Welding Speed (m/min)	Trans. UTS (MPa)	Trans. Elong. (%)	Long. UTS (MPa)	Long. Elong. (%)
HSLA	1.3	488	17.4	578	22.1
	1.2	467	17.2	590	18.6
	1.0	453	18.5	606	17.2
DP980	1.6	786	4.7	1213	6.5
	1.45	776	4.5	1198	5.3
	1.3	756	4.7	1246	5.3

The transverse tensile test results of the DP welds showed that the ultimate tensile strength was lower in all cases than the base metal. Furthermore, failure occurred by ductile rupture in the outer-HAZ, exactly at the location of the hardness valley (Figure 4.14 a). Examination of the deformation pattern along the transverse specimens showed that yielding occurred first in the soft zones and much of the total plastic strain was concentrated there. This led in turn to a reduction in overall specimen elongation, as necking and failure occurred in the HAZ before the balance of the specimen was fully work-hardened.

In longitudinal tensile tests, the weld metal, HAZ, and base metal zones are under equal strain, and zones of different local hardness/strength contribute in parallel to overall load-bearing capacity. All specimens showed strength in excess of the base metal (963 MPa for DP980, 470 MPa for HSLA), which was expected as the weld metal and most of the HAZ was harder than the base metal. The fracture site in longitudinal tests was randomly distributed as shown in Figure 4.14b. Interpretation of strength data from longitudinal tests is complex because each specimen is a composite of various layers having varying flow properties, including the fusion zone, continuous variation of properties in the HAZs on both sides of the weld, plus a thickness of unaffected base metal dependent on fusion zone width in relation to specimen width. Actual strength data obtained were found in each case to reasonably reflect a weighted sum of the widths of constituents present and their local flow properties based on correlation with local hardness. Recognizing the difficulties of interpreting strength data from longitudinal tensile test, these tests were

included in the investigation mainly to verify that significant embrittlement was not being included in any weld zone(s) by the welding process. However, all the HSLA welded longitudinal and transverse specimens showed excellent elongation, and showed significant amounts of plastic strain, in spite of the higher weld metal hardness than the base metal.

Local strain in the transverse tensile sample after deformation was measured using the circular grid strain analysis as described in the section 3.6.2. The grid pattern was applied along the length of the tensile sample (which includes the weld and HAZ) as shown in Figure 4.16. Smaller grid sizes are able to capture a higher gradient of strain in the material, hence a circular grid size of 2.0 mm diameter was used. As the grids get smaller than this, it is expected that their shape and size become more inconsistent. After the tensile test was complete, the deformed elliptical grids were measured to calculate the major strain along the length of the specimen and obtain a strain distribution.

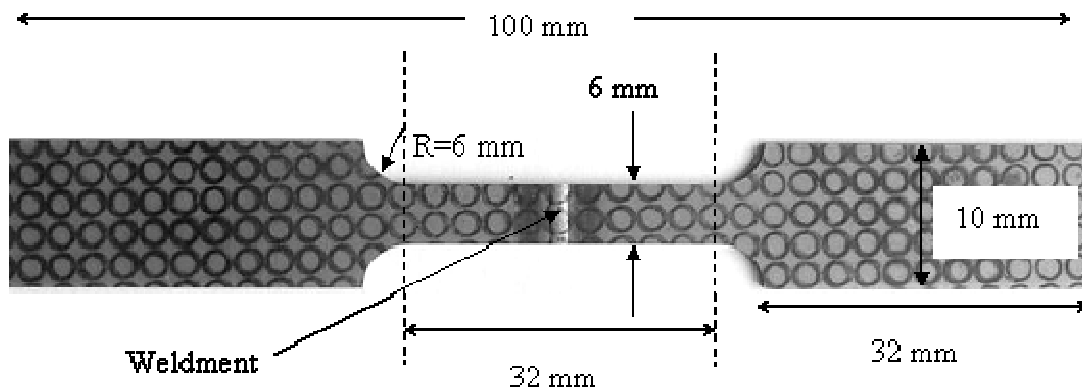


Figure 4-16 Gridded subsize tensile specimen of welded DP980 steel

Since the width of the fusion zone was very small in both diode and Nd:YAG laser welds, the standard ASTM E8 tensile specimen could not be used to give the tensile properties of the independent fusion zone. Longitudinal samples which are a composite of the fusion zone, heat affected zone, and base metal properties have been used by some [84,85] to characterize the weld metal properties. This application, however, is complicated by the presence of a softened region without known properties and cannot be used. Hence, a smaller mini-tensile specimen, as shown in Figure 3.9, was used to obtain the mechanical properties of fusion zone experimentally

The HAZ exhibited steep property gradients and varying widths with process parameters. It was impossible to prepare uniform samples for mechanical testing that represent the HAZ properties. So, in the present study the mechanical properties of HAZ were not evaluated experimentally, but were evaluated from the finite element analysis.

The standard tensile properties of 0.2% offset yield strength (YS), ultimate tensile strength (UTS), % elongation, strain hardening coefficient (n), and strength coefficient (K) for the DP980 base metal and weld zone are shown in Table 4.2. Results showed that the DP980 had fair strength and reasonable ductility (strain hardening coefficient = 0.14) for automobile part manufacturing.

Table 4-2 Mechanical properties of DP980 and its weld

	Y.S. (MPa)	UTS (MPa)	Elongation (%)	Strength Coefficient- K (MPa)	Strain Hardening Coefficient- n	Hardness (HV)
Base Metal (DP980)	534	980	15.2	1510	0.14	283
Weld	804	1361	12.1	-	-	413-429

Figure 4.17 shows the engineering stress- engineering strain curve obtained from the tensile tests for base metal and weld zone. Typical  $\log \sigma - \log \epsilon$  plots for the base metal and weld zone are shown in Figure 4.18.

In the case of the base metal, a linear fit was successfully applied (after 2.5% strain). The slope of this line was the n-value and the Y-intercept was the log K value. In the case of the weld metal, a good linear fit could not be attained, which indicated that it changed slope (n-value) during deformation. Hence the weld metal did not appear to obey the power law of hardening and the strain hardening and strength coefficients could not be determined. The strength of the weld metal increased compared to base metal as indicated by the UTS and YS, which was an outcome of the hardness increase.

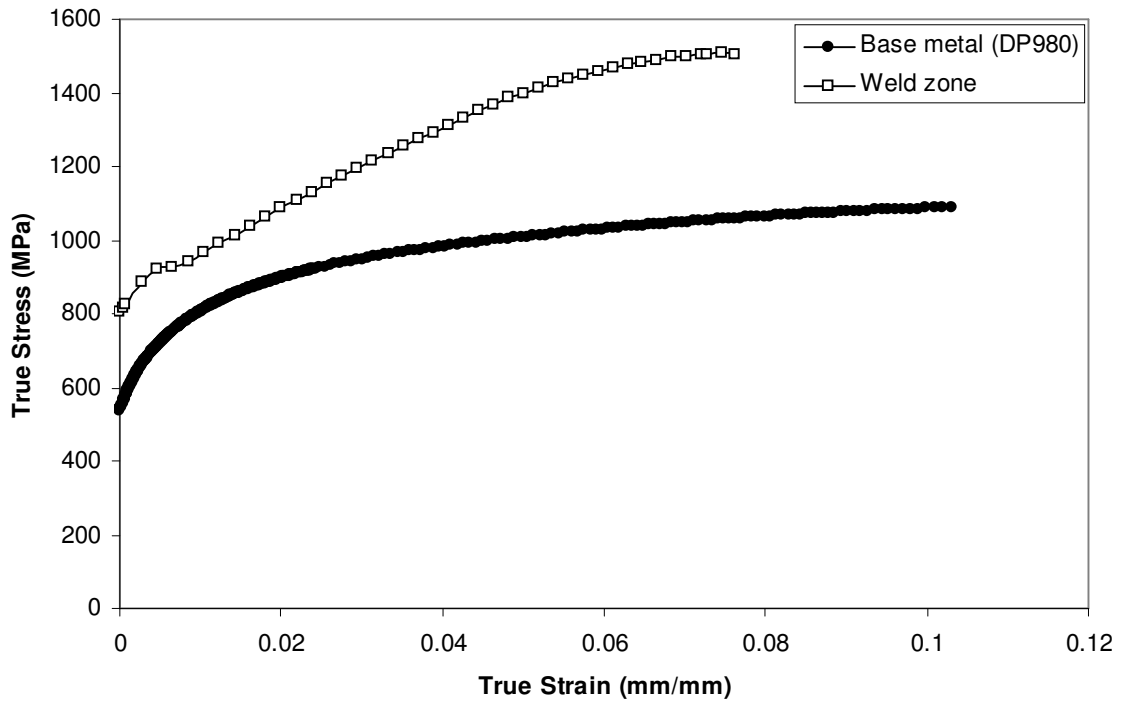
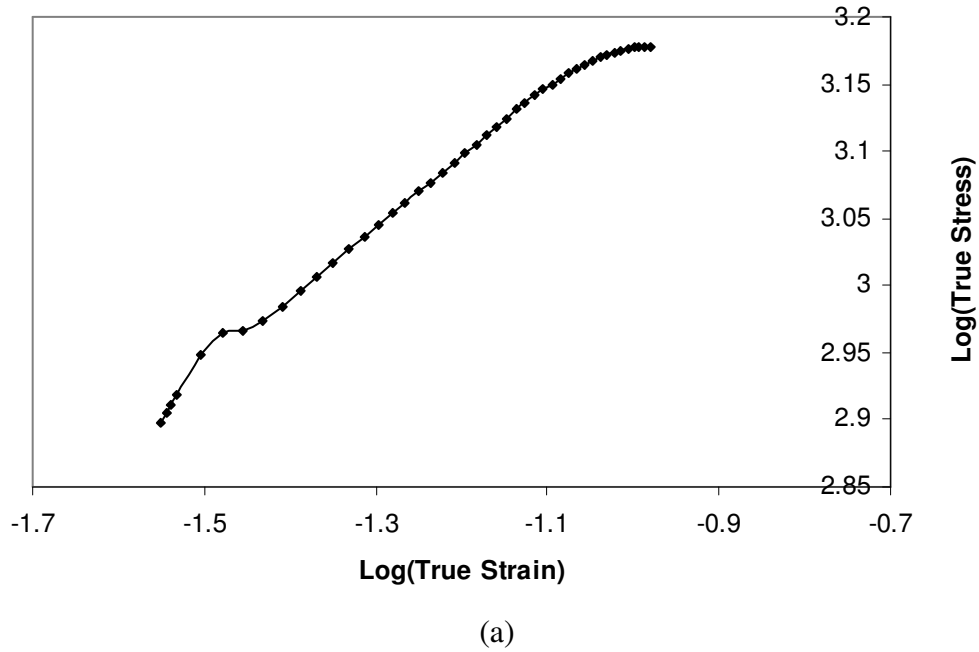


Figure 4-17 True stress- true strain curve obtained from the experiment for base metal (DP980) and weld.



(a)

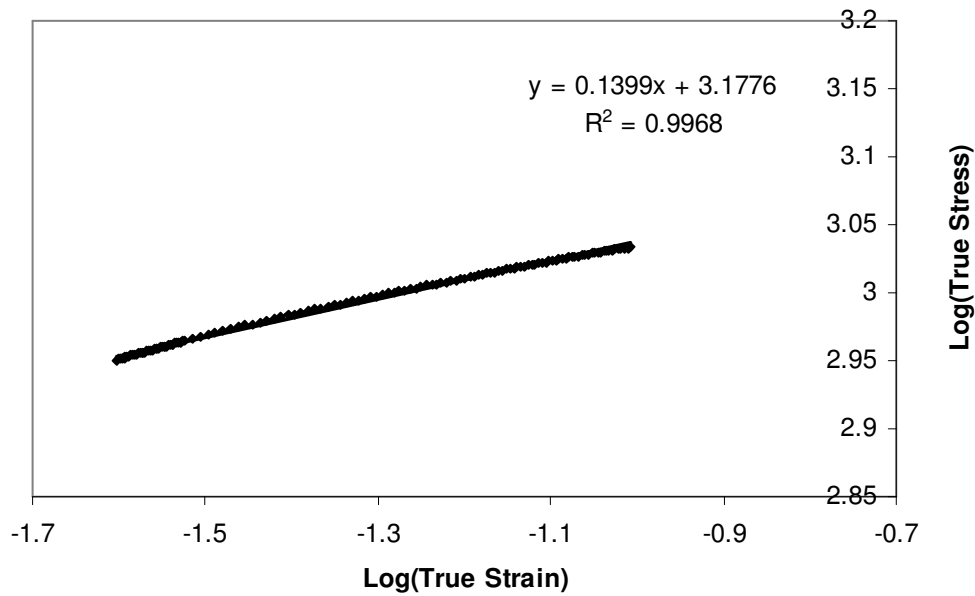


Figure 4-18 log true stress- log true

Figure 4.19 shows representative engineering stress - strain curves from tensile testing of the base metal and the transverse welded samples. The YS and UTS of the welded samples were lower than base metal values. Furthermore, overall specimen elongation was reduced, as necking and failure occurred in the softened HAZ in all the welded specimens as shown in Figure 4.20. The Nd:YAG laser welded specimen had higher strength and ductility (elongation) compared to the diode laser welded specimen. This was due to a smaller softened HAZ width and smaller drop in hardness with the Nd:YAG laser. Hence, it was observed that the transverse strength and ductility of laser welded DP980 depended on HAZ width and hardness. To further understand the effect of HAZ characteristics it was important to determine the mechanical properties (K and n- value).

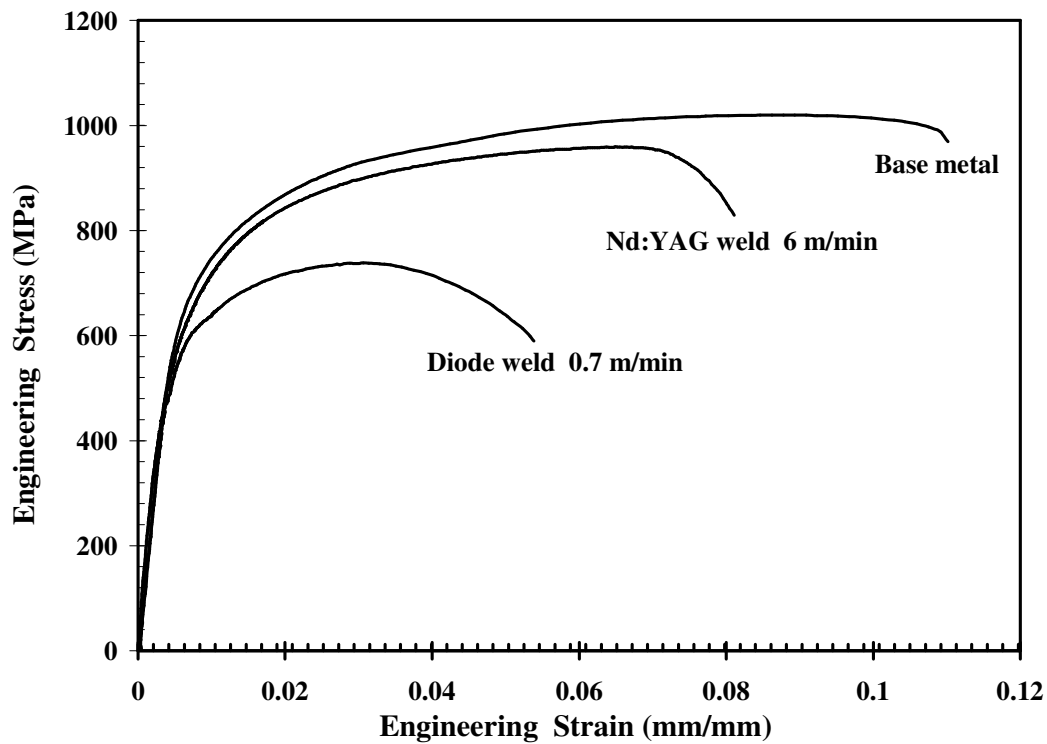


Figure 4-19 Representative results of engineering stress versus engineering strain of the uniaxial tensile tests

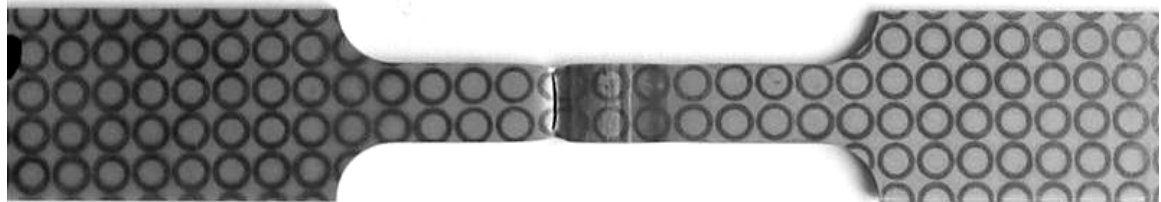


Figure 4-20 Typical tested transverse welded tensile coupon indicating fracture at the HAZ during experiment.

### 4.3 Formability Test

The formability of laser welded blanks was evaluated under biaxial strain conditions to compare different grades of the dual phase (DP) type of AHSS. Top views of tested specimens till the point of fracture are shown in Figure 4.21. Figure 4.21(a), (b), (e) are

DP980 and HSLA base metal specimens, whereas Figure 4.21(c), (d), (f) are welded deformed specimens. In DP base metal, the fracture location was at a radial distance of 17 mm from the pole and propagated in a direction parallel to the rolling direction in all tests (Figure 4.21(b)). This DP steel displayed strong directionality in terms of formability. The fracture path in dome height testing of HSLA base metal differed significantly from the DP steel. The crack followed a curved, arc path and the radial distance from the fracture path to pole was about 30mm (Figure 4.21 (e)). Fractures of laser welded specimens of both steels followed fundamentally different paths in LDH test.

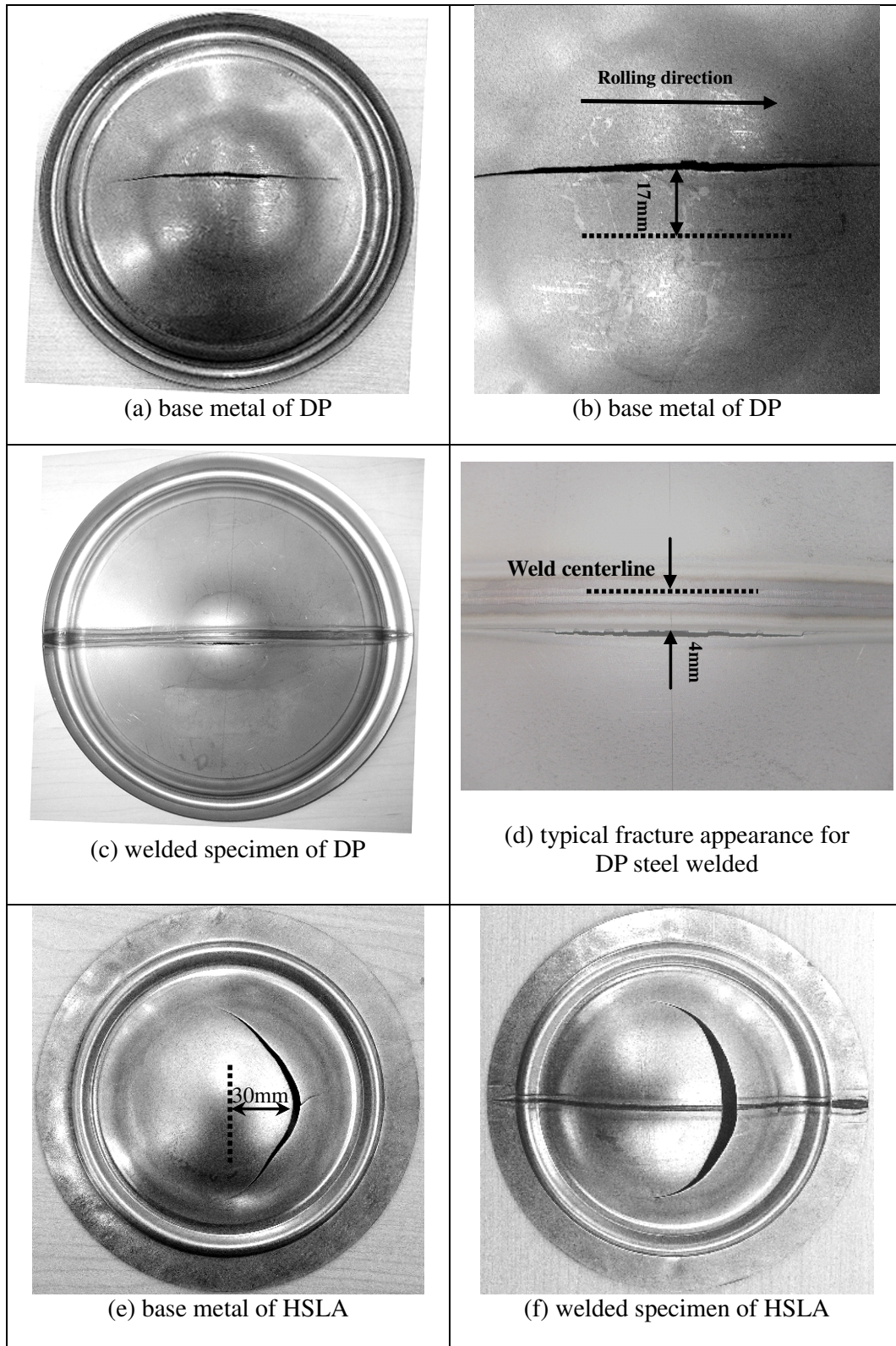
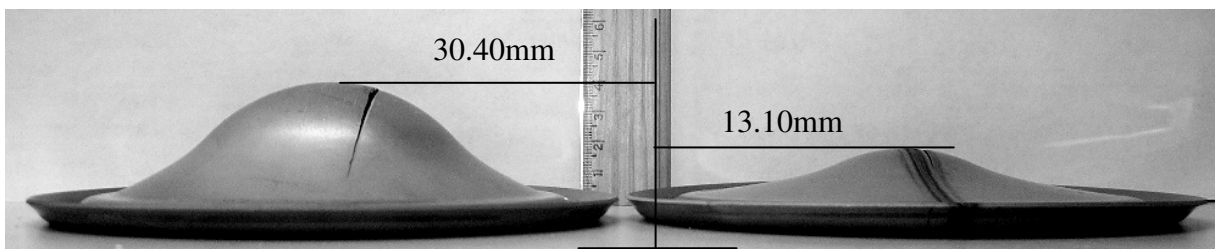
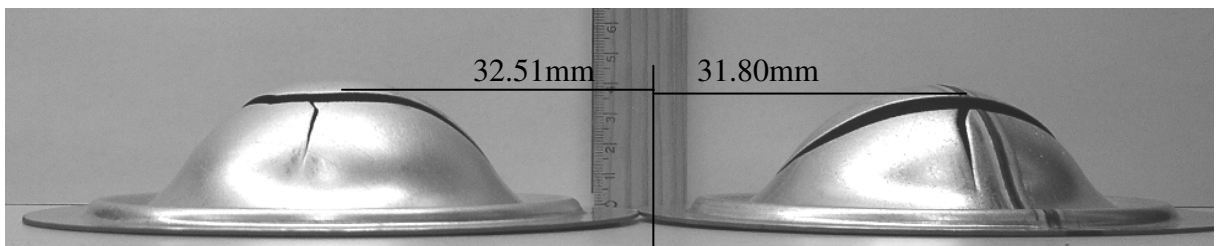


Figure 4-21 The shape of specimens after Dome Height Testing [10]

In diode and Nd:YAG laser weldments, the fracture path was always entirely in the outer HAZ, at a different radial distance from the weld centerline, with respect to the welding speed (Figure 4.21(d)). The limiting dome height (LDH) of all welded specimens is lower than that of the corresponding base metal. Hence the formability was significantly reduced due to change in material properties during welding. The formability degradation was also demonstrated by the big gap of dome height in Figure 4.22 (a). As for HSLA welded specimens, no significant difference in fracture path was observed between welded specimens and base metal. The minimum radial distance from the dome apex to the fracture path was essentially the same in base metal and welded coupons and both exhibited a curved fracture feature as shown in Figure 4.21 (e),(f). Such high consistency implied that the welding process had no significant influence on the formability of HSLA. This is also consistent with the fracture height results in Figure 4.22 (b), where strains in base metal and welded coupons were essentially equal.



(a) DP980



(b) HSLA

Figure 4-22 Side views of the LDH test specimens of (a) DP980 and (b) HSLA steel; weld speed 1.6 m/min [10]

Figure 4.23, shows load progression during LDH testing of the base metal and diode laser welded specimens (weld parallel and perpendicular to the rolling direction) of DP980

steel. The LDH of the base metal was 30.4 mm, and that of the diode welded sample was 13.1 mm. Formability of DP980 welded specimen was drastically reduced by 57% with respect to the base material. This indicates that the formability of the DP980 material was significantly reduced due to major changes in material properties following welding.

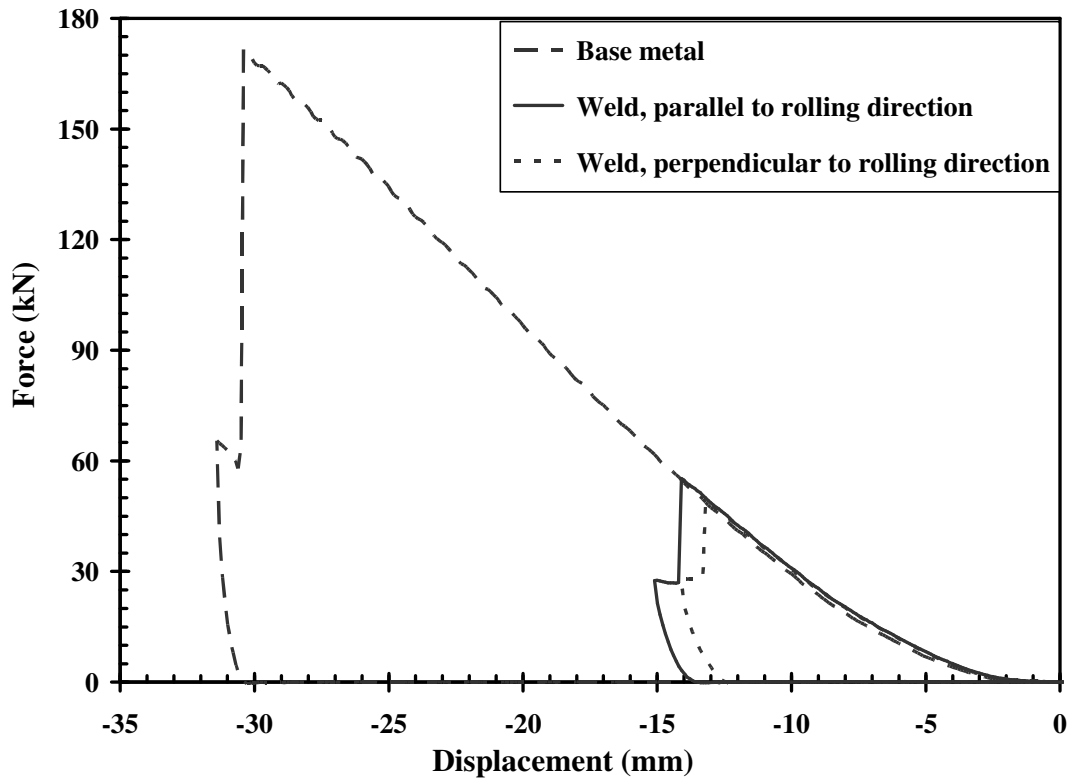


Figure 4-23 Typical limiting dome height results of the base metal and diode welded specimens at 1.6 m/min welding speed [64]

In this DP980 steel, welding direction with respect to the rolling direction of the steel did not significantly influence the formability (Figure 4.23).

Experiments were conducted for each position (the root side & face side) of the weld samples facing the punch. The LDH results for the diode weld samples, for each of the positions is shown in Table 4.3. Placing the similar thickness weld sample with face side or root side of the weld facing the punch did not significantly change the formability of the DP steel.[37].

Table 4-3 Diode laser weld orientation on the punch of the formability equipment at 2m/min [64]

Orientation	LDH (mm)
Face side	11.03
Root side	11.14

The formability of all grades of dual phase steel and HSLA was evaluated in terms of LDH and the results of the LDH tests for unwelded and welded blanks are summarized in Figure 4.24. The LDH of the base metal was in the range of 30-35 mm for all of the grades tested. The LDH of all the welded specimens was lower than the respective base metal LDH. But the LDH of the welded HSLA was nearly equal to that of the base metal. The LDH decreased continuously with increasing nominal base metal strength. The lowest LDH was observed in the welded DP980 steel, which was measured to be 13.1 mm. The fracture location was across the weld for HSLA, DP450 and DP600 as seen in Figure 4.21(f). However, fracture location was along the weld (HAZ) for DP800 and DP980 steel as seen in Figure 4.21(c).

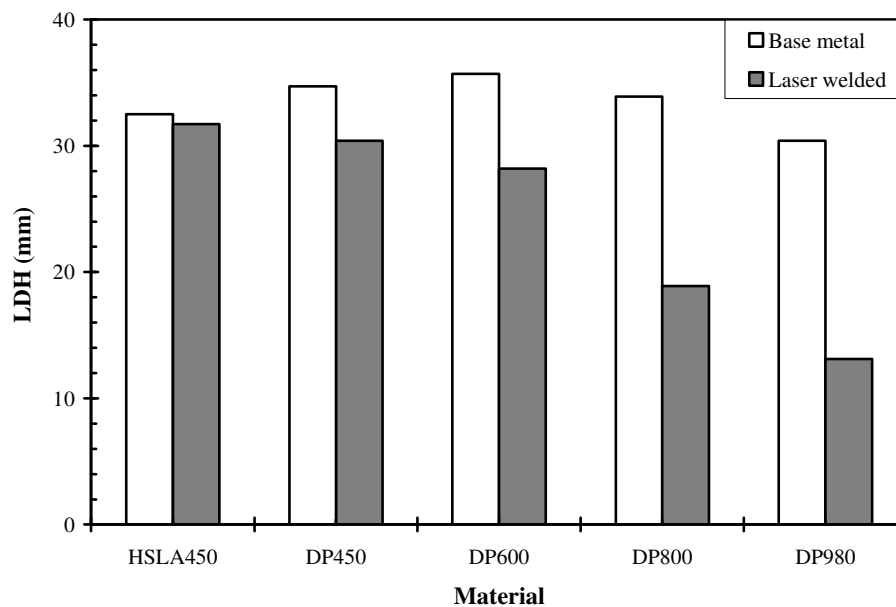


Figure 4-24 Limiting dome height of base metal and diode laser welded samples of different strength AHSS at welding speed: 1.0 m/min [65]

The formability ratio is given as in Eqn 1:

$$\text{Formability ratio} = \text{LDH of welded sample} / \text{LDH of base metal} \quad (\text{Eqn 1})$$

The formability ratio for a welded blank is defined here as the LDH of the welded blank divided by the LDH of the base metal (Eqn 1). The formability ratio can be understood as the effect of welding on the strain to failure in biaxial deformation for each of the materials. The formability ratio for LDH results given in Figure 4.24 is plotted in Figure 4.25.

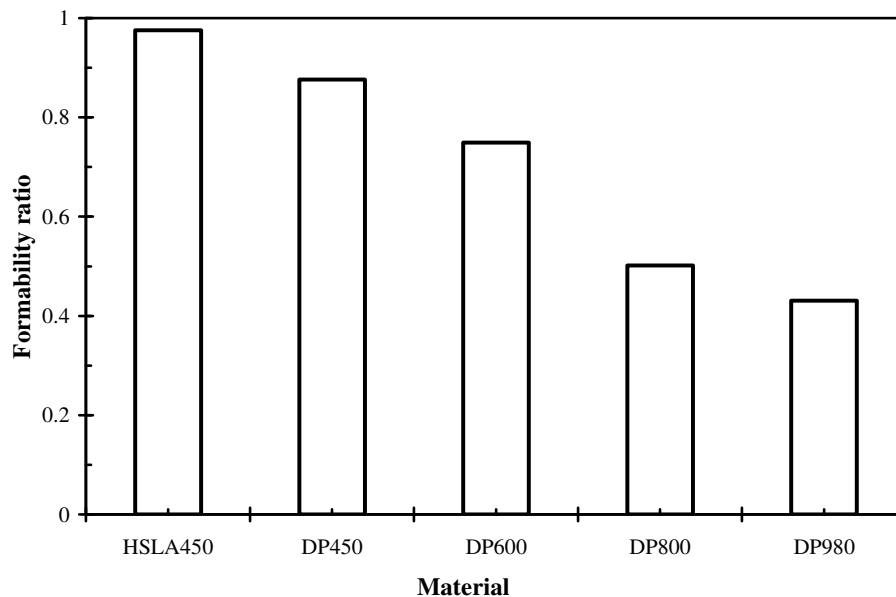


Figure 4-25 Formability ratio of different AHSS (welding speed: 1.0 m/min) [65]

There is a clear trend of decreasing formability ratio with increasing nominal base metal strength. Previous work has suggested that the reduction in formability can be attributed to metallurgical changes in the weld metal and HAZ surrounding the weld [68,63]. For example, in dual phase steels the fusion zone experiences high cooling rates after solidification typically resulting in a hardened martensitic microstructure. The high temperature heat affected zone (HAZ), just outside the fusion boundary is heated above the austenitic transition temperature and upon cooling forms a hardened microstructure that generally consists of lower transformation products martensite and bainite. Further from the fusion boundary, the maximum local temperature is too low to produce martensite; however, exposure to elevated temperatures results in tempering of the pre-existing martensite phase and concomitant softening of the microstructure. These

metallurgical changes can be associated with the mechanical properties of the welded joint, and ultimately, the formability of a welded blank.

#### **4.3.1 Effect of Softening on the Formability Properties of Welded AHSS**

The degree of softening in the HAZ can be best represented in terms of percentage reduction in hardness. Reduction in hardness is represented as in Eqn 2:

$$\text{Reduction in Hardness (\%)} = (HV_{bm} - HV_{sz}) / HV_{bm} * 100 \quad (\text{Eqn 2})$$

Where,  $HV_{bm}$  is the hardness of the base metal;  $HV_{sz}$  is the minimum hardness of the softened zone.

Figure 4.26, represents the relationship between the formability (LDH) and the percentage reduction in hardness. It was observed from the plot that larger reductions in hardness led to lower formability of the welded blanks. Different curve fitting operations were attempted to obtain the best fit for the experimental results, in which an exponential curve (shown in Figure 4.26) fitted the data well with regression coefficient (R value) of 98%.

The formability of the diode welds was less than that of the Nd:YAG welds, as the softened zone in the diode welds has larger reduction in hardness than that of the Nd:YAG welds as shown in Figure 4.26. With increase in the welding speed, formability of the welded DP steel samples approaches that of the base metal. These results indicate that there is less reduction in hardness in the softened zone for higher power laser density and higher welding speed with keyhole mode of welding. Therefore, for DP steel it is better to weld with Nd:YAG laser in keyhole mode, and at the maximum achievable welding speed to achieve higher formability.

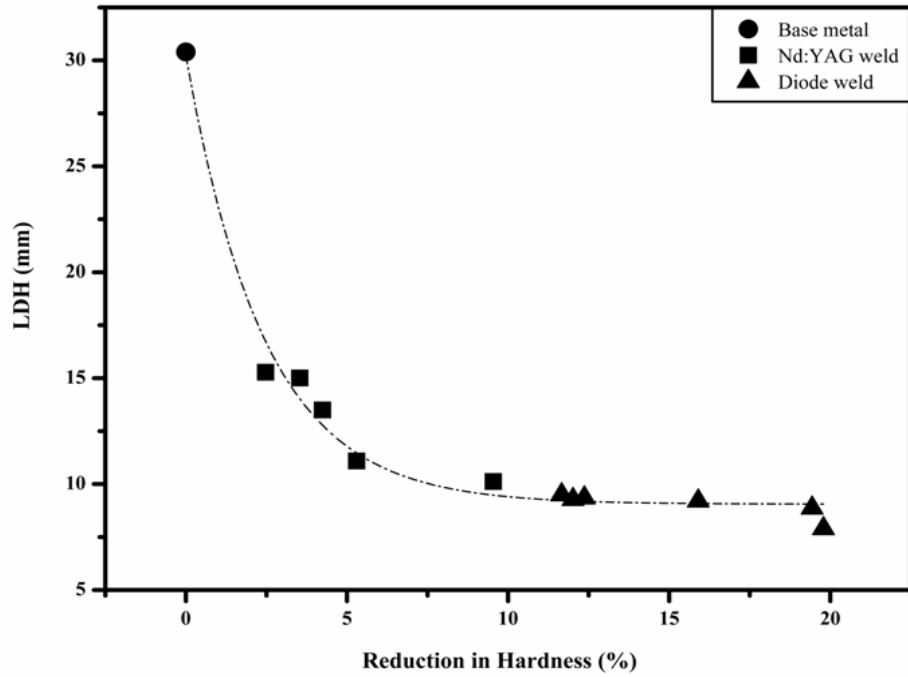


Figure 4-26 Relationship between reduction in hardness vs. limiting dome height [64]

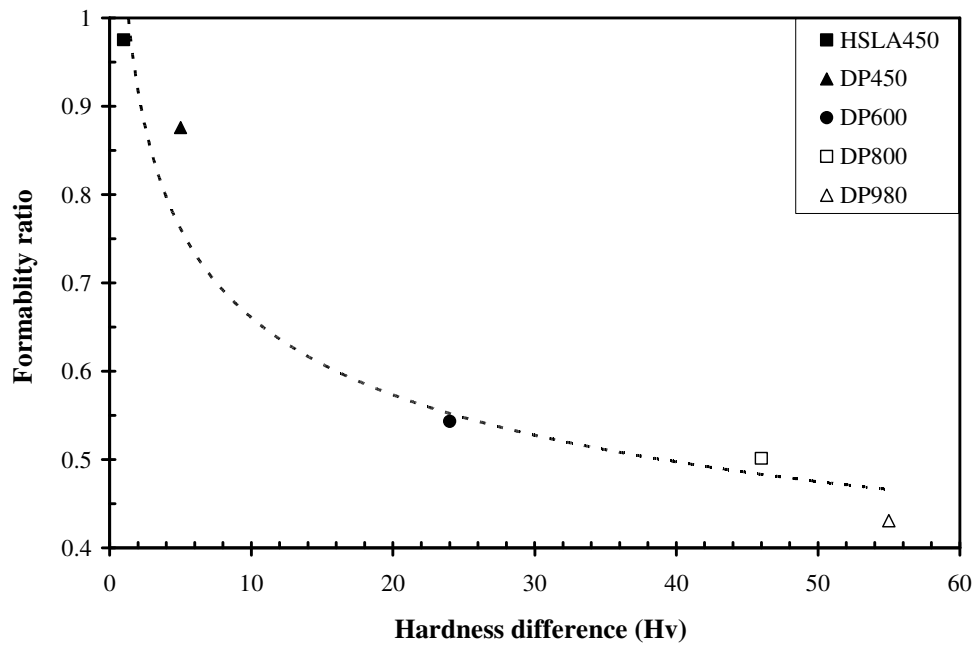


Figure 4-27 Relationship of formability ratio on the hardness ratio of different AHSS, welding speed 1.0 m/min[65]

Fig. 4.27 shows the effect of softening on the formability (interms of formability ratio) of different AHSS welded blanks. The formability ratio is plotted against HAZ softening, where softening is defined as the hardness difference between the base metal and the minimum hardness in the HAZ. The formability of the dual phase steels tends to decrease with greater susceptibility to softening.

### **4.3.2 Effect of Heat Input on the Formability Properties of Welded AHSS**

Figure 4.28 depicts the relation between formability ratio versus welding speed for welded balnks (using both the lasers) of DP980. Formability was higher for blanks which are laser welded at higher welding speed. Specific energy input to the material reduced and faster cooling rate can be achieved with increase of welding speed. This resulted in a smaller softened zone created in the specimen. For the same weld parameter, Nd:YAG welds had better formability. This was due to smaller softened zone due to the keyhole mode of welding in Nd:YAG laser but a deeper and broader softened zone in the outer HAZ was developed during welding with the low irradiance diode laser which operate in the conduction mode welding, generating a longer thermal cycle (Figure 4.1 and 4.2 ). Varying the weld speed changes the net heat input per unit length of weld. As shown in Figure 4.29, the net heat input has an effect on the formability ratio for DP980. The formability ratio decreases with increasing heat input (i.e. lower welding speed). An exponential curve fits the data well with a regression coefficient (R-value) of 98 %. Thus, it is apparent that the formability ratio is a function not only of material design, but also of the process parameters.

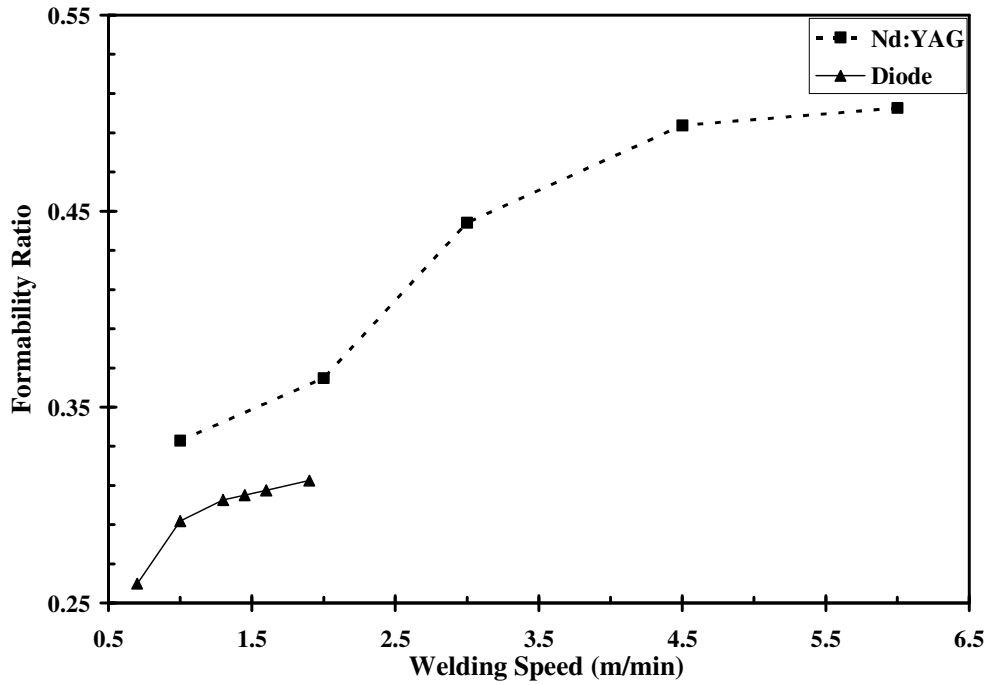


Figure 4-28 Relation between formability ratio and welding speed for welds with both lasers [64]

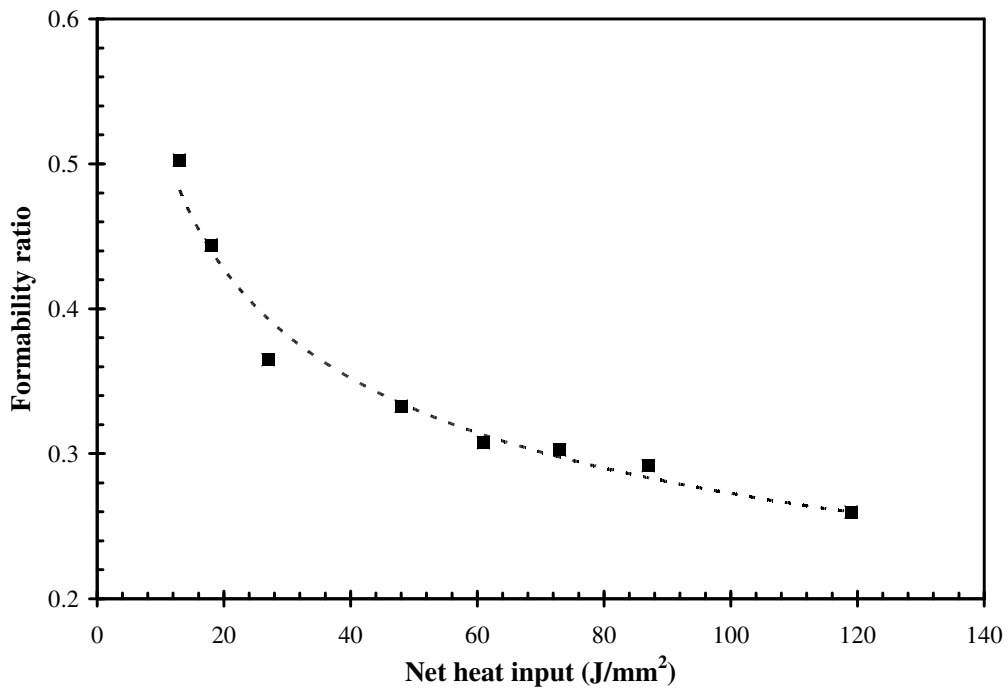


Figure 4-29 Relationship between formability ratio and the heat input of the welding process for DP980 steel [65]

### **4.3.3 Effect of Base Metal Elongation on the Formability Properties of Welded AHSS**

Two steels of the same grade, ultimate tensile strength and thickness (DP980) with different base metal elongation (martensite content) and welded with the same welding parameters (3kW, 4 m/min) were used for formability tests by Bruce et al [4]. It was observed from their work [4] that the formability of the laser welded high strength DP steel was higher when the base material elongation was higher. This result confirms the conclusion of Uchihara et al [33] that one of the influencing factor in the formability of laser welded high strength steels is the elongation of the base metal. Further, to investigate the formability of the same grade of DP steel with the same welding parameters, test welds were conducted in the present study. The base metal elongation of the DP steel used in this work was smaller than that of the two DP steels [4]. Figure 4.30 depicts the relation between the formability ratio as defined in Eqn.1 and the base metal elongation of the welded DP steels in the present work as compared to that of Bruce et al [4].

Similarly, three steels of the same grade, thickness and ultimate tensile strength (DP600) with different chemical composition and welded with the same diode laser welding parameters 4kW, 1 m/min in this work. As shown in Figure 4.31, the result validates the effect of the base metal elongation on the formability of the welded DP steel. Higher base metal elongation means higher strain hardening exponent (n-value) of the base metal. The n-value describes the material's ability to uniformly distribute deformation or elongation. Material of higher n-value will have greater uniform elongation in the presence of local strength variations and will also resist localized deformation or necking.

These result shows a good and a predictable relationship of the formability with the base metal elongation of the laser welded joint. DP steels with higher base metal elongation are preferred for the formability aspect of the laser welded specimen.

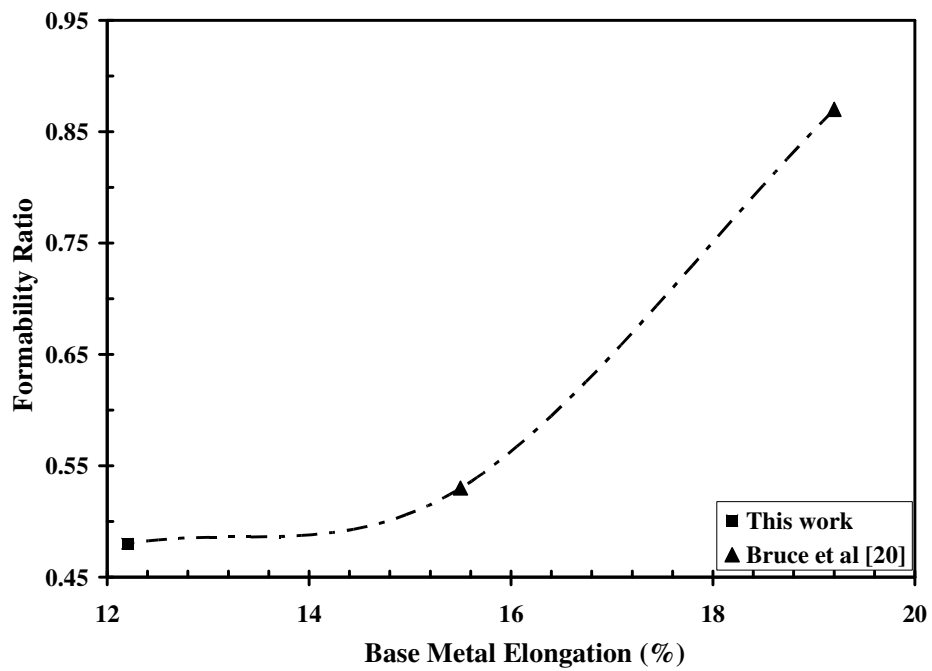


Figure 4-30 Relationship between formability ratio vs. base metal elongation of same grade of steel with laser weld with same welding parameters (3 kW, 4 m/min) [64]

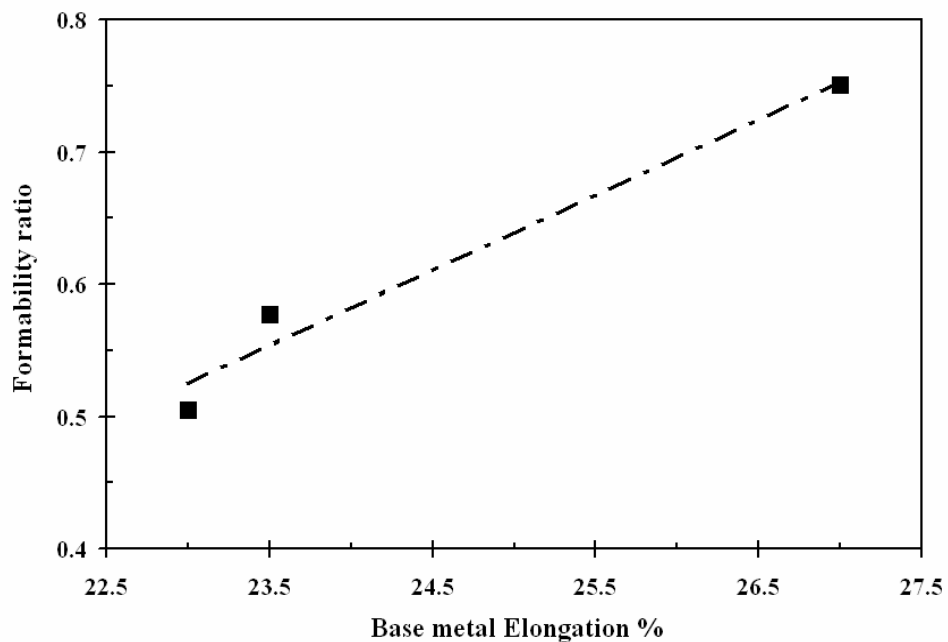


Figure 4-31 Relationship between formability ratio vs. base metal elongation of same grade of steel (DP600) with diode laser weld with same welding parameters (4kW, 1 m/min)

#### **4.3.4 Relationship between Heat Input, Minimum Hardness and the Fracture Location**

It was confirmed that fracture in the welded DP 980 steels are due to the formation of a softened zone. It is well known that increasing the heat input results in a wider HAZ, thus moving the position of maximum softening farther from the weld centerline. Higher welding speed is expected to generate faster cooling rates, which will generate the same peak temperatures in the HAZ at a shorter distance from the weld centreline. Fracture occurred slightly farther out from the weld centerline than the softest zone. It appeared that the hardened inner HAZ and the fusion zone restricted the deformation and pushed the failure farther out from the softest zone. Figure 4.32 shows relationships between the welding speed and fracture distance and softened zone distance from the weld centerline in the biaxial test (LDH). Fracture distances from the weld centreline in both the uniaxial and biaxial tests were similar. The fracture distance and softened zone distance from the weld centerline were inversely related to the welding speed (Both the soft zone and fracture location were directly related to the net heat input). Fracture distance from the weld centre was higher for diode laser weld than for Nd:YAG laser weld at the same welding speed. Since diode and Nd:YAG lasers have different power densities generating conduction and keyhole mode laser welding respectively, which evidently develop a different welding thermal cycle for the same welding speed [3] , i.e., less irradiance in diode laser resulted in a softened zone farther away from the weld centre.

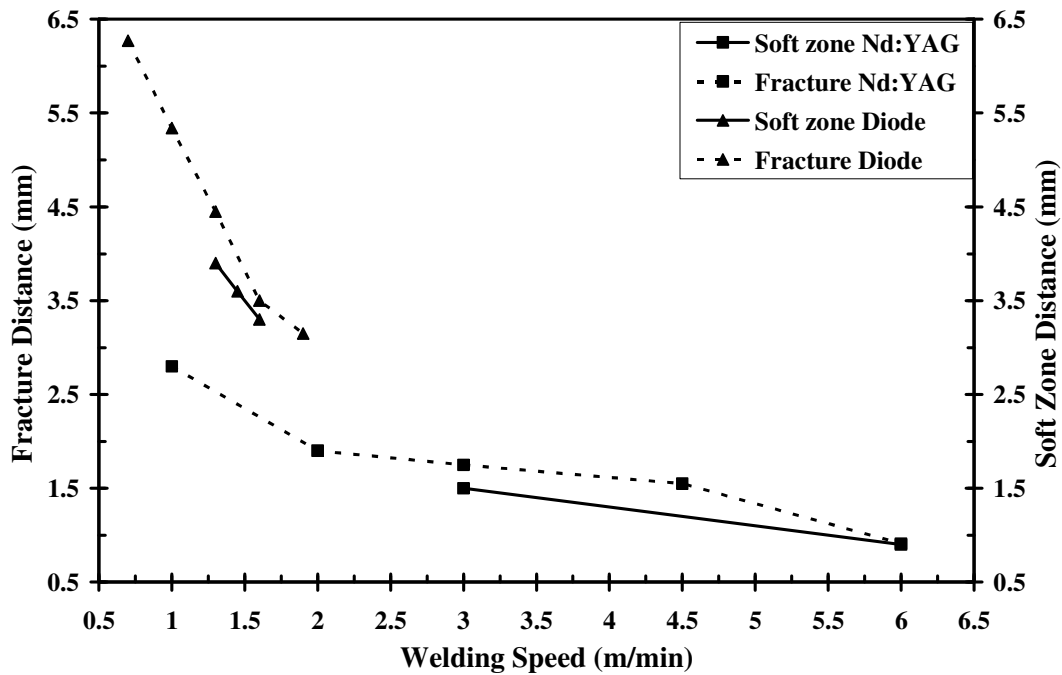


Figure 4-32 Softened zone and fracture distance from weld centre for welds with both lasers [64]

#### 4.3.5 Relationship between Uniaxial Strain and Biaxial Strain

Figure 4.33, represents the relationship between the uniaxial and the biaxial strain of the base metal and diode welded samples of the DP980 material. The average measured strain in traverse tensile tests and average measured strain in LDH tests appeared to have a stable and a predictable relationship.

The measured biaxial strain was higher than the uniaxial strain in the base metal specimen. This is consistent with the behaviour expected from the forming limit diagram (FLD) [69]. However, the measured biaxial strain was less than the uniaxial strain in welded specimens. Since the ratio of softened zone size (width) to the gauge length of the LDH specimens was smaller than the ratio of the softened zone size to the gauge length of the uniaxial tensile test specimens. Hence the localized strain concentration developed in the biaxial test will be smaller compared to the uniaxial tensile test.

The results showed that fracture and failure in both the uniaxial tensile test and the biaxial LDH test was in the outer HAZ of the laser welded DP steel, indicating that transverse tensile testing is a useful indicator for the formability of the welded DP steel.

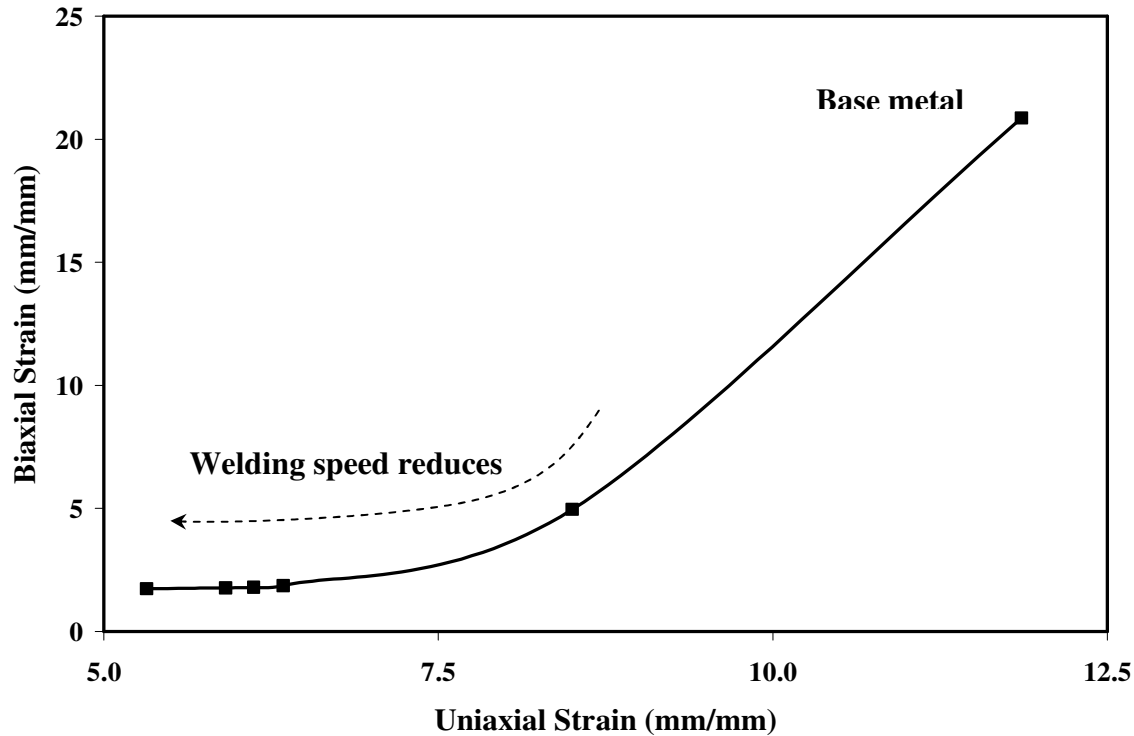


Figure 4-33 Relationship between biaxial and uniaxial strain versus weld speed [64]

#### 4.4 Summary of the Experimental Results

The present work developed tailored blanks for formability testing were simply created with identical material properties on each side of the joint by carrying out full-penetration bead-on-plate welding on square blanks pre-cut to fit the dome height testing apparatus. Comparison of the behavior of welded and unwelded blanks was thus able to focus exclusively on welding related phenomena. The formability effects of the welds made with two different power density types of laser on DP 980 steel, spanning a wide range of welding thermal cycles. The influence of the softened zone on formability was examined. The effect of welding speed/heat input on fracture distance and softened zone distance from the weld centreline was studied. Further the relationship between uniaxial and biaxial strain was examined.

## 5 Numerical Modelling

### 5.1 Introduction

Numerical simulation has become a very important tool to clarify and confirm experimental observation. The strong demand for cost reduction, shortened development cycle and high quality has required the development of computer aided engineering (CAE) simulation. FE analysis is an essential component of CAE for many fields of engineering analysis including TWB. As a development tool, Finite element analysis (FE) analysis can be invaluable for eliminating many prototyping or proof-of-concept experiments. Having the flexibility to test new parameters and test configurations led to the development of the uniaxial tensile and biaxial formability experiment.

In this work, FE analysis focuses on the uniaxial tensile test of the base metal (DP980) and the autogenously laser welded DP980 steel sheets in transverse direction. The objectives was to look into the validation of numerical simulation results with experimental results, the influence of tensile strength and the width of the soft zone on the overall load bearing capacity and the elongation of the weldments. The geometry, material properties and the boundary condition of the numerical model was created and meshed by the help of the commercially available pre-processor called Hypermesh. FE analysis was done by a commercially available code LSDYNA

### 5.2 Theoretical Back ground

The transverse weld specimen was a heterogeneous structure with different material properties across the various regions of the weldment, such as fusion zone, inner and outer HAZ, and base metal. Each of these zones can be modelled by their individual mechanical properties, where available. Figure 5.1 depicts a schematic overview of the half side of tensile test sample with 3 different zones within the gauge length., where  $l_0$  ( $l$ ) is the initial (final) overall length of the specimen,  $l_1^0$  ( $l_1$ ) the initial (final) length of fusion zone,  $l_2^0$  ( $l_2$ ) the initial (final) length of HAZ and  $l_3^0$  ( $l_3$ ) the initial (final) length of base metal. The final length of each region will be different not only due to different initial length of each region but also due to different amount of strain in different region

during deformation.

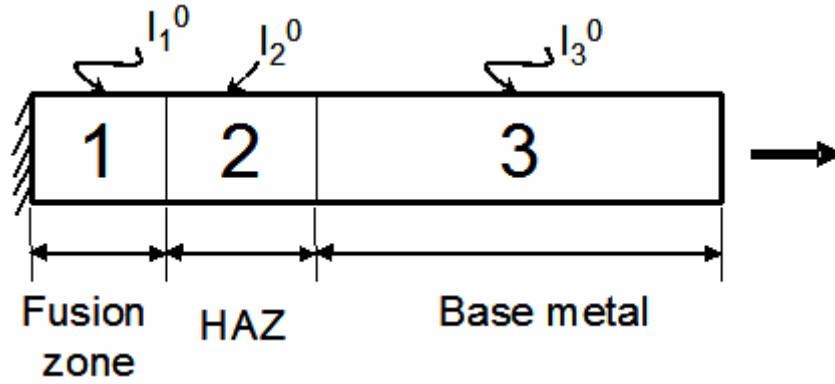


Figure 5-1 Schematic view of half the tensile sample.

Initial total length of the sample is represented as

$$l_0 = l_1^0 + l_2^0 + l_3^0 \quad (1)$$

And final length as

$$l = l_1 + l_2 + l_3 \quad (2)$$

Total true strain is as given as

$$\epsilon^e = \ln \frac{l}{l_0} = \ln \frac{(l_1 + l_2 + l_3)}{(l_1^0 + l_2^0 + l_3^0)} \quad (3)$$

Each zone is governed by its own constitutive equation as

$$K_1 \cdot \epsilon_1^{n_1} = K_2 \cdot \epsilon_2^{n_2} = K_3 \cdot \epsilon_3^{n_3} = \sigma \quad (4)$$

Where,  $K_1$ ,  $n_1$ ,  $K_2$ ,  $n_2$  and  $K_3$ ,  $n_3$ , are the strength coefficient and strain hardening exponent of the fusion zone, HAZ, and base metal, respectively. As the area of cross section is same in all the regions, the stress will be uniform through out the region. But

due to difference in mechanical properties (K and n- values), each region will have different deformation and this will lead to non-uniform deformation.

For each zone the strain will be as follows

$$\left. \begin{aligned} \varepsilon_1 &= \ln \frac{l_1}{l_1^0} \\ \varepsilon_2 &= \ln \frac{l_2}{l_2^0} \\ \varepsilon_3 &= \ln \frac{l_3}{l_3^0} \end{aligned} \right\} \quad (5)$$

Using equation (3), (4) and (5) we get

$$\varepsilon^e = \ln \frac{l}{l_0} = \ln \left( \frac{e^{(\sigma/K_1)^{1/n_1}} l_1^0 + e^{(\sigma/K_2)^{1/n_2}} l_2^0 + e^{(\sigma/K_3)^{1/n_3}} l_3^0}{l_1^0 + l_2^0 + l_3^0} \right) \quad (6)$$

From this equation it can be understood that the displacement and force developed in each region is governed by its strength coefficient and initial length. Hence for the FEM simulation of the heterogeneous transverse weld specimen, the effect of strength and size of HAZ should be studied.

### 5.3 Experimental Tensile Testing

The experimental results of the transverse tensile testing of the DP980 steel are discussed in detailed in the section 4.2 of experimental result.

### 5.4 FE Modeling

Numerical simulation of tensile test was done by the LS-DYNA-971 FEA software package (this solver handles material and geometrical non-linearities in solving the quasi-static sheet metal forming process very well) [73]. The model was created and meshed by quadratic 2D shell elements with 5-integration points by the help of the commercially available pre-processor called Hypermesh.

The sub-size transverse TWB tensile specimen was divided into three main regions. Each region was joined with the adjacent region by merging of common nodes. As the sample was symmetric in both the longitudinal and transverse directions, only a quarter of the whole sample was modeled. The weld centre (seam) coincided with the transverse symmetrical line. The solution domain was discretized by 5263 quadrilateral shell elements. A refined mesh was used in the weld and HAZ area to account for the rapid change of stresses in these areas (shell element dimension of 0.1 mm x 0.1 mm) [74].

Figure 5.7 shows the TWB tensile specimen along with the boundary conditions. In order for the quarter model to represent the full specimen, both X and Y constraints were imposed on the nodes along the transverse and longitudinal symmetric line respectively. Displacement in X-direction was applied to the nodes at the end of the grip portion. This displacement is equal to the final displacement obtained during the tensile test.

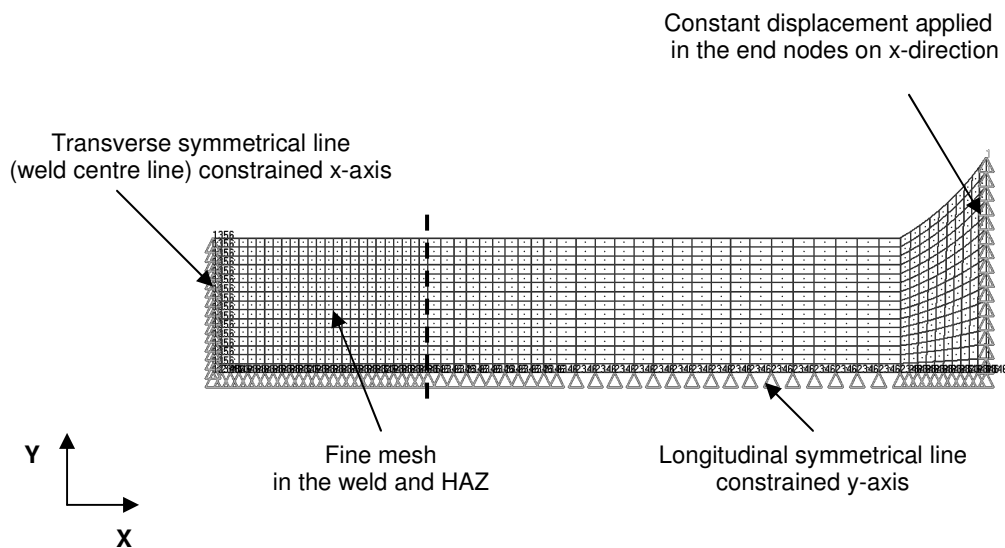


Figure 5-2 Mesh for the quarter model of tensile specimen with constraints in the X, Y plane

The model was considered as a deformable body with appropriate yield criterion and stress-strain relation during non-linear plastic deformation to account for strain hardening. The yielding behaviour of the blank material was considered as per Von-Mises yield criterion. The simplest way to represent this criterion is  $f(I_2) = I_2 = C$ .

Where  $I_2$  is the second invariant of the stress tensor and  $C$  is a material constant. The second invariant ( $I_2$ ) of stress tensor can be expressed in terms of stress deviator tensor as  $I_2 = \frac{1}{2} S_{ij} S_{ij}$ . Here, the Einstein summation convention is used. Hence Von-Mises criterion for plastic flow can be expressed as  $S_{ij} S_{ij} = \frac{2}{3} \sigma_{yp}^2$ , where  $\sigma_{yp}$  is the yield stress of the material in uni-axial tensile test [75]. This quadratic yield condition in the cartesian principal stress ( $\sigma_1, \sigma_2, \sigma_3$ ) space is represented by the following equation in terms of principal stresses.

$$\left[ \frac{1}{2} \{ (\sigma_1 - \sigma_2)^2 + (\sigma_2 - \sigma_3)^2 + (\sigma_3 - \sigma_1)^2 \} \right]^{\frac{1}{2}} = \sigma_{yp} \quad (7)$$

For uniaxial tensile test it simplified to

$$\sigma_1 = \sigma_{yp} \quad (8)$$

Where  $\sigma_1, \sigma_2, \sigma_3$  are the principal stresses in three direction and  $\sigma_{yp}$  is the yield stress of the material.

The stress-strain relationship during deformation was approximated by the following constitutive equation in the numerical model. This takes into non-linear work hardening behaviour of the material.

$$\sigma_y = K \varepsilon^n = K (\varepsilon_{yp} + \bar{\varepsilon}^p)^n \quad (9)$$

where  $\sigma_y$  = flow stress,  $\varepsilon_{yp}$  = strain to cause yield,  $\bar{\varepsilon}^p$  = effective plastic strain

K is strength coefficient and n is strain hardening coefficient.

The elastic strain at yield can be found from [73]:

$$\varepsilon_{yp} = \left[ \frac{\sigma_{yp}}{K} \right]^{\left[ \frac{1}{n} \right]} \quad (10)$$

The K and n value of the base metal was obtained by fitting a power law function to the true stress and true strain curve obtained from the experiment. It was done by calculating the log true stress and log true strain values in the uniform plastic deformation range (between YS and UTS) and using linear regression (least square method), a best fit was

plotted. The slope of this line gives n-value and Y-intercept gives log K [76]. In the case of the fusion zone, the material did not obey the power law of hardening, and the true stress and true strain curve was imported for that material model by the help of a subroutine including the stress-strain data in the program. The LSDYNA-971 solver has the ability to evaluate stress and strain for the material at each stage of deformation by interpolating from the data points that were imported for the stress-strain curve [73]. It was assumed that the softened HAZ obeys the power law of hardening during deformation. As previously discussed, experimental determination of the strength coefficient and strain hardening exponent for the HAZ was not possible. For simulation purposes, these values were obtained through a pragmatic process optimization until the load-displacement curve matched well with the experimental result (by comparing the load-displacement curve obtained from both the experiment and FE simulation i.e. different combinations of the K and n-values were tried to fit the best with the experimental load vs. displacement curve).

## **5.5 Comparing the Numerical Simulation Results with the Experimental Results**

Initially comparison of the FEM simulation results with the experimental load-displacement curve for the DP980 base metal is shown in Figure 5.8. The predicted and experimental curves matched reasonably well with a small discrepancy in the initial portion of the curve.

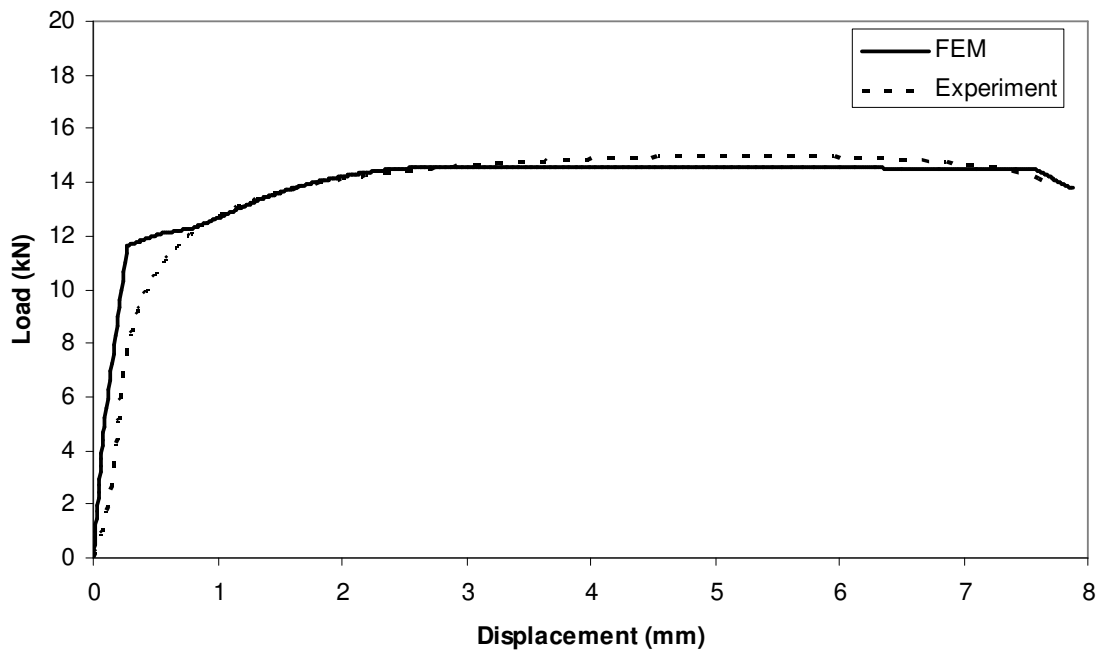


Figure 5-3 Comparison of load-elongation curve obtained from experiment and numerical simulation for DP980 steel.

This was a result of the approximation of power law hardening by assigning a constant  $n$ -value throughout plastic deformation. In the measured curve, during the initial phase of plastic deformation the  $n$ -value was not constant until a strain of 2.5%.

FE analysis of the welded samples which consisted of base metal, HAZ, and fusion zone was done to evaluate the effects of HAZ properties. The fusion zone and HAZ dimensions were taken from the experimental results and are shown in Table 5.1.

Table 5-1 Fusion zone and the soft zone width obtained during laser welding experiments.

Laser	Weld speed (m/min)	Laser specific energy( $\times 10^3$ kJ/m <sup>2</sup> )	Experiment soft zone (mm)	Experiment fusion zone (mm)
Diode	0.7	381	4.0	3.5
Diode	1.3	205	2.5	3.2
Diode	1.9	140	2.0	3.2
Nd:YAG	3.0	100	0.75	0.75
Nd:YAG	6.0	50	0.5	0.5

The mechanical properties for the base metal were modelled with the parameters obtained experimentally. The material properties of the weld zone were modelled by importing the measured true stress - true strain curve into the LSDYNA-971 code (as the weld zone could not be modelled by the power law of hardening). It was assumed that this curve was valid for all welding parameters for both diode and Nd:YAG laser welds. Table 5.2 gives the mechanical properties (k, n value) of the soft zone for the diode and Nd:YAG laser weld respectively obtained from curve fitting. To get the mechanical properties (K and n-value) of the HAZ, trial input parameters are given and the output load-displacement was matched with the corresponding experimental results.

Table 5-2 Mechanical properties for the HAZ compared to base metal in the welded samples.

Properties	Nd:YAG Laser		Diode Laser	
	Base Metal	HAZ	Base Metal	HAZ
n-value	0.14	0.17	0.14	0.19
K-value (MPa)	1510	1408	1510	1290

When the curves matched, the corresponding K and n- values were adopted as the mechanical properties of the softened HAZ. Figure 5.9 shows the matching of load-

displacement curves obtained from experimental and numerical simulations for different welded samples.

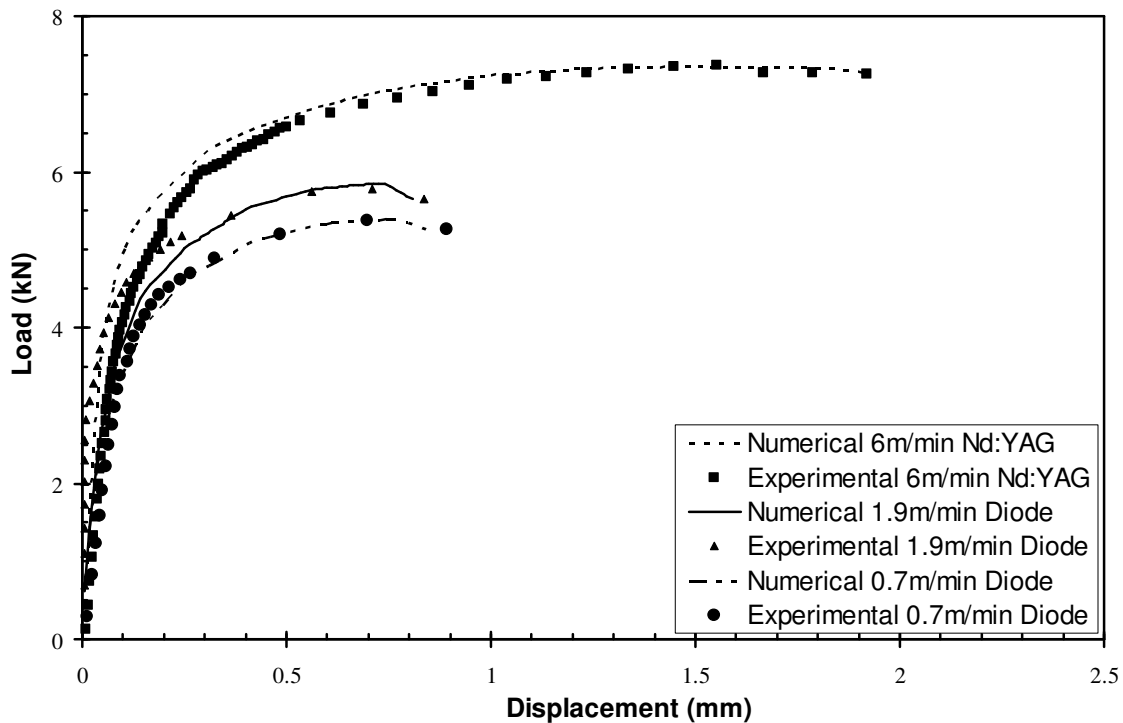


Figure 5-4 Comparison of experimental and numerical result of load vs. displacement in the DP980 steel for diode laser and Nd:YAG laser weld.

To validate the model, the strain distribution obtained from experimental results and FEM simulations were compared. Figure 5.10 depicts the comparative results of the local strain of the experimental and numerical analysis. The simulated distribution matched reasonably well and it was seen that major plastic strain has taken place only in the softened HAZ as seen in Figure 5.11. For the simulations, the major strain values were calculated at the gauss point and then extrapolated to the nodes which had a high density in the softened HAZ. However, in the experimental specimen, the softened HAZ is contained within the span of one circular grid point and only one major strain value was obtained. In both experimental and numerical results, the major plastic strain is less than 8% in both the fusion zone and base metal, while in the case of the HAZ it is above 35%.

The fusion zone and base metal in both the numerical and experimental distribution did not experience significant plastic strain, while the maximum plastic strain occurred in the softened HAZ. This led to localized deformation and fracture of the sample.

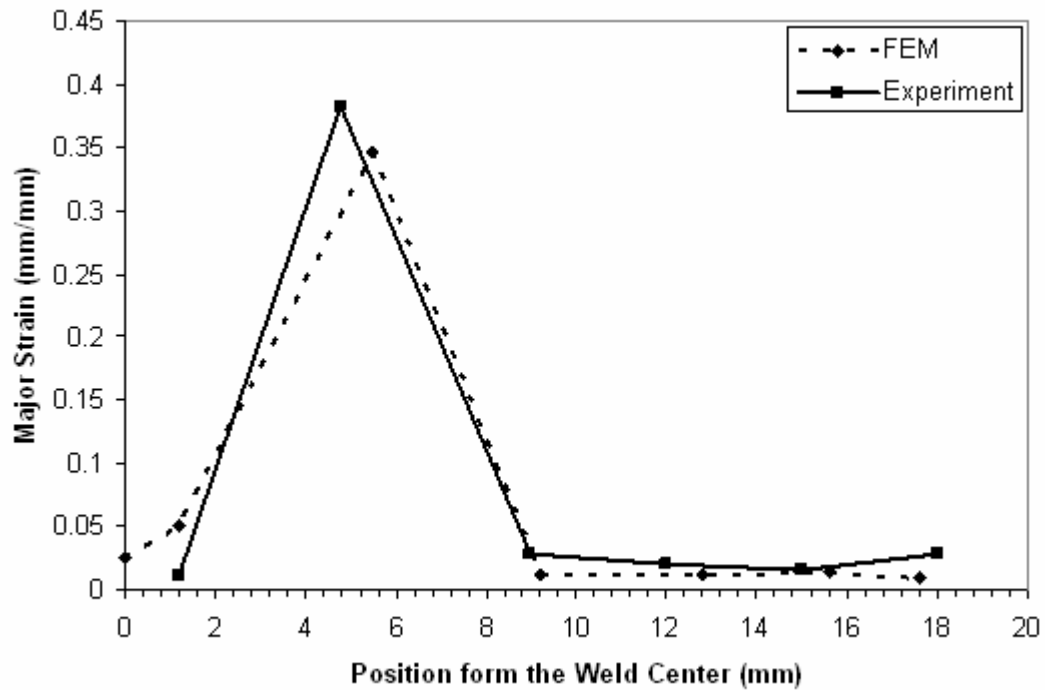


Figure 5-5 Comparison of experimental and numerical plastic strain in the transverse welded tensile specimen of DP980 steel (diode laser welding).

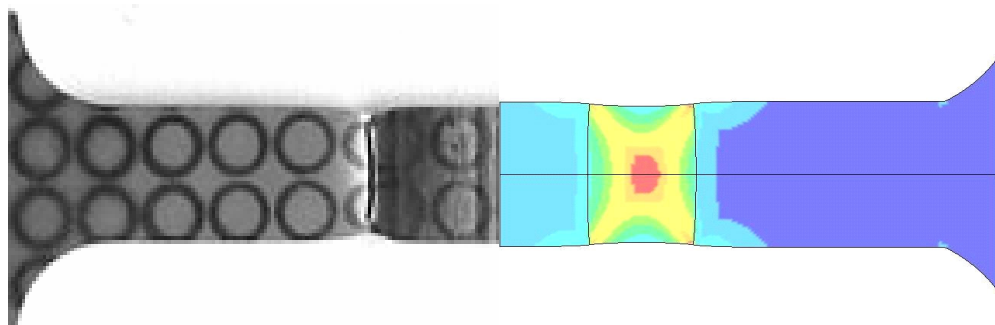


Figure 5-6 Strain localisation is high in softened HAZ in DP980 steel welded sample in experiment and FEM simulation.

## 5.6 Effect of Softened HAZ Material Properties on the Overall Strength and Elongation

The effects of both material properties and size of the softened HAZ were studied individually. Tabor [76] estimated that the best correlation between Vickers hardness,  $H_v$ , and the flow stress occurs at a strain of 8% as following.

$$H_v = C\sigma_{0.08} \quad (11)$$

where  $C$  is a material constant.

In the work-hardening region the stress–strain curves follows Holloman’s equation.

$$\sigma = K\varepsilon_p^n \quad (12)$$

where  $\varepsilon_p$  is the plastic deformation,  $K$  the strength coefficient and  $n$  the hardening exponent.

For  $\varepsilon = 0.08$  the flow stress should be

$$\sigma_{0.08} = K(\varepsilon_{p,0.08})^n \quad (13)$$

where  $\varepsilon_{p,0.08} = 0.08 - \varepsilon_e$  and  $\varepsilon_e$  being the elastic strain.

From equations (11) and (13) the relation between hardness and strength coefficient is obtained

$$H_v = CK(\varepsilon_{p,0.08})^n \quad (14)$$

So in the simulations different  $K$  values (1510, 1450, 1410, 1370 and 1300 MPa) were used to define the HAZ properties to indirectly vary the hardness of this region. But in all the simulations the width of HAZ was kept constant at 0.5 mm. Figure 5.12 shows the effect of HAZ strength on the maximum load and displacement of the transverse weld uniaxial tensile test sample. It was found that with decreasing strength (hardness) of the softened HAZ the overall load bearing capacity of the welded joint decreases along with the displacement of the tensile sample.

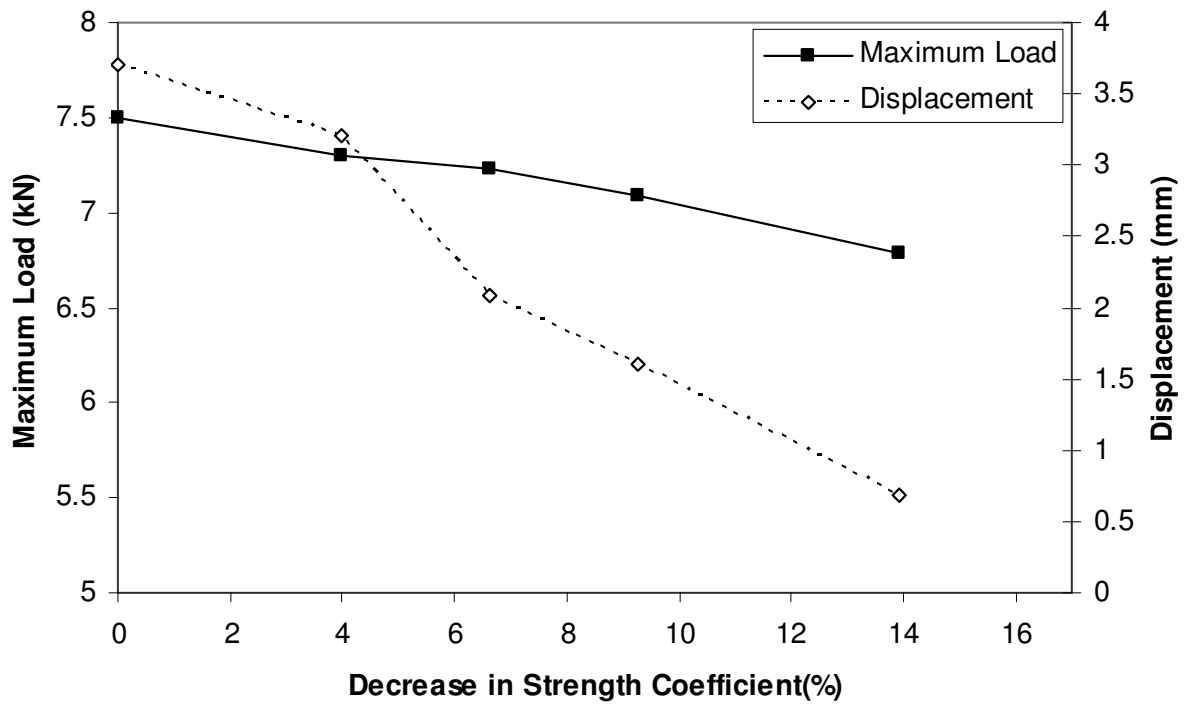
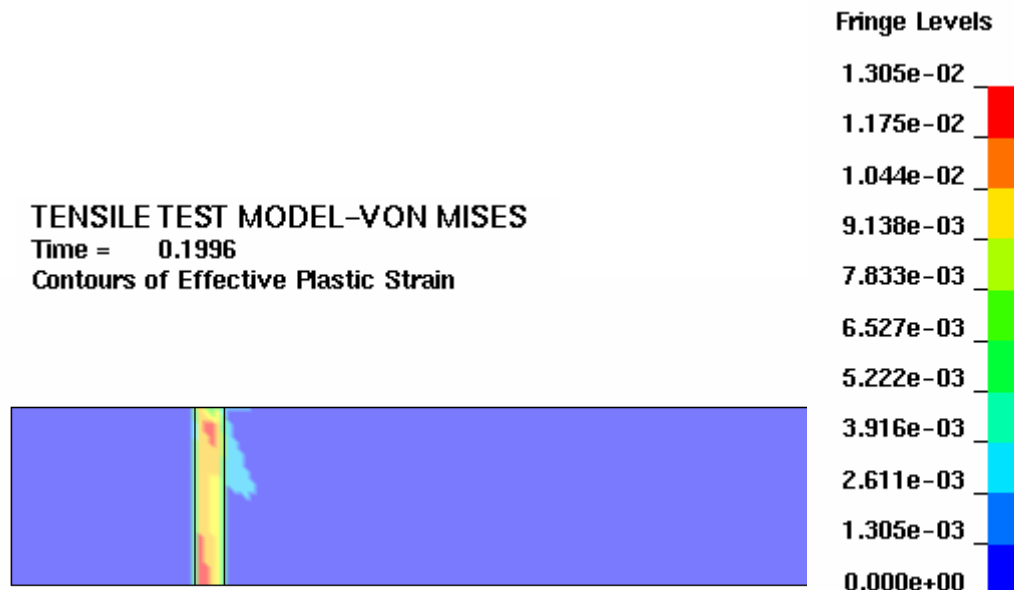
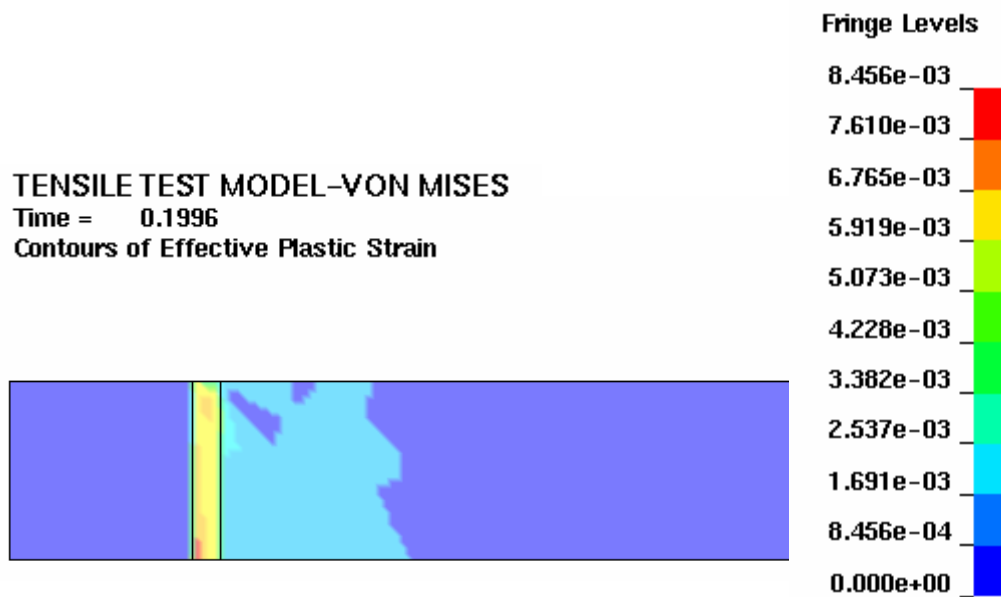


Figure 5-7 Variation of maximum load and displacement with respect to decrease in HAZ strength for welded sample with 0.5 mm HAZ width in the simulation.



(a)



(b)

Figure 5-8 Plastic strain contours in different zones of weldments for HAZ strength of (a) 1300 MPa (b) 1450 MPa during time=0.1996 sec of deformation.

Figure 5.13 and Figure 5.14 show the plastic strain contours for two different HAZ strengths at different time during deformation. It was seen that in the case of lower strength (K=1300), there was not uniform strain distribution and strain localization took place in the softened HAZ. But in the case of higher strength coefficient (K=1450) of HAZ, the strength of the softened zone increased with strain hardening, which in turn arrested strain localization and resulted in a more uniform distribution in the base metal. Thus, premature failure of the specimen in the HAZ was avoided, increasing the overall ductility of the welded tensile specimen.

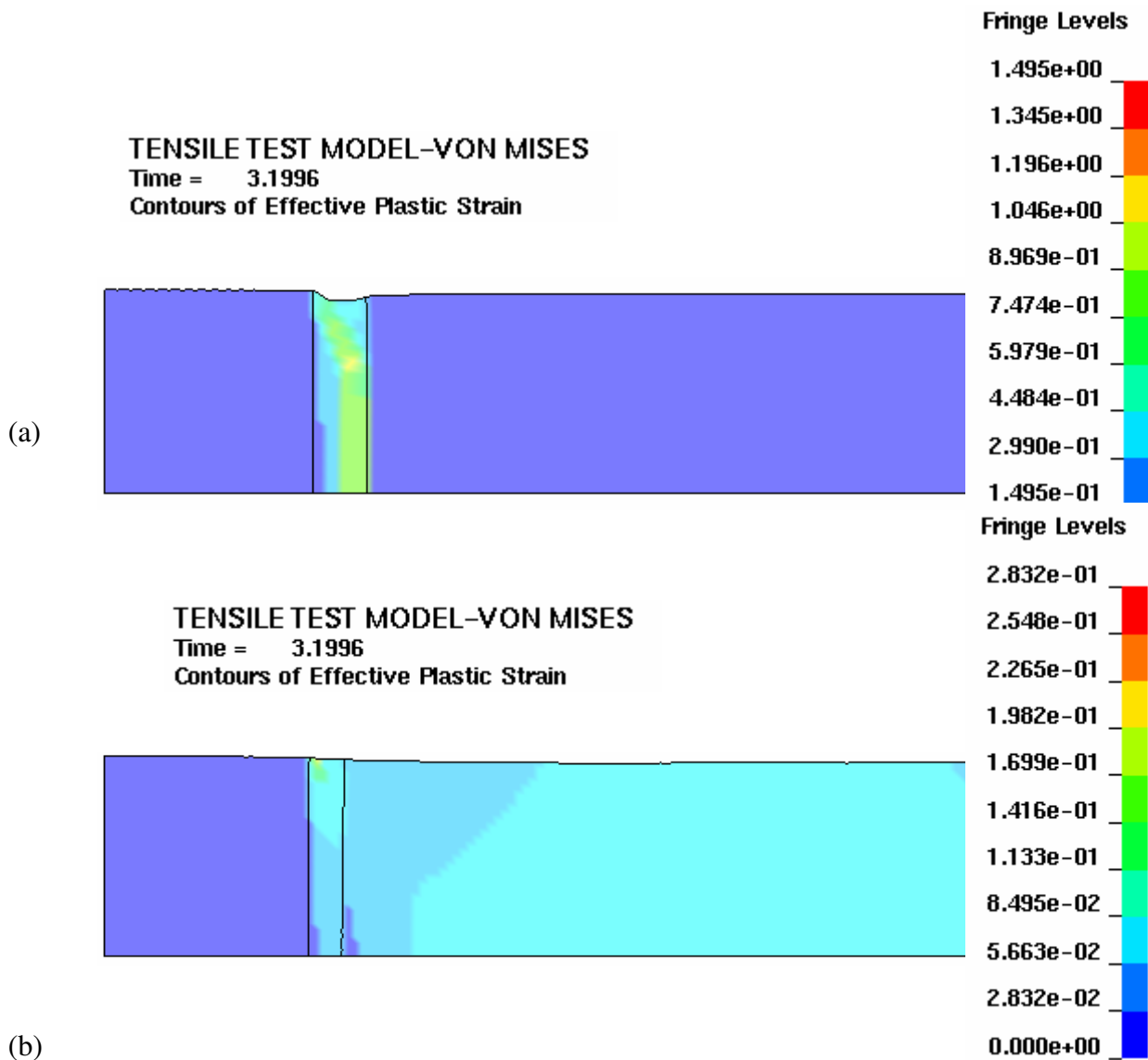


Figure 5-9 Plastic strain contours in different zones of weldments for HAZ strength of (a) 1300 MPa (b) 1450 MPa during time=3.1996 sec of deformation.

### 5.7 Effect of Softened HAZ Width on the Overall Strength and Elongation

The width of the softened HAZ was varied (0, 0.5, 1.5, 2.5 and 4.0 mm) while the strength coefficient was held constant at 1290 MPa. Figure 5.15 shows the effect of HAZ width on the maximum load and ductility of the transverse welded specimen. It was found that the load bearing capacity and ductility decreased sharply as soon as the width

of the softened HAZ increased above zero (i.e. no softening). With further increase in softened HAZ width, the maximum load decreased but the displacement was nearly constant. Figure 5.16 shows contours of stress in Y-direction (Y-stress) developed within the softened HAZ during deformation. In the fusion zone and base metal there was zero Y-stress.

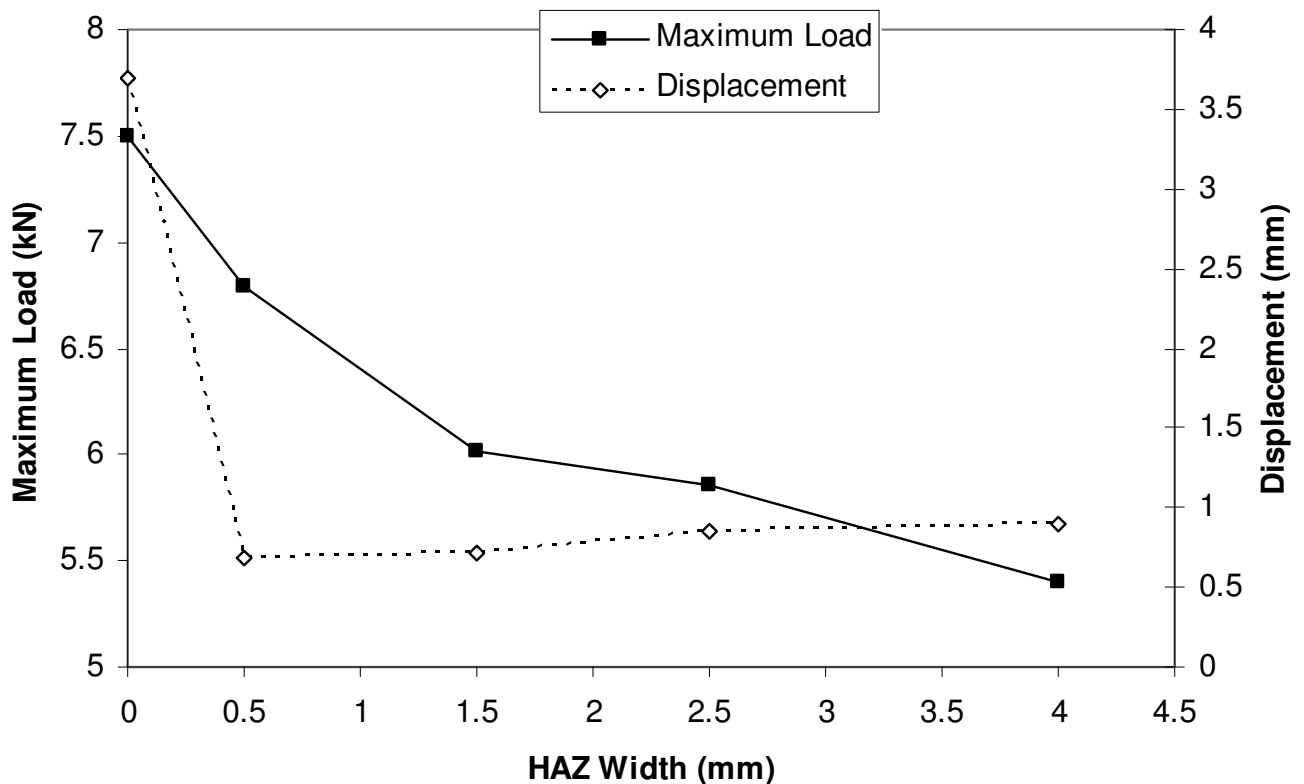


Figure 5-10 Variation of maximum load and displacement with respect to HAZ width (HAZ strength of 1300 MPa) in the simulation.

The stress in the softened HAZ changed from a uni-axial to bi-axial stress state, but the fusion zone and the base metal remained in a uni-axial stress state. During deformation, the strain was localized in the softened HAZ and due to strain in the transverse direction the width of the sample tended to decrease. The adjacent regions (base metal and fusion zone) resisted transverse strain in the softened HAZ, which produced a constraint force and stress in the Y-direction (Figure 5.16).

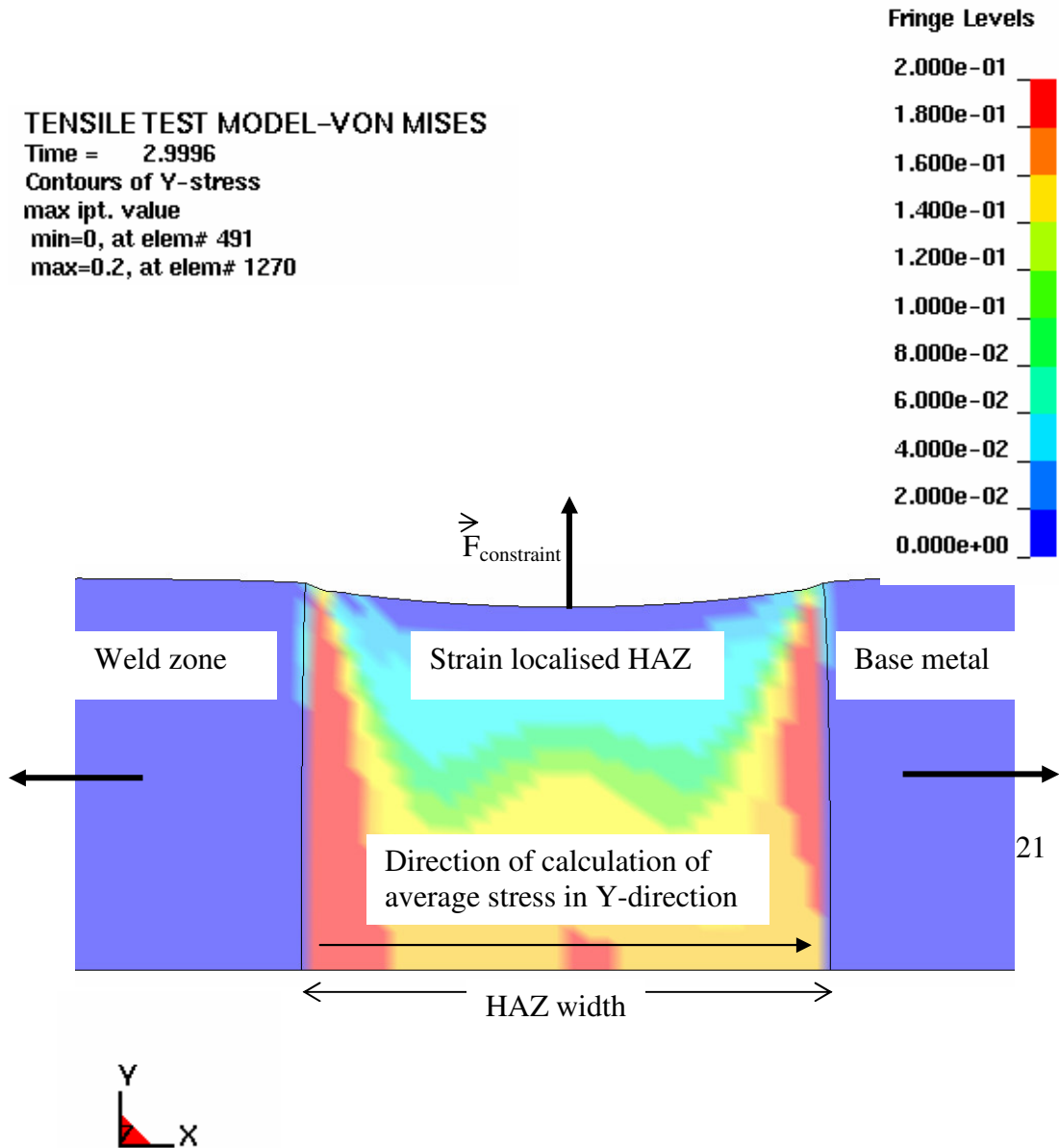


Figure 5-11 Contours of Y-stress during deformation of welded specimen with 4mm HAZ width due to development of constraint force.

The magnitude of the stress component depended on the HAZ width. Figure 5.17 shows that this Y-component decreased as the softened HAZ width increased from 0.5 mm to

4.0 mm. The hydro-static stress (mean stress) component,  $\frac{1}{3}\sigma_{ii}$  within the HAZ increased with increase of stress component in Y-direction. Hence, a relatively larger

tensile force was required to deform the softened HAZ of lower width compared to that of higher width to overcome higher hydrostatic stress component. But hydrostatic stress component does not cause plastic deformation. It was found that the strength of welded specimen with a very narrow HAZ width was close to the base metal.

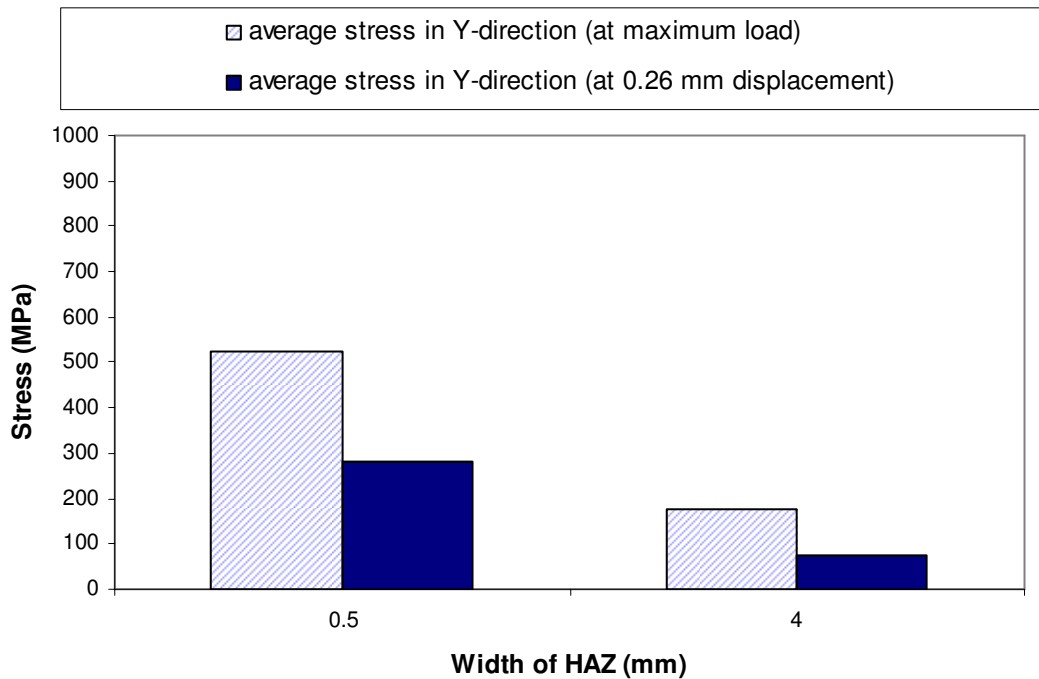


Figure 5-12 Comparison of Y-stress developed in the welded specimen for HAZ width of 0.5 mm and 4mm.

The simulation results show that both the softened HAZ size and hardness (strength) have a significant influence on the load bearing capacity of the welded blank. In terms of ductility, the overall elongation of the sample decreases with decreasing strength in the softened HAZ; however, it is relatively unaffected by increasing HAZ width. In real welds, the severity of softening as well as the softened HAZ width both increase with increasing heat input. As a result, these two factors must be considered simultaneously. Figure 5.9 shows the effects of heat input on the strength and ductility of the transverse weld tensile sample. Both the maximum load and displacement were significantly lower in the high heat input diode welds compared to the low heat input Nd:YAG welds. The diode welds exhibited a wider and softer HAZ than the Nd:YAG welds. When the weld speed was decreased from 1.9 m/min to 0.7 m/min with the diode laser, the width of the

softened HAZ increased; however, the hardness in the softened HAZ was nearly constant. At high heat inputs, the martensite was fully tempered and the hardness does not change with increasing heat input. As a result, the maximum load of the tensile samples decreased with increasing heat input; however, the sample elongation was relatively unaffected.

## **5.8 Summary of the Numerical Results**

This study developed a numerical simulation approach for modeling the tensile test of laser welded DP980 blanks which show significant softening in the HAZ. Material properties for the hardened and softened regions were determined by comparing experimental results with numerical analysis in uniaxial tensile testing. The effects of mechanical properties in the weld region, especially fusion zone hardening and HAZ softening were characterized in terms of formability and strength of the joint. This provided clarification on the significance of the softened region in the HAZ in terms of the effects on the global deformation behaviour of a tailor welded blank.

## **6 Conclusion**

### **6.1 Microstructure**

The microstructure of base metal and laser welded AHSS was characterized.

From this work, the following conclusions were made:

1. With all the diode and Nd:YAG laser weld parameters studied from high to low welding speeds, a combination of severe local hardening and local softening (outer HAZ) happened across welds in DP800 and DP980 steel, as a result of metallurgical change caused by the welding thermal cycle.
2. Dimensions (depth, width) of the softened zone were found to be inversely related to heat input (welding speed and to the irradiance of the laser).

### **6.2 Tensile Testing**

Both longitudinal and transverse tensile testing of base metal and welded AHSS was conducted. Softened HAZ of the welded DP980 steel influenced tensile properties. From this the following conclusions were made:

1. In uniaxial tensile testing, DP980 showed a sharp decrease in strain after laser welding, particularly in the transverse orientation. The fracture site was invariably at the soft zone in DP980 steel welds in transverse orientation. The HSLA weld steel also exhibited lower strain than base metal, but enjoyed a higher strain than DP980 weld under same welding conditions.
2. DP980 steel deformation behaviour can be approximated by Hollomon's power law of hardening equation, without much discrepancy in the plastic region for predicting load bearing capacity and elongation. But the fusion weld zone does not obey power law of hardening during deformation.
3. Strain is localized in the softened HAZ and the remaining region undergoes negligible plastic deformation in uniaxial transverse tensile testing. On further deformation fracture takes place in the HAZ.

### **6.3 Numerical Simulation of Tensile Test**

Numerical simulation of transverse tensile test of base metal and laser welded DP980 steel was developed. Numerical result was validated to the experimental result. From this the following conclusions were made:

1. Experimental results agree with numerical simulations and indicate that strain localization decreases tensile strength and elongation of laser welds in DP980.
2. The strength of HAZ properties can be predicted well by FEM analysis by pragmatic process optimisation technique.
3. The HAZ strength and its width are controlling factors for load bearing capacity and the ductility of the laser welded steel sheets.

### **6.4 Formability Properties**

The limiting dome height test of both the base metal and the welded AHSS was determined. Influence of laser welding on the formability was observed. From this work, the following conclusions were made:

1. Compared to the base metal, sharp decrease of formability was observed for DP980 welded specimens and while HSLA welded specimens possessed the same formability as base metal, regardless of the welding speed. HSLA and DP980 steel show different sensitivities to laser welding in terms of formability.
2. Formability was significantly affected by the presence of the softened zone in the welded DP980 steel, with reduction of formability becoming greater as softened zone size increased. Higher welding speed was achieved as the irradiance of the Nd:YAG laser develop a keyhole mode of welding, which generated a shorter weld thermal cycle and hence a smaller softened zone, yielding a better formability of welded blanks.
3. No significant difference was observed in the formability of the DP980 steel with change in welding orientation relative to the rolling direction or variation of the welded specimen location on the punch (face or root side of the weld), as softened zone dominated the formability behaviour.

4. The hardness distribution across the weld can be a useful indicator for the formability of laser welded sheet metals. Soft zone across the weld is detrimental to the welded specimens' formability.
5. The formability ratio of laser welded DP sheet steels generally decreases with increased base metal strength. Significantly lower LDH strain was observed in higher strength DP steels.
6. Both in uniaxial tensile test and biaxial LDH tests, the fracture occurred in the softened zone of the welded DP980 samples consistently slightly farther out from the weld centerline than the location of the minimum hardness.

## References

1. Auto Steel Partnership ,Advance High Strength Steel Application Guidelines, IISI, March 2005
2. Steen, W.M. Laser Material Processing, 3rd Edition. Springer, London, UK,2003.
3. Duley, W.W. Laser Welding. John Wiley & Sons, Inc., New York, NY, 2000.
4. Bruce, H. Moraki, O. Laser Weldability of Dual Phase Steels in Tailored Blank Applications, SAE Technical Papers Series: 2002-01-0150, 2002.
5. Lawson, S. Li, X. Zhou, Y. Sheet Metal Welding Conference XII, 2006.
6. Mondal, D.K. Dey, R.M. Effect of grain size on the microstructure and mechanical properties of a C-Mn-V dual-phase steel, Materials Science and Engineering, Volume A149, 173-181,1992
7. Huppi, G. S. Matlock, D. K. Krauss, G., An evaluation of the importance of epitaxial ferrite in dual-phase steel microstructures, Scripta Metallurgica, Volume 14, Issue 11, November, 1239-1243,1980
8. Rocha, R.O. Melo, T.M.F. Pereloma E.V. Santos, D.B. Microstructural evolution at the initial stages of continuous annealing of cold rolled dual-phase steel, Materials Science and Engineering, Volume A391, 296-304, 2005
9. Erdogan, M. Priestner, R. Effect of epitaxial ferrite on yielding and plastic flow in dual phase steel in tension and compression, Materials Science and Technology, Volume15, Issue 11, 1273-1284, 1999
10. Xia, M. Sreenivasan, N. Lawson, S. Zhou, Y. J. Eng. Mat. Technol. 129, pp. 446-452 2006.
11. Sarwar, M. Priestner, R. Influence of ferrite-martensite Microstructural morphology on tensile properties of dual-phase steel, Journal of Materials Science,Volume 31, 2091-2095,1996
12. Lawson, R. D. Matlock, D. K. Krauss, G. An etching technique for microalloyed dual-phase steels, Metallography, Volume 13, Issue 1,P 71-87,1980
13. Liedl, U. Traint S. Werner, E.A. An unexpected feature of the stress-strain diagram of dual-phase steel, Computational Materials Science, Volume 25, 122-128, 2002

14. Cribb, W.R. Rigsbee, M. Structure and Properties of Dual-Phase Steels, ed. A.T. Davenport, Warrendale, Pennsylvania, 1979
15. Fischmeister, H. Karlsson, B. Plastizitätseigenschaften grob-zweiphasiger Werkstoffe, Z. Metallkunde, 311-327,1977
16. Yurioka, N. Suzuki, H. Ohshita, S. Saito, S. Welding Journal, 1983 V.62,147s-153s,1980
17. Sakuma, Y. Matlock, D.K. Krauss, G. Intercritically annealed and isothermally transformed 0.15 pct C steels: Part 1. transformation, microstructure, and room temperature mechanical properties, Metallurgical Transactions of the ASME, Volume 23A, 1221-1231,1992
18. Hahn, G.T. Model for yielding with special reference to yield-point phenomena of iron and related BCC metals, Acta Metallurgica, Volume 10, 727-738,1962
19. Gorni, A.A. Mei, P.R. Development of alternative as-rolled alloys to replace quenched and tempered steels with tensile strength in the range of 600-800 MPa, Journal of Materials Processing Technology, Volume 162-163, 298-303, 2005
20. Nemat-Nasser, S. Guo, W.G. Thermomechanical response of HSLA-65 steel plates: experiments and modeling, Mechanics of Materials, Volume 37, 379-405, 2005
21. Kilber, J. Schindler, I. Recrystallization/precipitation behaviour in microalloyed steels, Journal of Materials Processing Technology, Volume 60, 597-602, 1996
22. Kalpakjian, S., and Schmid, S.R., Manufacturing Engineering and Technology, Pearson Education, India.,2003
23. American Iron and Steel Institute, AISI Forms Tailored Steel Product Alliance to Help Facilitate Tailored Steel Market Growth, [http://www.steel.org/news/newsletters/2006\\_02/tspa.htm](http://www.steel.org/news/newsletters/2006_02/tspa.htm),2006
24. Pallett, R.J., and Lark, R.J.,The Use of Tailored Blanks in the Manufacture of Construction Components, **117**, pp. 249-254,2001.
25. Ready, J. F. LIA handbook of laser materials processing, 2001
26. Bleck, W., Cold-Rolled, High-Strength Steels for Auto Applications, J. Metals, 48, pp. 26-30,1996.

27. Heiple, C.R., Burgardt, P. Fluid Flow Phenomena During Welding, ASM Handbook Vol. 6, Welding, Brazing and Soldering. ASM International, Materials Park, OH, pp. 19-24,1993
28. Zhao, H., White, D.R., DebRoy, T. Current issues and problems in laser welding of automotive aluminium alloys, International Materials Reviews, 44 (6), pp. 238-266,1999
29. Swift-Hook, D.T., Gick, A.E.F. Penetration Welding with Lasers, Welding Journal, 52 (11), pp. 492s-499s,1973
30. Automotive Steel Design Manual, Revision 6.1. American Iron and Steel Institute, Southfield, MI, 2002.
31. Schaik,M. Wenk,D. SOUTRAC®: The Future for Welding of AHSS Tailored Blanks: SAE Technical paper series 2003-01-2779
32. Finlay, M.R. Resistance Spot Welding of Metallic Coated Steels and PVD Coated Electrodes, Australian Welding Research CRC No. 18, 1996.
33. Uchihara, M. Fukui, K. Tailored Blanks of High Strength Steels – Comparison of Welding Processes : SAE Technical paper series 2003-01-2829
34. Larsson, J. K.: Supporting Welding Methods for Future Light Weight Steel Car Body Structures: SAE Technical paper series 2002-01-2091
35. Ramasamy, S; Albright, C.E.; CO2 and ND:YAG Laser beam welding of 6111- T4 Aluminum Alloy for Automotive Applications: Journal of laser applications 2000Vol. 12 issue No.3, pg : 101
36. Ghoo, B. Y; Kim, Y. S.: Evaluation of the mechanical properties of welded metal in tailored steel sheet welded by CO2 laser: Journal of materials processing technology 113, pg : 692-698,2001
37. Scriven, P. J.; Brandon, J.A and Williams, N.T.: Influence of weld Orientation on forming limit diagrams of similar/dissimilar thickness laser welded joints: Proceedings of the Institute of material, Ironmaking Steelmaking, 23(2) ,Pg:177-182 ,1996.
38. Howard, K., Lawson, S., Zhou, Y. Diode Laser Welding of Aluminum. Proc. AMT 2004. Government of Canada Catalogue No. NR15-70/2004E-MRC, 2004.

39. Abe N., Tsukamoto M., Morikawa A., Maeda K., Namba K. Welding of Aluminum Alloy with High Power Direct Diode Laser. Trans. JWRI. 31 No.2, 2002.
40. Herfurth, H.J., Ehlers, B. Increased Performance Broadens Processing Capabilities of High Power Diode Lasers. Proc. ICALEO, Laser Applications in the Automotive Industry. Vol. 91 pp. D9-D18,2000.
41. Johnson, W. Mellor, P.B., Engineering Plasticity, Van Nostrand Reinhold Company London,1975.
42. Mellor P.B.,Sheet Metal Forming, Int. Metall. Rev., **1**, pp. 1-20,1981.
43. Lee, Y. Formability of Aluminum alloy Tailor welded blank. Master thesis Department of Mechanical Engineering, University of Waterloo, 2001.
44. Shi, M.F; Thomas, G.H.; Chen, X.M: Formability performance comparison between Dual Phase and HSLA Steels: 43RD MWSP Conference. Proceeding., Vol. XXXIX, pp:165-174,2001.
45. Chen, X.M., Shi, M.F; McKune, P.M; Chen, S.M.: Applications of High Strength Steels in Hydroforming Dual Phase Vs. HSLA
46. Sriram, S., Yan, B., Huang, M.: Characterization of press formability of advanced high strength using laboratory tests; SAE 2004-01-0506
47. Kamura, M., Omiya, Y., Shaw, J., Chen, M., : Formability and Spring Back Characterization of Advanced High Strength Steel SAE 2003-01-0522
48. Irving, B., Blank Welding Forces Automakers to Sit Up and Take Notice, Weld. J., 70 (9), pp. 39-45,1991
49. Azuma, K., Ikemoto, K., Sugiura, H., Press Formability of Laser Welded Blanks, 16th IDDRG, 1990
50. Radlmayr, K.M., Szinyur, J., Laser welded sheet panels for the body in white, IDDRG Working Groups Meeting, PISA, Italy, 1991
51. Saunders, F.I., Wagoner, R.H., Forming of Tailor-Welded Blanks, Metallurgical and Materials Transactions: A, 27A(9) ,2605-2616,1996.
52. Waddell, W, Jackson, S., Wallach, E.R., The Influence of the Weld Structure on the Formability of Laser Welded Tailored Blanks, IBEC1998, SAE Paper 982396, 1998.
53. Chan, L.C. Chan, S.M. Cheng, C.H. Lee, T.C ASME J. Eng. Mat. Technol. V.127 743-751,2005

54. Breakiron, B. Fekete, J. R. SAE Technical paper series: 2005-01-1326, 2005.
55. Lawson, S. Li, X. Zhou, Y. Sheet Metal Welding Conference XII , 2006.
56. Aristotile, R., Fersini, M., Tailored Blanks' for Automotive Components, Welding Research Abroad, 45(1) 16, 1999.
57. Dry, D; Hughes, D; Owen, R: Methods of assessing influence of weld properties on formability of laser welded tailored blanks: Ironmaking & Steelmaking: ISSN: 03019233 Vol.28; part 2 pg 89-95
58. Shi, M., Pickett, K., Bhatt, K. , Formability Issues in the Application of Tailor Welded Blank Sheets, SAE Paper 930278,1993.
59. Baysore, J.K., Laser Beam Welding and Formability of Tailored Blanks, Welding Journal, 74(10) 345s, 1995
60. Chan, S.M., Chan, L.C., Lee, T.C., Deformation Mode Analysis of Forming Limit Diagrams for Tailor-welded Blanks, SAE Paper, 2001.
61. Smerd, R. Winkler, S. Worswick, M.. High rate tensile testing of automotive aluminum alloy sheet International J. of Impact Engineering 32, 541–560, 2005
62. Bailey, S.J. Baldini, N.C. Barkley, E.I. Peters, K.A. Rosiak, J.L. Simms,S.T. Annual book of ASTM standards: metals – mechanical testing; 2003.
63. Biro, E. Lee, A.2004, Welding Properties of Various DP600 Chemistries, Sheet Metal Welding Conference□, Sterling Heights, MI May 11-14,.,pp, 1-11
64. Sreenivasan, N. Xia, M. Lawson, S. Zhou, Y. Effects of Laser welding on formability of DP980 Steel, accepted in , J. Eng. Mat. Technol., 2007.
65. Sreenivasan, N. Kuntz, M. Zhou, Y. Influence of laser welding on the formability of AHSS steels ,accepted in , MST conference by ASM Int. , Detroit ,2007.
66. Ghosh, P.K. Gupta, P.C. Avtar,R. Jha, B.K., Resistance Spot Weldability of Comparatively Thick C-Mn-Cr-Mo Dual Phase Steel Sheet, ISIJ International, 30(3), pp. 233-240, 1990.
67. Hsu, C. Soltis, P. Carroscia, M. Barton, D. Occhialini, C., Weldability of Dual-Phase Steel with Arc Welding Processes, Sheet Metal Welding ConferenceXI, Sterling Heights, MI May 11-14, pp:1-11, 2004.

68. Irving, B., Welding Tailored Blanks is Hot Issue for Automakers, *Weld. J.*, 74 (8), pp. 49-52, 1995.
69. Keeler, S. Brazier, W.G. Microalloying conference, 517-527, 1975.
70. Ovreas L and Thaulow C Mechanical properties of AlMgSi1 weldments and the significance of the softened heat affected zone 3rd Int. Conf. Alumin. Alloys (Trondheim) pp 106–12, 1992.
71. Rodrigues, D. M. Menezes, L. F. Loureiro, A. Fernandes J.V. Numerical study of the plastic behaviour in tension of welds in high strength steels, *Int. J. of Plasticity* 20 1-18 , 2004
72. Martilla, W.A. Forrest, M.G. Inter. Institute of Welding Conference III-1389-06 ,2006.
73. LS-DYNA User's Manual, LSTC, Inc.
74. HyperMesh 7.0 User's Manual, Altair Computing, Inc.
75. Dieter, G.E., Mechanical Metallurgy, McGraw Hill, Singapore, 1988.
76. Castro, V. de Leguey, T. Munoz, A.. Monge, M.A Pareja, R. Mater. Sci. Eng. A, 400-401, 345-348, 2005.
77. Hecker, S.S., A Cup Test for Assessing Stretchability, *Metals Eng. Quart.*, pp. 30-36, 1974.
78. Narasimhan, K. Nadedkar, V.M., Formability Testing of Sheet Metals, *Trans. Indian Inst. of Metal.*, 49, pp. 659-676, 1996.
79. Ghosh, A.K., The Effect of Lateral Drawing-in on Stretch Formability, *Metal. Eng. Quart.*, 15, pp. 53-64, 1975.
80. Miles, M.P., Siles, J.L., Wagoner, R.H., and Narasimhan, K., A Better Sheet Formability Test, *Metall. Trans. A*, 24, pp. 1143-1151, 1993.
81. Nuvonyx ISL-4000L Industrial Laser Owner's Manual. Nuvonyx Inc., Bridgeton, MO, 2001.
82. Nakagawa, N., Ikura, S., Natsumi, F., Iwata, N., Finite Element Simulation of Stamping a Laser-Welded Blank, SAE Technical Paper Series 930522, 1993.
83. Xia, M. Biro, E. Tian, Z. Zhou, Y. Effects of Heat Input and Martensite on HAZ Softening in Laser Welding of Dual Phase Steels, submitted in, Iron and steel institute of Japan, 2007.

84. Panda, S. K., Ravi Kumar, D., Kumar, H., Nath, A. K., Characterization of Tensile Properties of Tailor Welded IF Steel Sheets and Their Formability in Stretch Forming, *J. Mater. Process. Technol.*, 183, pp. 321-332,2007.
85. Abdullah, K., Wild, P. M., Jeswiet, J. J., and Ghasempoor, A.,Tensile Testing of Weld Deformation Properties in Similiar Gage Tailor Welded Blanks Using the Rule of Mixtures, *J. Mater. Process. Technol.*, 112, pp. 91-97,2001
86. Tomokiyo, T., Taniguchi, H., Okamoto, R., Miyagi, T., Furusako, S.,Effect of HAZ Softening on the Erichsen Value of Tailored Blanks”, *SAE Technical Paper Series* 2006-05-0140,2006.